NASA CR-54033

213P

N64-28735
(ACCESSION NUMBER)
213
(PAGES)
CR-54033
(NASA CR OR TMX OR AD NUMBER)
(THRU)
1
(CODE)
27
(CATEGORY)
FACILITY FORM 602

ANALYSIS OF ELECTRON-ION MIXING IN ION ENGINES

FINAL REPORT

by

R. P. Wadhwa and G. Kooyers

prepared for

NATIONAL AERONAUTICS AND SPACE ADMINISTRATION

CONTRACT NAS 3-2503

OTS PRICE

XEROX $ 14.50 ph.
MICROFILM $

RESEARCH
LABORATORY

LITTON
INDUSTRIES

ELECTRON
TUBE
DIVISION

SAN CARLOS
CALIFORNIA

NOTICE

This report was prepared as an account of Government sponsored work. Neither the United States, nor the National Aeronautics and Space Administration (NASA), nor any person acting on behalf of NASA:

A.) Makes any warranty or representation, expressed or implied, with respect to the accuracy, completeness, or usefulness of the information contained in this report, or that the use of any information, apparatus, method, or process disclosed in this report may not infringe privately owned rights; or

B.) Assumes any liabilities with respect to the use of, or for damages resulting from the use of any information, apparatus, method or process disclosed in this report.

As used above, "person acting on behalf of NASA" includes any employee or contractor of NASA, or employee of such contractor, to the extent that such employee or contractor of NASA, or employee of such contractor prepares, disseminates, or provides access to, any information pursuant to his employment or contract with NASA, or his employment with such contractor.

Requests for copies of this report should be referred to

National Aeronautics and Space Administration
Office of Scientific and Technical Information
Attention: AFSS-A
Washington, D. C. 20546

9750 CASE FILE COPY

NASA CR-54033

FINAL REPORT

ANALYSIS OF ELECTRON-ION MIXING IN ION ENGINES

by

R. P. Wadhwa and G. Kooyers

prepared for

NATIONAL AERONAUTICS AND SPACE ADMINISTRATION

March 31, 1964

CONTRACT NAS 3-2503

Technical Management
NASA Lewis Research Center
Cleveland, Ohio
Space Craft Technology Division
S. Jones and W. Rayle

RESEARCH LABORATORY
LITTON INDUSTRIES
ELECTRON TUBE DIVISION
960 INDUSTRIAL ROAD
SAN CARLOS, CALIFORNIA

FOREWORD

This is a summary report on the work performed under the subject study program from June 1962 to February 1964. The one-dimensional analysis was performed by G. P. Kooyers, while the two-dimensional analysis was performed by R. P. Wadhwa. Professor O. Buneman acted as a consultant throughout the program and made several significant contributions. Mr. R. Hockney also acted as a consultant and made significant contributions towards the solution of Poisson's equation in the two-dimensional analysis. Mr. D. F. Brauch and Miss P. A. Vartanian contributed towards programming on the high speed digital computer. This work was completed under the supervision of Dr. S. P. Yu, who also made several helpful suggestions.

OBJECTIVE

The objective of the work to be performed under this contract is the study of the transient and oscillatory phenomena in an ion beam into which electrons are injected for the purpose of neutralization. The studies are aimed at obtaining a more complete understanding of the ion-electron mixing process as it applies to ion-beam engines, with specific attention being given to factors which might affect the performance of such an ion engine.

ABSTRACT

28736

Electron-ion mixing is studied in one- and two-dimensional configurations with the use of a high speed digital computer. These studies are important for optimizing the electron emission required for adequate space-charge neutralization of ion beams for ion-engine applications. Ions are injected across the accel grid at constant velocity while electrons are emitted at the decel plane with Maxwellian velocity distribution. Finite dimensions for the ion beam and electron emitter are considered for the two-dimensional configuration. The mathematical formulations in both the cases are normalized in a convenient manner, and the charged particles are updated at every unit-time interval according to self-consistent space-charge and dc fields evaluated by superfast methods. Poisson's equation is solved by using Green's method in the one-dimensional configuration and by using the Fourier analysis and "marching method" in the two-dimensional configuration. For the two-dimensional case, both the ideal (transparent) and actual cases of decel grid are investigated. Several values of ion-electron mass ratio, emission, velocity, and electron emitter temperature are studied. The ship potential and thrust are calculated in each case.

Author

The results of the two formulations indicate that an ion instability may be caused when the number of electrons is insufficient, although the results of the two-dimensional formulation seem to indicate that a smaller number of electrons is needed for space-charge neutralization. Such an instability causes deterioration in both thrust and ship potential. For the two-dimensional configuration, the transverse ion-beam spread is found to be inversely proportioned to ion mass. There is an adequate space-charge neutralization in the vicinity of the decel grid; the ion-beam seems to be well compressed, except for some residual space-charge. The fluctuations in thrust and ship potential seem to be decreased as the ion mass is increased. The electrons seem to follow the ions very closely, and the average exit velocity of electrons is almost equal to that of the ions.

For the case of an aperture in the two-dimensional configuration, the equipotentials are significantly changed, and almost all the electrons are directed towards the ion beam, resulting in higher space-charge neutralization of the ion beam. Poisson's equation, in this case, is solved by modifying the marching method and using capacitance matrix.

TABLE OF CONTENTS

Section	Title	Page
	Foreword	ii
	Objective	iii
	Abstract	iv
	List of Figures	ix
I.	HISTORICAL SUMMARY OF THE ELECTRON-ION MIXING PROBLEMS	1
II.	ONE-DIMENSIONAL ANALYSIS	7
	A. General	7
	B. Formulation of the One-Dimensional Analysis	12
	C. Calculation of Actual Thrust Per Unit Area	21
	D. Calculation of Ideal Thrust Per Unit Area	25
	E. Comparison Between Ideal and Actual Thrust	27
	F. Random Electron Emission Velocity	28
	G. Integrated Plasma Potentials	30
	H. Definitions of Symbols used in One-Dimensional Configuration	32
III.	ONE-DIMENSIONAL RESULTS	34
	A. Review of the Computer Model	34
	B. Plots Made from the Calculations	37
	C. General Results	37
	D. Detailed Results and Discussion	40
	E. Shelf Development Condition	71
IV.	TWO-DIMENSIONAL ANALYSIS	79
	A. Introduction	79
	B. Assumptions Made in This Analysis	81
	C. Description of the Physical Model	81
	D. Development of Normalized Poisson's Difference Equation	87

TABLE OF CONTENTS (Cont.)

Section	Title	Page
	E. Evaluation of Space-Charge Voltage	94
	1. Region I	96
	2. Region II	99
	3. Inclusion of the DC Terms in Field Computations	102
	4. Evaluation of Ship Potential	104
	F. Interpolation of Fields Near the Grids . .	104
	G. Trajectory Equations	106
	H. Normalization of the Various Parameters and Injection Conditions	110
	I. Injection Conditions	113
	J. Evaluation of Thrust	116
	K. Definition of Symbols used in Two-Dimensional Configuration	121
V.	RESULTS OF TWO-DIMENSIONAL ELECTRON-ION MIXING	123
	A. Considerations in Computer Simulation . .	123
	B. Choice of Parameters	124
	C. Variation with Ion Mass Ratio	126
	D. Variation with Electron Emission	146
	E. Variation with Electron Temperature . . .	153
	F. Variation with Normalized Charge	159
	G. Extrapolation of Results to Practical Cases	162
	H. Correlation Between One-Dimensional and Two-Dimensional Results	165
VI.	TWO-DIMENSIONAL ELECTRON-ION MIXING WITH AN APERTURE AT THE DECEL GRID PLANE	169
	A. Introduction	169
	B. Evaluation of Capacitance Matrix	170
	C. Solution of Poisson's Difference Equation with Boundary Constraints	174
	D. Thrust Evaluation	177
	E. Results	178

TABLE OF CONTENTS (Cont.)

Section	Title	Page
VII.	CONCLUSIONS AND SUGGESTIONS FOR FURTHER WORK	191
	A. Conclusions	191
	B. Suggestions for Future Work	196

LIST OF FIGURES

Figure No.	Title	Page
2-1	Electrode Schematic of an Ion Engine	8
2-2	Electrode Schematic of the Simulated Ion Engine	10
2-3	Variation of Electric Field	11
3-1	One Dimensional Model	35
3-2	Ion Trajectory Plot	41
3-3	Electron Trajectory Plot	42
3-4	Ship Potential vs. Time	43
3-5	Integrated Potentials, Time-Distance Plots . .	44
3-6	Ion Trajectory Plot (Run 12B)	45
3-7	Ship Potential Versus Time (Run 12B)	46
3-8	Integrated Potential vs. Distance (Run 12B) .	47
3-9	Thrust vs. Time (Run 12B)	48
3-10	Ship Potential vs. Time (Run 12BP)	50
3-11	Thrust vs. Time (Run 12BP)	51
3-12	Ion Trajectory Plot (Run 12B, N = 60)	52
3-13	Ship Potential vs. Time (Run 12B, N = 60) . .	53
3-14	Thrust vs. Time (Run 12B, N = 60)	54
3-15	Ship Potential vs. Time (Run 14D2)	57
3-16	Thrust vs. Time (Run 14D2)	58
3-17	Ship Potential vs. Time (Run 14F2)	59
3-18	Thrust vs. Time (Run 14F2)	60
3-19	Ship Potential vs. Time (Run 15F2)	61

LIST OF FIGURES (Cont.)

Figure No.	Title	Page
3-20	Thrust vs. Time (Run 15F2)	62
3-21	Electron Trajectory Plots (Run 15F2), Ion Trajectory Plots (Run 15F2)	63
3-22	Thrust vs. Time (Run 15H)	64
3-23	Ship Potential vs. Time (Run 15HR)	68
3-24	Thrust vs. Time (Run 15HR)	69
3-25	Integrated Potential vs. Distance (Run 15HR) .	70
3-26	Shelf Formation	72
4-1	A Schematic for a Periodic Idealized Ion-Beam Flow	82
4-2	A Schematic of an Idealized Ion-Beam Flow in One Period	83
4-3	Division of the Half Period in the X-Y Plane .	85
4-4	Schematic of Division of the Half Period for Thrust Evaluation	117
5-1	Y Versus X, Ions, (Run 3B)	130
5-2	Y Versus X, Ions, (Run 2E)	131
5-3	Y Versus X, Ions, (Run 4A)	132
5-4	Variation of Ion-Beam Spreading with Ion Mass	134
5-5	X Versus Time, Ions, (Run 2E)	135
5-6	Y Versus X, Electrons, Run 4A)	137
5-7	Electron Cloud Envelope in Normalized Space (For Different Ion Mass Ratios)	139
5-8	X Versus Time, Electrons, (Run 4A)	140
5-9	X Versus Time, Electrons, (Run 3B)	141
5-10	Thrust Versus Time; Variation with Ion Mass .	143

LIST OF FIGURES (Cont.)

Figure No.	Title	Page
5-11	Ship Potential Versus Time; Variation with Ion Mass	145
5-12	Electron Cloud Envelope in Normalized Space for Different Electron Emissions	148
5-13	Y Versus X, Ions, (Run 2G)	149
5-14	X Versus Time, Ions, (Run 2G)	150
5-15	Thrust Versus Time; Variation with Electron Emission	152
5-16	Ship Potential Versus Time; Variation with Electron Emission	154
5-17	Y Versus X, Electrons, (Run 1D)	156
5-18	Y Versus X, Electrons, (Run 1E)	157
5-19	X Versus Time, Electrons, (Run 1D)	158
5-20	Y Versus X, Ions, (Run 3A)	161
5-21	X Versus Time, Electrons, (Run 3A)	163
6-1	A Schematic of Accel-Decel System	172
6-2	An Algorithm for Obtaining Potential Distribution from the Charge Distribution	175
6-3	A Schematic of Marching Process	176
6-4	Thrust Versus Time, (Runs 2E and 5A)	179
6-5	Ship Potential Versus Time, (Run 5A)	180
6-6	Normalized Equipotentials in Normalized Space; (Run 5A), Time Step: 200	182
6-7	Normalized Equipotentials in Normalized Space; (Run 5A), Time Step: 600	183
6-8	Normalized Equipotentials in Normalized Space; (Run 2E), Time Step: 200	184

LIST OF FIGURES (Cont.)

Figure No.	Title	Page
6-9	Normalized Equipotentials in Normalized Space; (Run 2E), Time Step: 600	185
6-10	Normalized Equipotentials in Normalized Space; (Run 5A), Time Step: 10	187
6-11	Y Versus X, Electrons, (Run 5A)	188
6-12	Y Versus X, Ions (Run 5A)	189

ANALYSIS OF ELECTRON-ION MIXING IN ION ENGINES

by R. P. Wadhwa and G. Kooyers

Litton Industries

I. HISTORICAL SUMMARY OF THE ELECTRON-ION MIXING PROBLEMS

The subject of neutralization has been approached with a wide range of attitudes, resulting in varying degrees of optimism and pessimism.

Instinctively, one feels that the heavy ions will always pull along the requisite number of electrons, provided they are made available from some source placed in or near the beam. Any charge imbalance will result in electrostatic fields which redistribute electrons in such a way as to restore neutrality. Indeed, it would appear that this mechanism is not dependent on collisions for its operation, and the scarcity of collisions cannot be invoked against our "instinctive" confidence in successful neutralization.

However, several analytical studies have been made of the problem of collision-free electron-ion mixing. They have, on the whole, yielded negative results[1].

---

1. Seitz, R. N., Shelton, R. D. Stuhlinger, E.; "Status Report on Neutralization," Proceedings of the Monterey Conference, 1961.

Broadly speaking, it is found that the electrostatic field mechanism for the adjustment of electron densities results in "overshooting" by the electrons. At best only neutrality in-the-mean has been achieved in these theoretical models of the mixing problem[2]. Whenever the electrons are released with velocities greater than twice the ion velocities (and in ion engines one would want to release them with possibly three times the ion velocity), theory has failed altogether to provide a rigorous solution: i.e., a self-consistent field distribution in the beam.

This is one cause of possible pessimism regarding efficient mixing, and extensive experimental research was devoted to checking the theoretical predictions. On the whole, these experiments have resulted in reversion to optimism and even complete disregard of the problem. On the other hand, the experiments encountered the criticism that space conditions cannot be simulated properly in the laboratory, and distant boundaries seemed to play a major role in the theories.

In the meantime, further theoretical developments have not been able to settle with certainty the questions

---

2. Staff of Ramo-Wooldridge Research Laboratory, "Electrostatic Propulsion", Proc. of IRE, April 1960, Vol. 48, p 477.

of whether and how neutralization may occur. The search has continued for a static potential distribution in the neutralizer region, taking into account more complicated effects. The original calculations had been concerned with monoenergetic electrons and ions, and had at best resulted in spatially varying potentials, i.e., permanently unneutralized positive and negative regions in a one-dimensional model under the restricted velocity conditions mentioned.

The injection of Maxwellian velocity distributions of electrons into an ion stream which itself is not completely monoenergetic was therefore studied. The following characteristics of such a system may be anticipated:

(1) The temperature is that of the emitter, say 2300°, equivalent to $kT = 0.2$ electron volt, corresponding to a mean one-way electron velocity of 150 km/sec.

(2) The potential is very close (within 0.2 volts) to that of the electron emitter.

(3) The ions, and the whole plasma, drift with a velocity corresponding to the potential difference between ion emitter and plasma. Assuming 3000 volts Cs ions, this is 65 km/sec.

(4) The density is that of the ion beam at this velocity; assuming 15 ma/cm^2 ion current, this means 1.4×10^{10} ions, and the same number of electrons per cm^3.

(5) The electron plasma frequency corresponding to this density is 1000 megacycles/sec.

(6) To produce the assumed Cs ion beam one would use an accelerator grid at -5000 volts, one-third of a cm from the ion emitter.

H. Derfler[3] some time ago developed a complete Boltzmann analysis of the problem stated. As in the case of mono-energetic particles, it was possible at best to obtain spatially periodic potentials with neutrality in-the-mean, provided the mean one-way thermal electron velocity did not exceed that of the ions. Derfler suggested, and this has been the view of many other theoreticians[4], that neutralization, if it occurs in space, cannot be a strictly static process. Somewhere there must be a source of entropy, i.e., a mechanism which causes ergodic behavior and increases disorder.

A considerable effort is being devoted to investigate the optimum conditions for space-charge neutralization in ion rocket beams. It is expected that the simulation of the electron-ion mixing mechanism in an ion engine on a high speed digital computer (discussed in this report) will add considerably in achieving optimum conditions for space-charge neutralization purposes. Correlation between theoretical and experimental

---

3. Derfler, H., Private communication.

4. Kaufman, H.R., "Electron Diffusion in a Turbulent Plasma", NASA Technical Note D-134, Lewis Research Center.

results[5,6,7,8,9] will be of great help in optimizing the design and further improving the performance of an ion engine.

The simulation of an ion engine described in this report covers three phases. The first two phases describe the formulation and results for the idealized one- and two-dimensional configurations, and the third phase includes the effects of an aperture at the decel grid plane. The formulation and results of the one-dimensional configuration are described in Sections II and III, respectively, while the formulation and results of the two-dimensional configuration (idealized) are discussed in Sections IV and

---

5. Design, Fabrication, and Testing of a Cesium Ion Rocket Engine, Summary Rpt. Phase III, Contract No. NAS 5-517, Hughes Aircraft Company Research Laboratories, Malibu; March 1964.

6. Kaufman, H.R., "The Neutralization of Ion Rocket Beams"; Technical Note D-1055, NASA Lewis Research Center; August 1961.

7. Kemp, R.F., Sellen, J.M., Jr., and Pawlik, E.V., "Neutralization Tests on a Flight-Model Electron Bombardment Ion Thrustor", Technical Note D-1733, NASA Washington; July 1963.

8. Sellen, J.M. and Shelton, H. "Transient and Steady State Behavior in Cesium Ion Beams", presented at the American Rocket Society Electrostatic Propulsion Conference, Monterey, Calif., November 3-4, 1960.

9. Sellen, J.M. and Kemp, R.F., "Cesium Ion Neutralization in Vehicular Simulation", presented at the joint meeting of the National IAS-ARS, Los Angeles, Calif., June 13-16, 1961.

V. The effects of an aperture at the decel grid plane are described in Section VI, and Section VIII describes the conclusions and suggestions for future work.

II. ONE-DIMENSIONAL ANALYSIS

A. General

The ion-engine configuration simulated on the high speed digital computer is shown in Fig. 2-1. The model of the emitter neutralizer system was reduced to less and less complicated forms for the purpose of maximum economy in the numerical procedure. Starting from the configuration shown in Fig. 2-1, we eliminated Region A and forced ions through the "accel grid" with a given unalterable velocity and intensity. We also eliminated Region C for a first calculation, letting the electrons emerge from a hot ideal grid at spaceship potential.

The omission of A is in error only to the extent that either an unusually energetic electron, or a rejected ion, might penetrate into it; thereby upsetting the normal diode potential distribution in this space which, in accordance with Child's law, determines the ion current forced into Region B. In the computer program particles which pass through the accel grid in the wrong direction are written off.

We assume zero thermal spread of the incoming ion velocities, since there are several thousand volts across Region A, compared with 1/10 volt thermal energy at emission, and since acceleration has, by itself, a "cooling" effect.

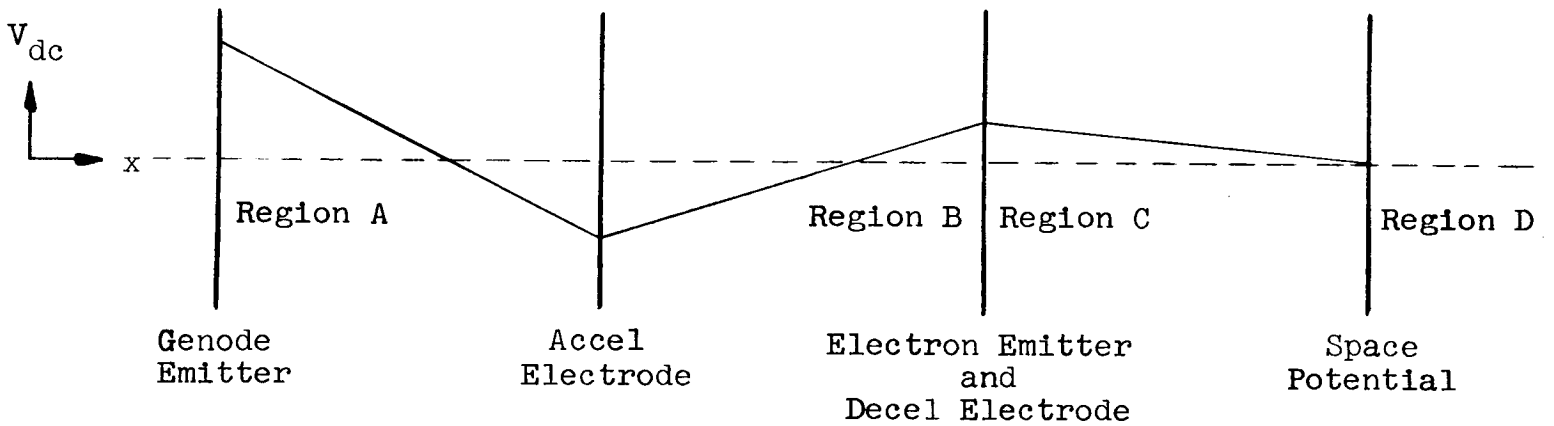

ELECTRODE SCHEMATIC
OF AN ION ENGINE

Fig. 2-1

The spaceship will charge up; i.e., the potential of the electron emitter will rise and fall with respect to that at infinity in accordance with the amount of charge ejected. In the calculations, the potential of the spaceship will be evaluated. One needs to know the value of the field, and this is, at each location in Region C (see Fig. 2-2), determined by the number of electron sheets minus the number of ion sheets which lie to the right of that location. (In space, beyond the farthest charge sheet, the field is zero.)

In Region B, one determines the field at each location by counting the excess number of electron sheets over the ion sheets between that location and the electron emitting grid, and adding the appropriate multiple to the value of the field immediately to the left of that emitter. The latter field has then to be determined such that the potential drop between accel grid and electron emitting grid has the required value.

A typical field distribution in Regions B and C is illustrated in Fig. 2-3. The determination of the field is accomplished in practice by a count of the number of particles of each (ions or electrons) which lie to the right of any location.

This count requires ordering the particles at each step in time according to their newly acquired positions. A new sorting procedure (appropriate tag numbers are associated with the particles according to their space distribution) was used for this purpose, and

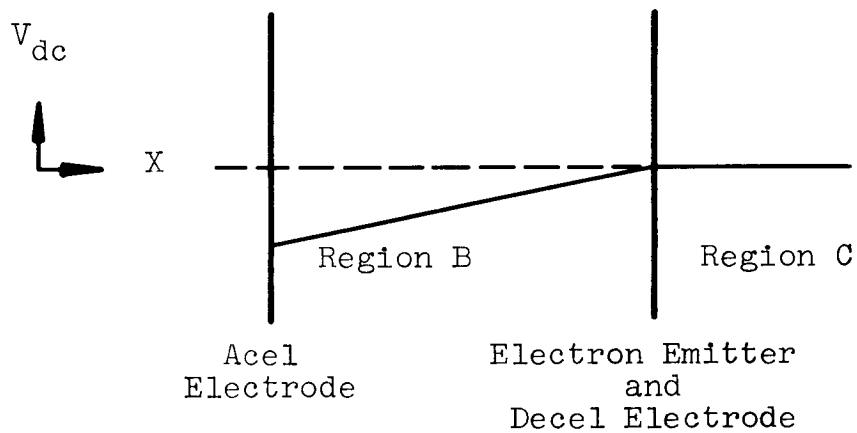

ELECTRODE SCHEMATIC
OF THE SIMULATED ION ENGINE

Fig. 2-2

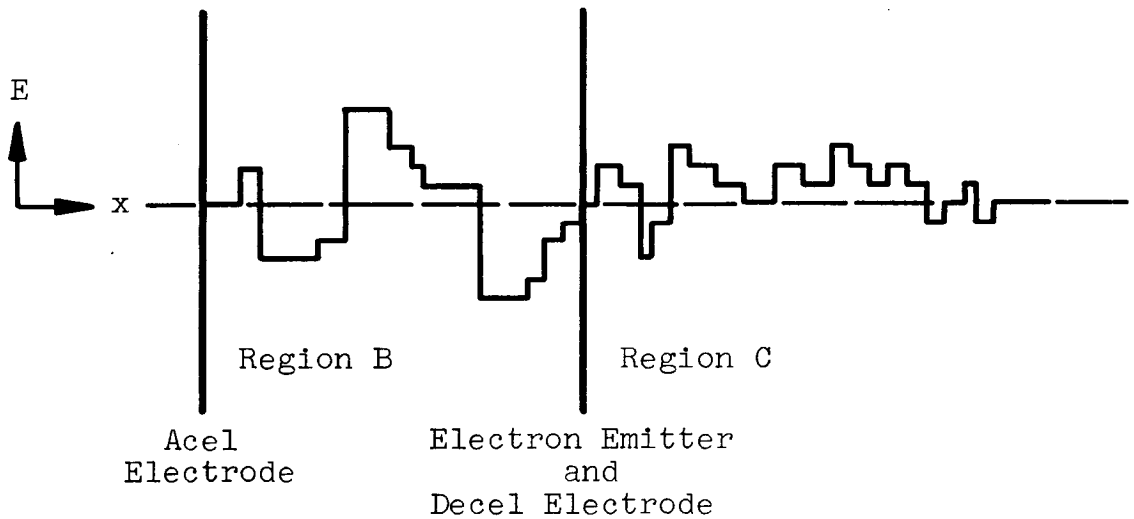

VARIATION OF ELECTRIC FIELD

Fig. 2-3

experience with similar programs was employed. Actually, the sorting was most time consuming and, for 5,000 particles of each kind, took approximately 2 seconds on an IBM 7090 Computer for each time step. The advancing time of each particle through one time step (finite difference formula was used for the acceleration process) was quite short on the computer.

B. Formulation of the One-Dimensional Analysis

Figure 2-2 shows a schematic of the geometry to be used for the analysis. Ions are injected into Region B from the left at a specified rate. The accel electrode is located at $x/\ell = 0$, and the electron emitter at $x/\ell = 1$. Thus, we use the normalized position variable x/ℓ. (See list for definition of symbols in Section II. H.)

The problem is divided into two independent regions (B and C) as shown in Fig. 2-2. Treating the boundary between Regions B and C as a conducting plane allows this division of the problem into two regions. Region B has an ion flux incoming from the left and an ion flux leaving to the right. Electrons are emitted into Region B from the right and should not reach the left boundary. When sufficient electrons are emitted into Region B to form a negative space charge distribution, additional electrons are rejected near the boundary $x/\ell = 1$. Region C starts at $x/\ell = 1$ and goes to $x/\ell =$ infinity. Ions and electrons are injected at the left boundary of Region C at the same rate as they left Region B. Additional electrons are also "boiled" into Region C from the left boundary.

The electron emitter is assumed to be held at a fixed potential relative to the accel grid. The ship is allowed to float in potential. This potential depends on the amount of total charge which has left the ship.

The equations of motion for a one-dimensional charged sheet are:

$$\frac{d^2x_e}{dt^2} = -\frac{e}{m}E \tag{2-1}$$

and

$$\frac{d^2x_i}{dt^2} = +\frac{e}{M}E. \tag{2-2}$$

The procedure for calculation of trajectories begins with the sheet farthest to the right (largest x value). Here the electric field is 0. Whenever a sheet is passed, the electric field jumps by a factor q_s/ϵ_o. The electric field E acting on a sheet is the mean between those prevailing on the right and the left and equals $\left(\frac{\gamma q_s}{2\epsilon_o}\right)$, where γ is a odd integer obtained by counting sheets (see symbol list for definition of γ).

Putting the equations in finite difference form and dividing both sides by the square of a plasma

frequency, we have

$$\frac{\Delta^2 \left(\frac{x_e}{\ell}\right)}{\omega_p^{\ 2}\ \Delta t^2} = \frac{-eE/m}{\left(\frac{\rho}{m}\frac{e}{\epsilon_o}\right)\ell} = -\frac{\epsilon_o}{\ell\rho} E \ . \qquad (2\text{-}3)$$

Now we define $\rho = \frac{Nq_s}{\ell}$ as the standard of charge density with N a pure number yet to be specified; also, $E = \frac{\gamma q_s}{2\epsilon_o}$.

Thus for electrons:

$$\Delta^2 \left(\frac{x_e}{\ell}\right) = -\left[\omega_p^{\ 2}\ \Delta t^2\right]\left[+\frac{\gamma}{2N}\right] , \qquad (2\text{-}4)$$

and for the ions

$$\Delta^2 \left(\frac{x_i}{\ell}\right) = \left(\frac{m}{M}\right)\left[\omega_p^{\ 2}\ \Delta t^2\right]\left[+\frac{\gamma}{2N}\right] \ . \qquad (2\text{-}5)$$

The choice of N for the purpose of defining a conventional standard of charge density (and hence electron plasma frequency) is somewhat arbitrary. We expect to use time steps of the order of one-tenth the electron plasma frequency in the mixing region. Assuming that in this region electrons and ions have comparable densities, and that the ions maintain more or less the density at which they are injected, we

choose the ion charge density at injection as our standard density, but use the electron mass in the calculation of a standard plasma frequency:

$$\omega_p^2 = \frac{e\ \rho}{m\ \epsilon_o} . \tag{2-6a}$$

If now the ions continued to travel at injection velocity in Region B, the number of ion sheets present in that region at any time would just be N, representing an average uniform charge density of amount

$$\rho = \frac{Nq_s}{\ell} . \tag{2-6b}$$

Thus, we have identified the number N.

The ion injection velocity into Region B is determined by the potential between the ion emitter and the accel grid. Thus,

$$u_o = \left(\frac{2e\varphi_o}{M}\right)^{1/2} . \tag{2-6c}$$

Putting in finite difference form and dividing by ω_p, we obtain

$$\frac{\Delta\left(\frac{x_i}{\ell}\right)}{\omega_p\ \Delta t} = \left[\left(\frac{2m}{M}\right) \frac{\varphi_o}{\frac{Nq_s\ell}{\epsilon_o}}\right]^{1/2} . \tag{2-7}$$

Region A (see Fig. 2-1) between the ion emitter and the accel electrode is assumed to have a potential distribution in accordance with Child's law. Thus, the potential is:

$$\varphi_o^{3/4} = \left(\frac{3}{2}\right)\left(\frac{J}{\epsilon_o}\right)^{1/2}\left(\frac{M}{2e}\right)^{1/4} L \quad , \tag{2-8}$$

where L is the distance between ion emitter and accel grid. The ion charge density ρ at injection is related to J by $J = \rho u_o$, where u_o is the ion velocity. Thus,

$$\rho = \frac{J}{u_o} = \frac{J}{\left(\frac{2e\varphi_o}{M}\right)^{1/2}} \quad . \tag{2-9}$$

Then we can form the quantity

$$\frac{\varphi_o}{\rho\ L^2/\epsilon_o} = \frac{\varphi_o}{\frac{J}{\left[2(e/M)\varphi_o\right]^{1/2}}\frac{L^2}{\epsilon_o}} = \left(\frac{3}{2}\right)^2 \quad . \tag{2-10}$$

Thus, from the definition of N,

$$\frac{\varphi_o}{\frac{Nq_s\ L^2}{\epsilon_o \ell}} = \frac{9}{4} \quad . \tag{2-11}$$

Substituting Eq. 2-7 into Eq. 2-11 we get

$$\Delta\left(\frac{x_i}{\ell}\right)_{\text{injection}} = (\omega_p \Delta t)\ \frac{3L}{2\ell}\left(\frac{2m}{M}\right)^{1/2} \qquad (2\text{-}12)$$

In Region B the plasma is bounded by two conducting plates; thus, the formulation of the electric field is slightly different than in Region C. First, the field next to the electron emitter has to be determined. Thereafter, a procedure similar to that used in Region C with an equivalent γ can be used.

To evaluate the field immediately to the left of $x/\ell = 1$ we have

$$E_1 = E_{dc} + \frac{q_s}{\epsilon_o}\left[\sum \frac{x_i}{\ell} - \sum \frac{x_e}{\ell}\right] \quad , \qquad (2\text{-}13)$$

where $\sum$ refers to summation over all ions and electrons in Region B, and $E_{dc} = \varphi_1/\ell$. Rewriting Eq. 2-13 in normalized form by multiplying by $\epsilon_o/q_s N$, we obtain

$$\frac{\epsilon_o\ E_1}{q_s N} = \left(\frac{\varphi_1}{\varphi_o}\right)\left(\frac{L}{\ell}\right)^2\left(\frac{9}{4}\right) + \frac{1}{N}\sum\left[\frac{x_i}{\ell} - \frac{x_e}{\ell}\right] \quad . \qquad (2\text{-}14)$$

Then, using the odd integer γ as defined before but bounding the counting region by $x/\ell = 0$ and $x/\ell = 1$ the equations of motion in finite difference form are

$$\Delta^2 \left(\frac{x_e}{\ell}\right) = - \left[\omega_p{}^2 \ \Delta t^2\right]\left[\frac{\epsilon_o \ E_1}{q_s \ N} + \frac{\gamma}{2N}\right] \qquad (2\text{-}15)$$

and

$$\Delta^2 \left(\frac{x_i}{\ell}\right) = \left[\omega_p{}^2 \ \Delta t^2\right]\left[\frac{m}{M}\right]\left[\frac{\epsilon_o \ E_1}{q_s \ N} + \frac{\gamma}{2N}\right] , \qquad (2\text{-}16)$$

where Eq. 2-14 can be substituted for $\epsilon_o \ E_1/q_s \ N$.

The ion sheets are assumed to be injected into Region B from the left with a uniform velocity distribution. The number that is to be injected in each time step is calculated from the parameters which are initially fed into the program. If we let η_k be the number of ion sheets emitted per time step, then

$$\eta_k = \frac{J \ \Delta t}{q_s} \quad . \qquad (2\text{-}17)$$

Multiplying both numerator and denominator by ω_p, we have

$$\eta_k = \frac{J(\omega_p \Delta t)}{q_s \omega_p} \quad . \qquad (2\text{-}18)$$

Substituting for $J = \rho u_o$ and ω_p as defined above,

$$\eta_k = \frac{\rho u_o \ (\Delta t \ \omega_p)}{q_s \left(\frac{\rho \ e/m}{\epsilon_o}\right)^{1/2}} = \frac{3}{2} N \left(\frac{L}{\ell}\right) \left(\frac{2m}{M}\right)^{1/2} (\omega_p \ \Delta t) \quad , \quad (2\text{-}19)$$

or

$$\frac{\eta_k}{N} = \frac{3}{2} \frac{L}{\ell} \left(\frac{2m}{M}\right)^{1/2} (\omega_p \ \Delta t) \ . \qquad (2\text{-}20)$$

For ease of calculation, η_k should be a rational number; then one can inject either η_k ions each step or one ion each $(1/\eta_k)$th step. One can achieve this convenience, for given ratios L/ℓ and m/M, by adjustment of $\omega_p \ \Delta t$.

One interesting ion engine characteristic to be determined from the calculation is the potential of the spaceship relative to space. This may be obtained by integrating the electric field from the sheet farthest out from the ship. The potential of the spaceship in the presence of only the Nth charged sheet in space is

$$\varphi_N = - \left(\pm \frac{q_s}{\epsilon_o}\right) x_N \quad .$$

Thus

$$\varphi = -\sum \frac{q_s}{\epsilon_o} (x_i - x_e) \tag{2-21}$$

(sum over all sheets in Region C).

Normalizing and substituting from Eq. 2-11 , we obtain

$$\frac{\varphi}{\varphi_o} = -\left[\frac{1}{N\left(\frac{3L}{2\ell}\right)^2}\right] \sum \left[\frac{x_i}{\ell} - \frac{x_e}{\ell}\right] \tag{2-22}$$

Another quantity of interest is the number of sheets per Debye length. Defining for the purpose of these calculations the Debye length in terms of the thermal energy in a Debye sphere,

$$\lambda_D^2 = \frac{kT}{m_e(\omega_{p_e})^2} \quad . \tag{2-23}$$

Substituting for the plasma frequency and dividing numerator and denominator by φ_o, we obtain

$$\left(\frac{\lambda_D}{\ell}\right)^2 = \left(\frac{kT}{e\varphi_o}\right)\left(\frac{3L}{2\ell}\right) \quad . \tag{2-24}$$

C. Calculation of Actual Thrust Per Unit Area

In the computer calculations the electric field adjacent to the electrodes will be known. The electrodes are assumed to be thin grids for the purpose of these calculations. Since an electric field change occurs when passing from one side of the grid to the other, an equivalent charge can be assumed to be present on the grid. This charge per unit area q_{s1} is equal to $\epsilon_o (E_{right} - E_{left})$. The force per unit area on the grid is $T = (q_{s1}/g)(E_{right} + E_{left})/2$, where the mean of the sum of the electric fields on both sides of the grid is used. Thus

$$T = \frac{\epsilon_o}{2g} (E_{right}^2 - E_{left}^2) \; * \quad . \quad (2\text{-}25)$$

For the region between the genode and the accel grid, a Child-Langmuir distribution has been assumed. Thus, the field at the genode surface is zero, so that we have only two grids to consider, the accel grid and the electron emitter decel grid (see Fig. 2-1). The field to the left of the accel grid from the Child's law (Eq. 2-8) is

$$E_4 = 2\left(\frac{\rho\varphi_o}{\epsilon_o}\right)^{1/2} \quad . \qquad (2\text{-}26)$$

---

* A positive thrust indicates that a drag on the ship as a positive force is a force to the right and, consequently, from the ship's viewpoint, a retarding force.

Now let E_1 be the field immediately to the right of the electron emitter, E_2 the field immediately to the left of the electron emitter, and E_3 the field to the right of the accel grid. Then the total actual thrust per unit area on the ship is

$$T = \frac{\epsilon_o}{2g}\left[E_1^{\,2} - E_2^{\,2} + E_3^{\,2} - \frac{4\rho\varphi_o}{\epsilon_o}\right] \quad . \qquad (2\text{-}27)$$

Assuming Region B to be bounded by metal grids, the field immediately to the left of $x/\ell = 1$ is

$$E_2 = E_{dc} + \frac{q_s}{\epsilon_o}\left[\sum \frac{x_i}{\ell} - \sum \frac{x_e}{\ell}\right] \quad , \qquad (2\text{-}28)$$

where the summations are over all ions in Region B and all electrons in Region B, respectively. The field to the right of the accel grid is

$$E_3 = E_{dc} + \frac{q_s}{\epsilon_o}\left[\sum \frac{\ell - x_e}{\ell} - \sum \frac{\ell - x_i}{\ell}\right] \quad , \qquad (2\text{-}29)$$

where the summations are over all ions and electrons in Region B, and E_{dc} is given by

$$E_{dc} = \frac{\varphi_1}{\ell} \quad . \qquad (2\text{-}30)$$

The field to the right of the electron emitter equals

$$E_1 = \gamma_3^* \frac{q_s}{\epsilon_o} \quad , \qquad (2\text{-}31)$$

where γ_3^* is the number of excess electron sheets to the right of the electron emitter. (See symbol list for definition of symbols.) Forming $E_3^2 - E_2^2$, we obtain

$$\frac{\epsilon_o^2}{q_s}(E_3^2 - E_2^2) = \left[\left(\frac{\varphi_1\epsilon_o}{\ell q_s} + \sum_{\substack{\text{all elec-}\\\text{trons}}}\left(1-\frac{x_e}{\ell}\right) - \sum_{\substack{\text{all}\\\text{ions}}}\left(1-\frac{x_i}{\ell}\right)\right)^2 - \left(\frac{\varphi_1\epsilon_o}{\ell q_s} + \sum_{\substack{\text{all}\\\text{ions}}}\frac{x_i}{\ell} - \sum_{\substack{\text{all elec-}\\\text{trons}}}\frac{x_e}{\ell}\right)^2\right] . \tag{2-32}$$

By letting N_e = total number of electron sheets in Region B and N_i = total number of ion sheets in Region B, we rewrite Eq. 2-32 in the form

$$\frac{\epsilon_o^2}{q_s^2}(E_3^2 - E_2^2) = 2(N_e - N_i)\left[\frac{\varphi_1\epsilon_o}{\ell q_s} + \sum\frac{x_i}{\ell} - \sum\frac{x_e}{\ell} + \frac{N_e - N_i}{2}\right] . \tag{2-33}$$

Thus, substituting Eq. 2-23 into Eq. 2-27 and normalizing, we obtain

$$\frac{Tg\ell}{\varphi_o q_s} = \frac{\ell q_s}{2\varphi_o\epsilon_o}\left[\gamma_3^{*2} + 2(N_e - N_i)\left(\frac{\varphi_1\epsilon_o}{\ell q_s} + \sum\frac{x_i}{\ell} - \sum\frac{x_e}{\ell} + \frac{N_e - N_i}{2}\right) - \frac{4\rho\,\varphi_o\epsilon_o}{q_s^2}\right] \tag{2-34}$$

Substituting

$$\rho = \frac{Nq_s}{\ell}$$

and

$$\frac{\varphi_o}{q_s} = \frac{9}{4}\frac{NL^2}{\epsilon_o \ell}$$

into Eq. 2-34, we obtain for the normalized actual thrust per unit area

$$\frac{Tg\ell}{\varphi_o q_s} = \frac{1}{2N\left(\frac{3L}{2\ell}\right)^2}\left[\gamma_3^{*2} + 2\,(N_e - N_i)\left[N\left(\frac{\varphi_1}{\varphi_o}\right)\left(\frac{3L}{2\ell}\right)^2 + \sum\frac{x_i}{\ell} - \sum\frac{x_e}{\ell} + \frac{N_e - N_i}{2}\right] - (2N)^2\left(\frac{3L}{2\ell}\right)^2\right]. \tag{2-35}$$

From this thrust equation some interesting observations can be made:

1. The third term within the main bracket is the largest term and is negative. This indicates a force which accelerates the ship in the proper direction.

2. If the number of ions and electrons in Region B are equal, there is no retardation of

the ions by the decel grid (electron emitter). In practice, however, this lack of retardation will not be observed since the electrons would then be intercepting the accel grid - an undesirable condition.

3. Any field on the surface of the ship (to the right of the electron emitter) results in loss of thrust. γ_3^2, whether γ_3 is positive or negative, is always positive, thus giving thrust loss.

D. Calculation of Ideal Thrust Per Unit Area

Ideal thrust occurs if complete mixing takes place outside the ship in Region C, and sufficient mixing occurs in Region B to result in the ions being decelerated by the decel grid potential φ_1.

We can obtain an ideal value for the thrust by assuming that all ions leave the ship after being accelerated to the potential of the grid $(\varphi_o + \varphi_1)$, wherein φ_1 is a negative number.

The thrust per unit area from ion ejection is:
Thrust/unit area = momentum/unit time and unit area =

$$T^* = \left(\frac{\eta_k}{\Delta t}\right) \left(\frac{q_s}{e} M\right) \left(\frac{1}{g}\right) v_i \qquad (2\text{-}36)$$

number of ion sheets per unit time

mass per unit area per sheet

mass to weight conversion

exit ion velocity $\Delta x_1/\Delta t$

or

$$T^* = \frac{\eta_k}{\Delta t} \frac{q_s}{e} \frac{M}{g} \ell \frac{\Delta(\frac{x_i}{\ell})}{\Delta t} \tag{2-37}$$

In Equation 2-7 we calculated the normalized difference $\Delta(x_i/\ell)$ for injection into Region B. To obtain the ideal injection into Region C we substitute $\varphi_o + \varphi_1$ for φ_o in that equation and utilize Eq. 2-11 defining the number N:

$$\Delta\left(\frac{x_i}{\ell}\right) = (\omega_p \Delta t)\left(\frac{3L}{2\ell}\right)\left(\frac{2m}{M}\right)^{1/2}\left(1 + \frac{\varphi_1}{\varphi_o}\right)^{1/2} . \tag{2-38}$$

Using Eqs. 2-6a and 2-10 in connection with Eq. 2-38, we can rewrite Eq. 2-37 in the normalized form as given by the following equation:

$$\frac{T^* g\ell}{\varphi_o q_s} = \frac{2\eta_k}{\omega_p \Delta t} \frac{\left(1 + \frac{\varphi_1}{\varphi_o}\right)^{1/2}}{\left(\frac{3L}{2\ell}\right)\left(\frac{2m}{M}\right)^{1/2}} \tag{2-38a}$$

Substituting Eq. 2-20 into Eq. 2-20 into Eq. 2-38a, we obtain for the normalized ideal thrust

$$\frac{T^* g\ell}{\varphi_o q_s} = 2N\left(1 + \frac{\varphi_1}{\varphi_o}\right)^{1/2} \tag{2-39}$$

E. Comparison Between Ideal and Actual Thrust

The ratio of actual thrust to ideal thrust can be formed by combining Eqs. 2-35 and 2-39:

$$\frac{T}{T^*} = \frac{1}{4\left(\frac{3L}{2\ell}\right)^2 \left(1 + \frac{\varphi_1}{\varphi_o}\right)^{1/2} N^2} \left[\gamma_3^{*2} + 2(N_e - N_i)\left[N\left(\frac{\varphi_1}{\varphi_o}\right)\left(\frac{3L}{2\ell}\right)^2 \right.\right.$$

$$\left.\left. + \sum \frac{x_i}{\ell} - \sum \frac{x_e}{\ell} + \frac{N_e - N_i}{2} \right] - (2N)^2 \left(\frac{3L}{2\ell}\right)^2 \right] . \qquad (2\text{-}40)$$

This relationship between the actual thrust and the ideal thrust is output from the computer at every step so that the engine performance can be related to the mixing of the ions and electrons.

F. Random Electron Emission Velocity

The probability P of an electron having a velocity v in the cathode is:

$$P(v)\ dv = \frac{e^{-\frac{mv^2}{2kT}}}{k\ T/m}\ dv \quad , \tag{2-41}$$

but the probability of an electron being emitted from the cathode surface with velocity v is

$$P^*(v)\ dv = \frac{2v}{\frac{2kT}{m}}\ e^{-\frac{mv^2}{2kT}}\ dv \quad , \tag{2-42}$$

or

$$P^*(v)\ dv = e^{-\frac{mv^2}{2kT}}\ d\left(\frac{mv^2}{2kT}\right) \quad . \tag{2-43}$$

The integrated or accumulated probability distribution is

$$\int_0^{v_e} P(v)\ dv = 1 - e^{-\frac{mv_e^2}{2kT}} \quad . \tag{2-44}$$

Now we can choose random numbers from a uniform distribution between 0 and 1. Calling this random number 1-R, we let

$$1-R = 1-e^{-\frac{mv^2}{2kT}} \tag{2-45}$$

Since 1-R is just as random as R over the domain from 0 to 1, we can take the logarithm,

$$\ell n\ R = \ell n \left[e^{-\frac{vm^2}{2kT}} \right] \tag{2-46}$$

or

$$v_e = \left[-\frac{2kT}{m}\ \ell n\ R \right]^{1/2} \quad . \tag{2-47}$$

Forming the finite difference for computer calculations, we obtain

$$\Delta \left(\frac{x_e}{\ell} \right) = \frac{v_e \Delta t}{\ell} = \left[-\frac{2kT}{m}\ \ell n\ R \right]^{1/2} \frac{\Delta t}{\ell} \quad . \tag{2-48}$$

Normalizing with the use of Eqs. (2-6a) and (2-10) we obtain:

$$\Delta \left(\frac{x_e}{\ell} \right) = (\omega_p \Delta t) \left(\frac{3L}{2\ell} \right) \left(\frac{2kT/e}{\varphi_o} \right)^{1/2} (-\ell n\ R)^{1/2} \quad . \tag{2-49}$$

The above information was programmed into the one-dimensional program.

G. Integrated Plasma Potentials

Of interest in understanding the plasma behavior is the electric potential within the plasma. Since time varying fields exist within the plasma, it is not strictly correct to call the integrated electric field an energy function. Nevertheless, it will be instructive to calculate a potential by integrating the fields that exist within the plasma.

In the model chosen for the analysis, the electric field and electric potential are zero at x equals-infinity. Thus, we start at large x where E is 0 and integrate inwards to find the potential.

Now the field in the plasma is

$$E = \frac{\overset{*}{\gamma}\, q_s}{\epsilon_o} \quad , \tag{2-50}$$

where $\overset{*}{\gamma}$ is the number of electron sheets to the right minus the number of ion sheets to the right in the plasma. Now,

$$\varphi_p = - \int E \cdot dx \tag{2-51}$$

and

$$\varphi_p = - \sum E_i \, \Delta x_i \quad , \tag{2-52}$$

where E_i is the field between the sheets i and i+1, and Δx_i is the distance between the two sheets.

Substituting from Eq. 2-11, and normalizing Eq. 2-52, the following is obtained:

$$\frac{\varphi_p}{\varphi_o} = \frac{q_s \ell}{\epsilon_o \varphi_o} \sum \gamma_i^* \Delta \left(\frac{x}{\ell}\right)_i \tag{2-53}$$

or

$$\frac{\varphi_p}{\varphi_o} = \frac{1}{N \left(\frac{3L}{2R}\right)^2} \sum \gamma_i^* \Delta \left(\frac{x}{\ell}\right)_i \quad . \tag{2-54}$$

A running record of the normalized potential is recorded at every ion and electron sheet position. These potentials are then plotted vs. the normalized position variable x/ℓ.

In Region B between the accelerator grid and the decelerator-emitter grid, a slightly different formulation is involved because of the dc potential.

In Region B,

$$E = E_1 + \frac{\overset{*}{\gamma}\, q_s}{\epsilon_o} \tag{2-55}$$

H. Definitions of Symbols used in One-Dimensional Configuration

E	electric field
e	electron charge
g	gravitational constant
J	ion current density = charge/unit area injected from left at $x = 0$, per unit time
L	interval length between ion emitter and accel grid
ℓ	interval length between accel and decel grid or electron emitter
M	ion mass
m	electron mass
N	number of ion sheets in Region B if ions proceeded at injection velocity
P	probability distribution of electrons in velocity space
P^*	probability distribution of electrons being emitted from a cathode in velocity space
q_s	charge per unit area for each sheet
R	random number from a uniform distribution, $0 < R \leq 1$
T	thrust per unit area
T^*	ideal thrust per unit area
u_o	ion injection velocity
x_e	position of electron sheet
x_i	position of ion sheet
Z	normalized position variable x/ℓ
γ	twice the number of electron sheets to the right minus twice the number of ion sheets to the right ± 1 (+1 for an electron sheet) (-1 for an ion sheet)
γ^*	number of electron sheets to the right minus the number of ion sheets to the right
ϵ_o	dielectric constant of free space
η_k	number of ion sheets injected at each time step
ρ	ion charge density at injection and also the electron charge density standard
φ	potential of ship relative to space

φ_o potential between ion emitter and accel grid

φ_1 potential between accel grid and electron emitter

ω_p plasma frequency

III. ONE-DIMENSIONAL RESULTS

A. Review of the Computer Model

Our model is, for the first part of the program, one-dimensional; ions and electrons are idealized into sheets of charge. We inject cold ions through the accel grid and electrons from a hot decel grid with a Gaussian velocity distribution. We study the situation both upstream and downstream of the decel grid (see Fig. 3-1).

All of the dynamical equations of the system are programmed into a high speed digital computer with the variables in completely normalized form. These input variables are:

$\frac{L}{\ell}$	Ratio of distance between the ion emitter and the accelerator grid to the distance between the accelerator grid and decelerator-emitter grid
$\frac{M}{m}$	Ratio of ion mass to electron mass
$\frac{\varphi_1}{\varphi_o}$	Ratio of the potential between the accelerator grid and the decelerator-emitter grid to the potential between the ion emitter and the accelerator grid
$\frac{kT}{e\varphi_o}$	Ratio of mean electron energy to potential difference between ion emitter and accelerator grid
η_i	Number of ion sheets injected per time step
$\frac{\eta_e}{\eta_i}$	Ratio of electron sheets injected per time step to the number of ion sheets injected per time step
N	Approximate number of ion sheets between the accelerator grid and the decelerator-emitter grid

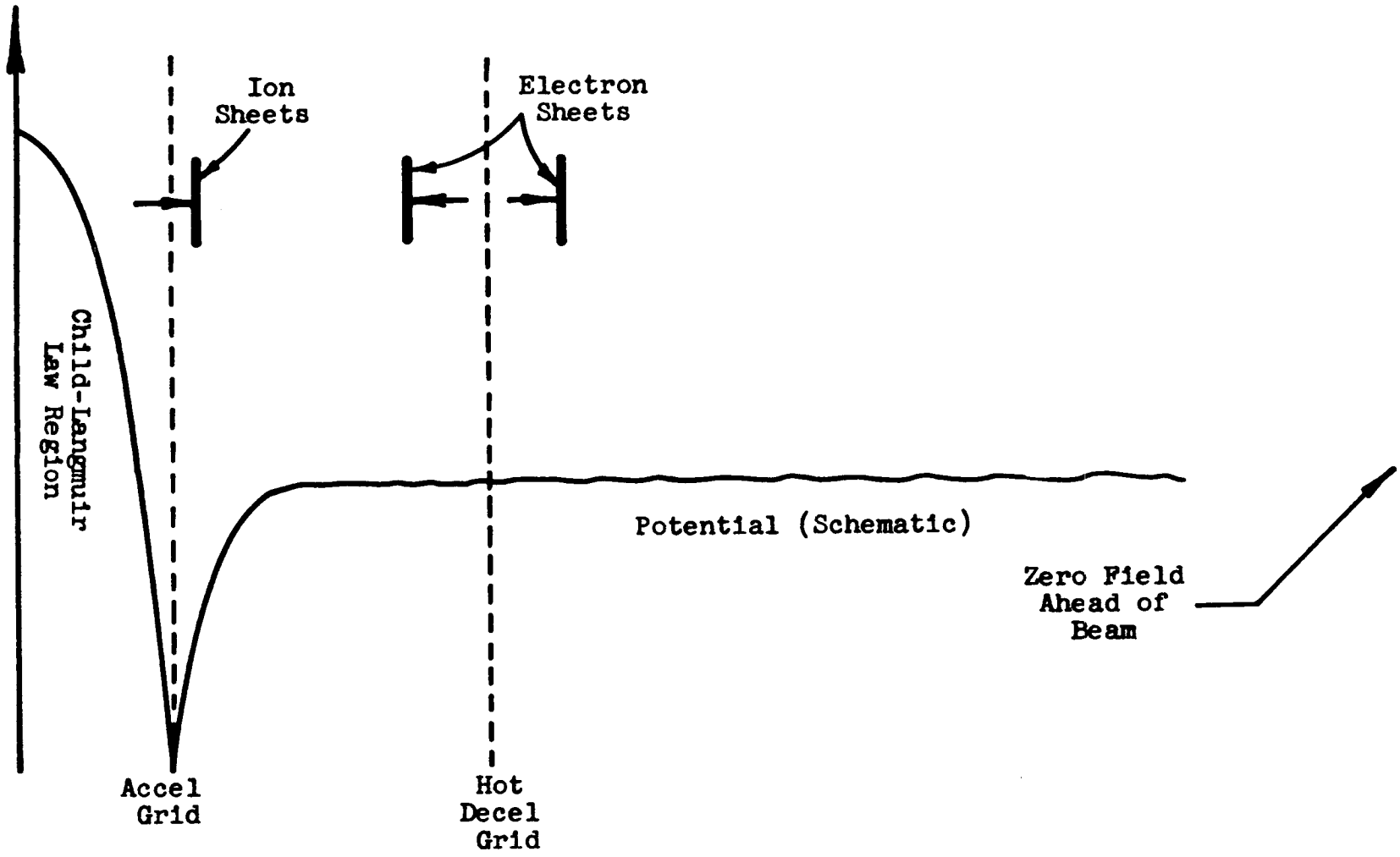

ONE DIMENSIONAL MODEL

Fig. 3-1

The output variables from the computer are:

$\frac{\varphi_{ship}}{\varphi_o}$ Ratio of the integrated spaceship potential at each time step to φ_o

$\frac{T_{actual}}{T_{ideal}}$ Ratio of the force exerted on the ship by all the charged sheets to the ideal force on the ship calculated at each time step from the change in momentum one would expect if the ions left the ship with energy $\varphi_o - \varphi_1$

$\frac{\varphi_p}{\varphi_o}$ Ratio of φ_p the potential in the plasma to φ_o as a function of distance from the accelerator grid. The potential is found by integrating the electric field in the plasma from the sheet farthest out to the accelerator grid

The electron current density is variable. Half of the temperature-limited electron current is injected upstream and half downstream. The electron sheets injected upstream are returned by the negative decelerator potential and made available for downstream mixing after passing through their emitting grid again. However, a grid interception rate of one in four passes is programmed for electron sheets. No ion-electron collisions have been programmed.

Injection of electrons from the hot grid began simultaneously with the entry of the first ions through the accelerator grid. The system was followed until the head of the beam had penetrated to a maximum of 150 inter-grid distances out into space.

The thrust was monitored throughout, as the actual force on the supposedly rigid grid system (see Fig. 3-1).

B. Plots Made from the Calculations

Zero field was imposed as the condition in free space ahead of the beam, and the ship was left to find its own potential relative to space. This potential was monitored, although fields only (not potentials) were required for tracing the charges.

The instantaneous potential is calculated as a function of distance for many successive time steps in several cases.

Time displacement graphs of some of the particles are also traced automatically for several cases.

The numerical procedure employed approximately twenty-two time steps per complete plasma oscillation for a typical calculation. (See variable $2\pi/\omega_p\Delta t$.) The charge continuum is coarse-grained into discrete sheets such that there are up to ten sheets of each species per Debye length (for N = 240). However, coarser models, down to only just over one sheet per Debye length (N = 30), were also tried.

Electrons and ions were emitted at regular time intervals. The injection velocity of the ions was fixed while that of the electrons was picked randomly from a Gaussian distribution at the specified temperature.

C. General Results

A good plasma was formed, mixing was almost perfect, and the thrust maintained its ideal value after a brief

initial adjustment in all cases except where prevented by a deficiency of electrons.

No electrons penetrated through the accel grid. They were repelled at a certain distance upstream of their source, with only ions beyond. The upstream boundary of the plasma lies exactly where predicted from the theory of self-consistent ion flow between the accel grid and the plasma. This theory is developed in Section 3E.

Ions made turn-arounds only when a deficiency of electrons was allowed to develop. Electrons randomly drifted about through the entire plasma. The advancing head of the beam acted as an electron reflector. The head seemed to become more and more diffuse. There appeared to be a forward acceleration in space of the first ions, perhaps due to plasma pressure.

No distinct "plasma puffs" developed; i.e., self-contained advanced groups of ions holding in their own electrons.

A slight tendency toward electron sheath formation at the hot grid was apparent. This sheath was intuitively predicted as a device for keeping back unwanted excess electrons.

Fields (potential gradients) remained moderate throughout the plasma, and the electrons did not acquire unduly high energies about their initial kT unless an electron deficiency developed.

However, there were marked potential fluctuations. In space these fluctuations seemed to become less violent as the number of sheets per Debye length was increased. Also a longer time was needed for the fluctuations to build up when more sheets were used.

In time, however, they remained at an unexpectedly high level and occurred with electron plasma frequency.

Certainly, it is felt that an ion engine similar to the model described here will work in space and provide thrust. The electron plasma frequency oscillation reported here have not been confirmed by all experiments, but one must keep in mind their longitudinal and very high frequency nature, and hence the difficulty in observing them. With electric fields of rapid time variance, it is not correct to talk about potentials as energy functions. Even though relatively large integrated potentials appear at the ship, electron velocities much greater than the electron injection velocity are not observed. Thus, these fluctuations in spaceship potential are not detrimental to the performance of the engine, but, on the contrary, provide the mechanism by which the beam is neutralized.

D. Detailed Results and Discussion

Several cases of emission and velocity for electrons and ions were simulated for several values of mass ratio. These results have already been described in detail in Quarterly Reports 3 and 4. Some of the most significant results are presented in this report. Figure 3-1 shows a schematic of the potential distribution for the one-dimensional configuration. Typical ion and electron trajectories for the case where $M/m = 1800$ are given in Figs. 3-2 and 3-3, respectively, while the variation of the ship potential as a function of time for the same case is shown in Fig. 3-4. A three-dimensional plot for the potential as a function of beam-front distance and time is shown in Fig. 3-5. In this case the fluctuations do not seem to be detrimental to the ion engine performance. Figures 3-6 through 3-9 show the plots of ion trajectories, ship potential and thrust for the case of $M/m = 576$ (the other parameters are indicated on the various figures). The bunching of the ions around $T/\Delta t = 900$ may be noticed in Fig. 3-6; its effect on potential and thrust may be noticed in Figs. 3-7 and 3-9, respectively. Figure 3-8 shows the variation of the integrated potential as a function of beam distance from the ship for different time intervals. The deterioration in the ion engine performance, as noticed from these plots, seems to be

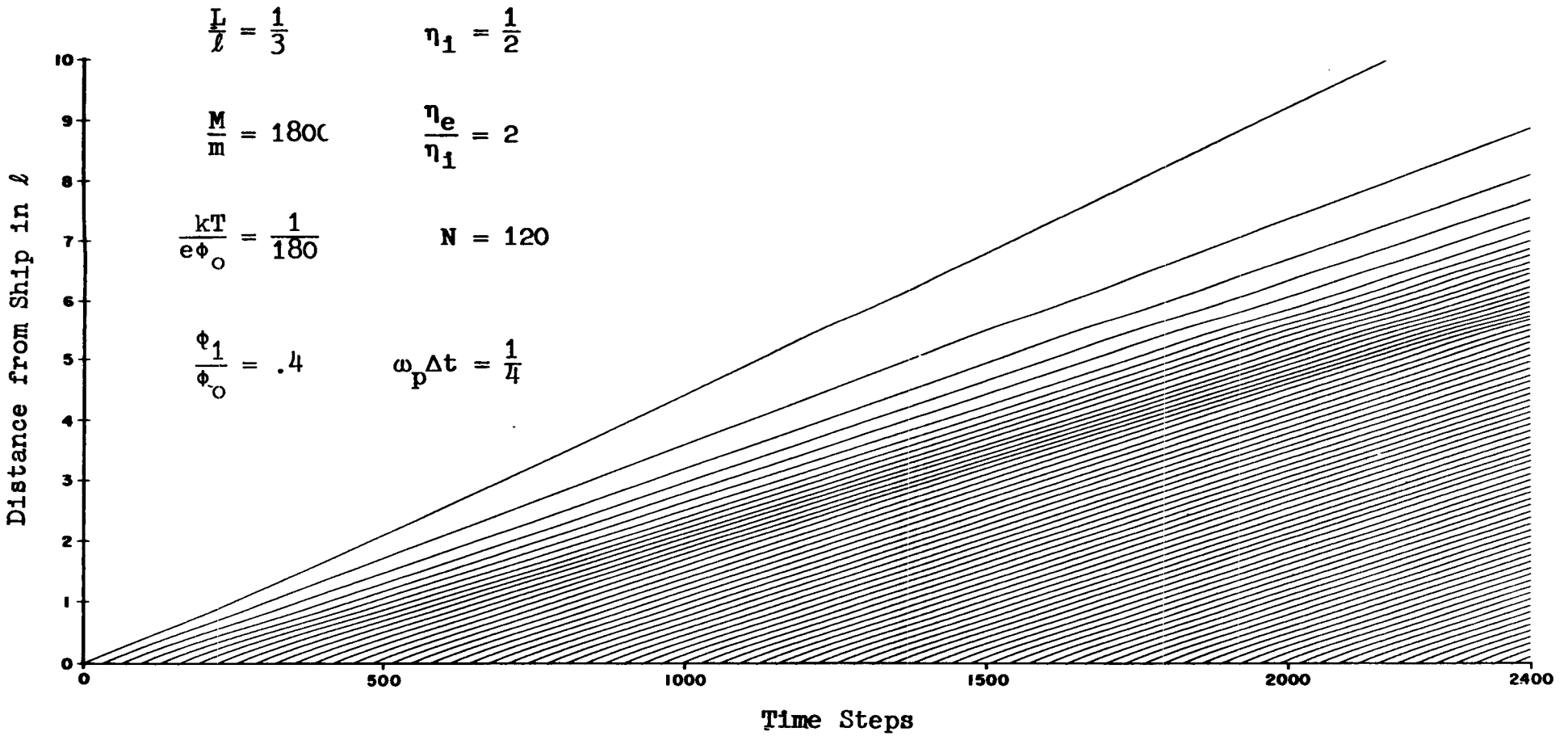

ION TRAJECTORY PLOT

Fig. 3-2

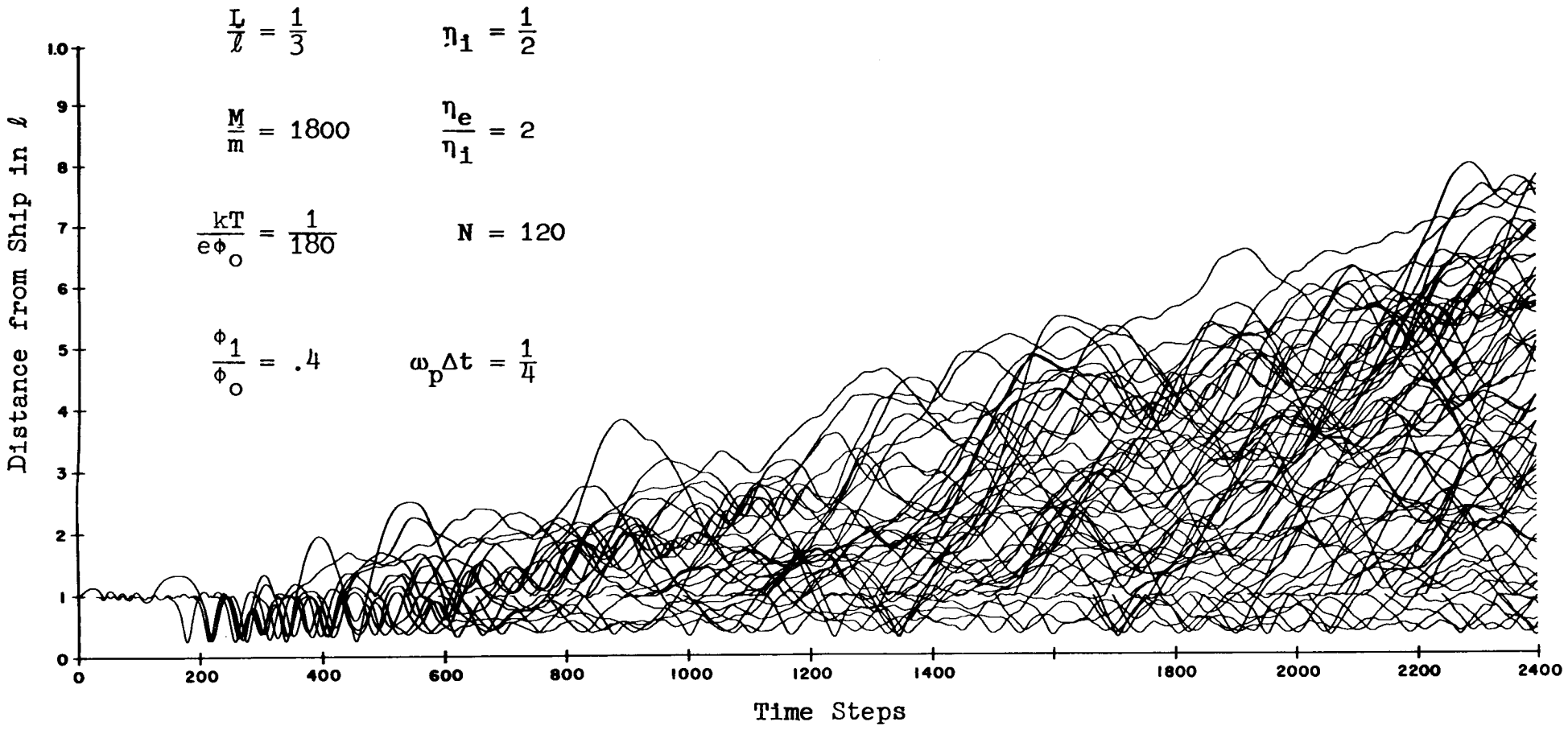

ELECTRON TRAJECTORY PLOT

Fig. 3-3

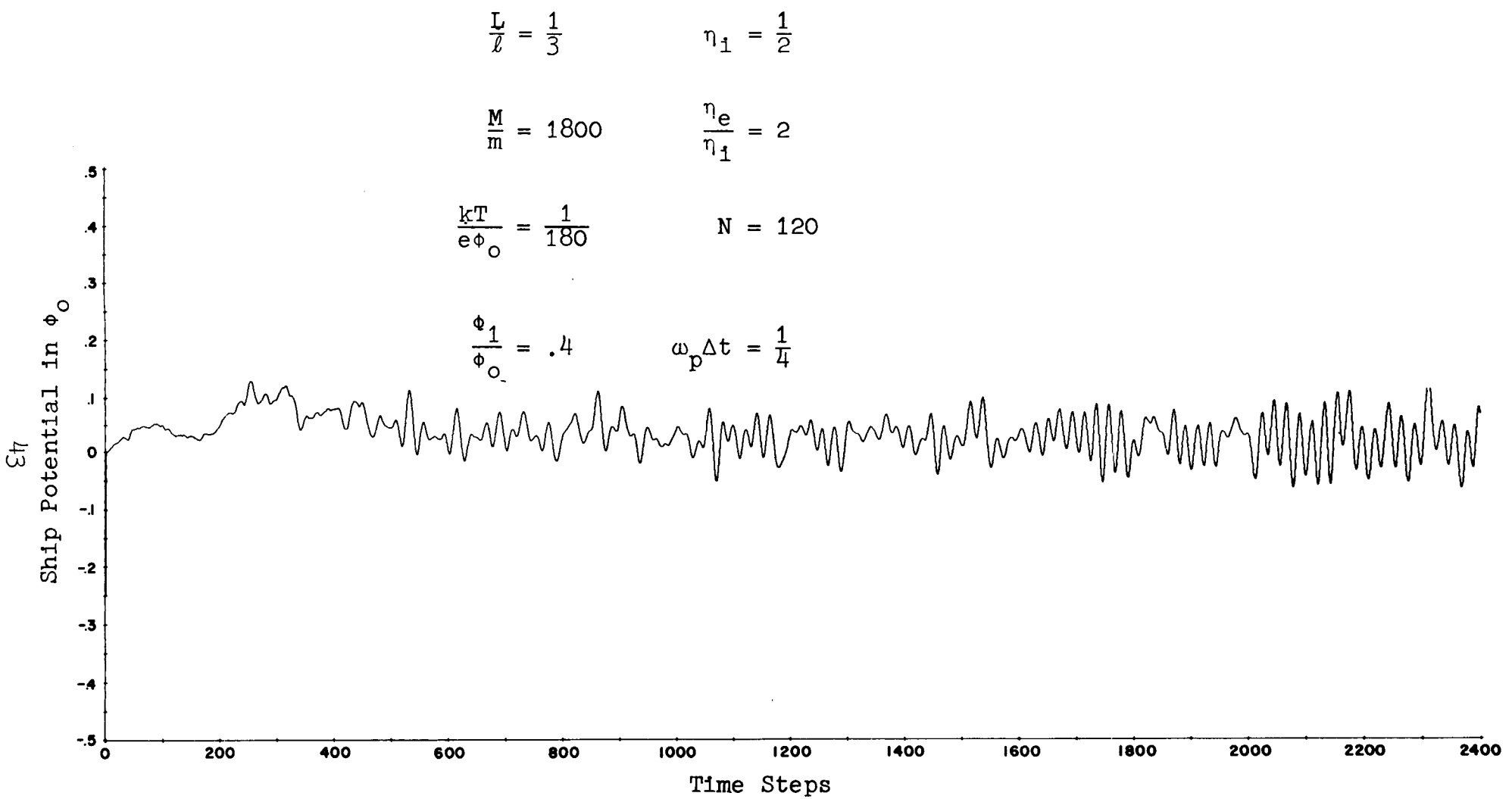

SHIP POTENTIAL VS. TIME

Fig. 3-4

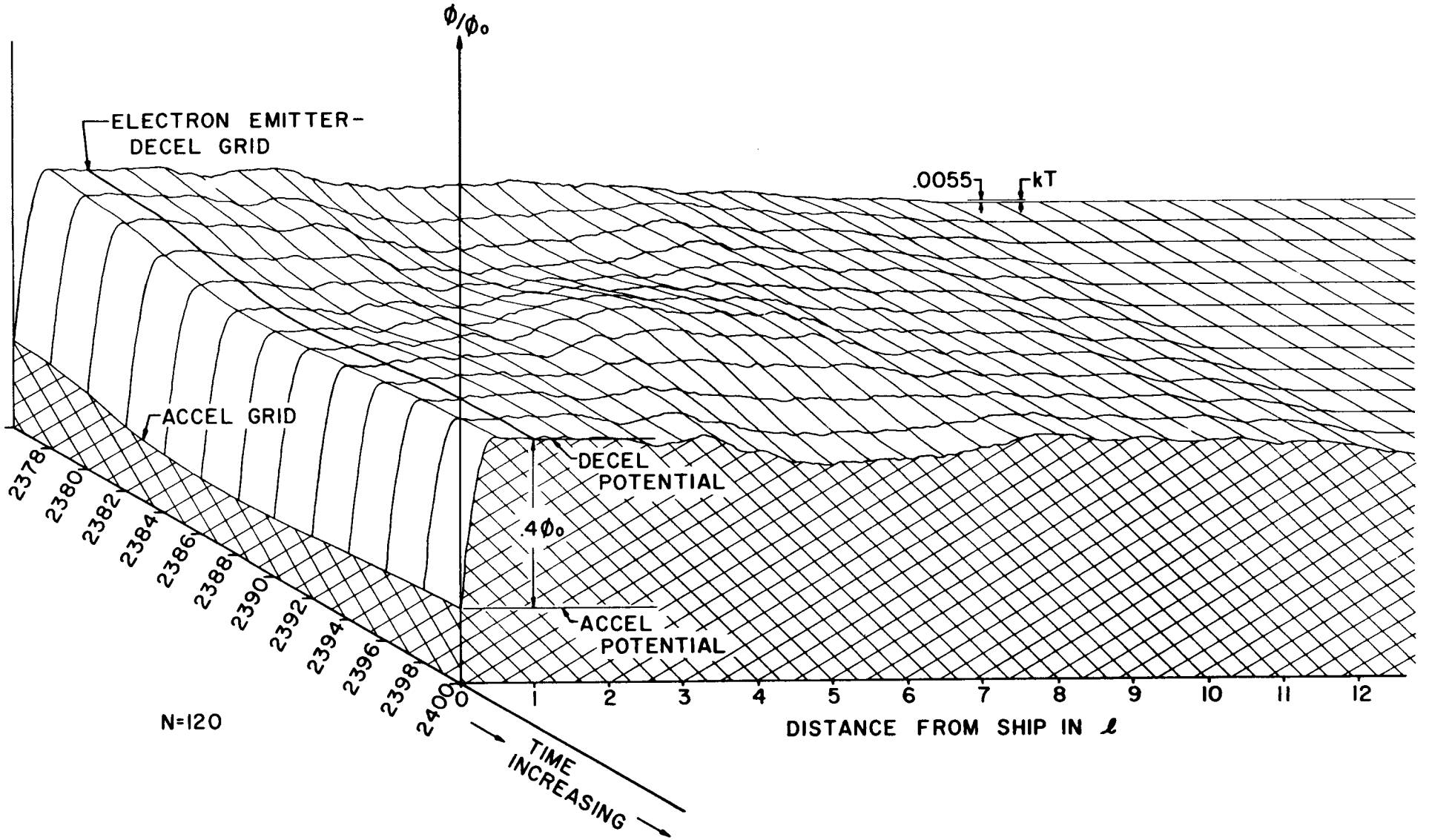

INTEGRATED POTENTIALS, TIME-DISTANCE PLOTS

Fig. 3-5

$\frac{3L}{2\ell} = \frac{1}{2}$ $\frac{2kT}{e\varphi_o} = \frac{2}{64}$ $\eta_i = 2$ $N = 80$

$\frac{2m}{M} = \frac{2}{576}$ $\frac{\varphi_1}{\varphi_o} = \frac{4}{10}$ $\frac{\eta_e}{\eta_i} = 2$ $\frac{2\pi}{\omega_p \Delta t} = 7.40$

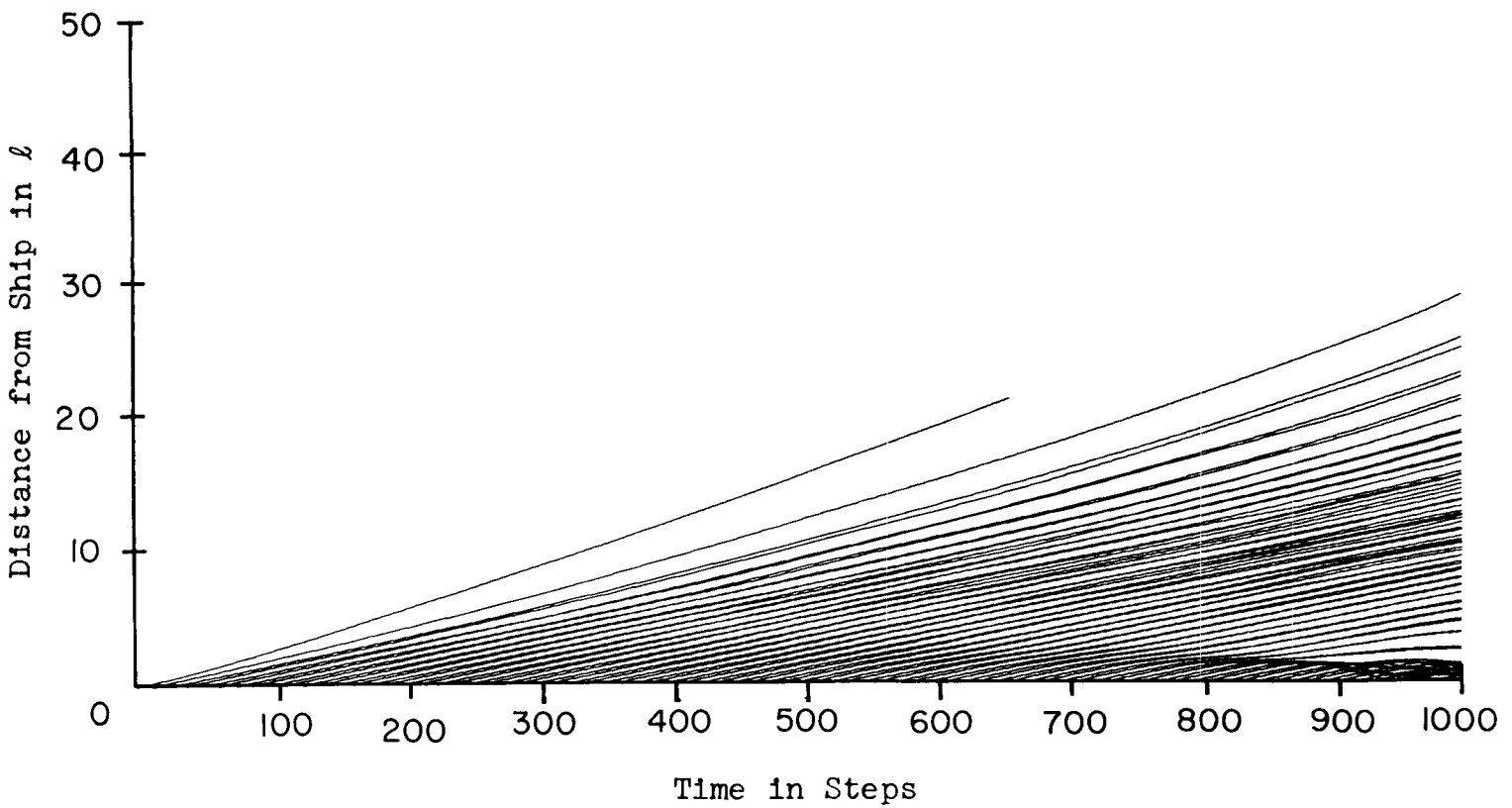

ION TRAJECTORY PLOT (RUN 12B)

Fig. 3-6

$\frac{3L}{2\ell} = \frac{1}{2}$ $\quad \frac{2kT}{e\varphi_o} = \frac{2}{64}$ $\quad \eta_i = 2$ $\quad N = 80$

$\frac{2m}{M} = \frac{2}{576}$ $\quad \frac{\varphi_1}{\varphi_o} = \frac{4}{10}$ $\quad \frac{\eta_e}{\eta_i} = 2$ $\quad \frac{2\pi}{\omega_p \Delta t} = 7.40$

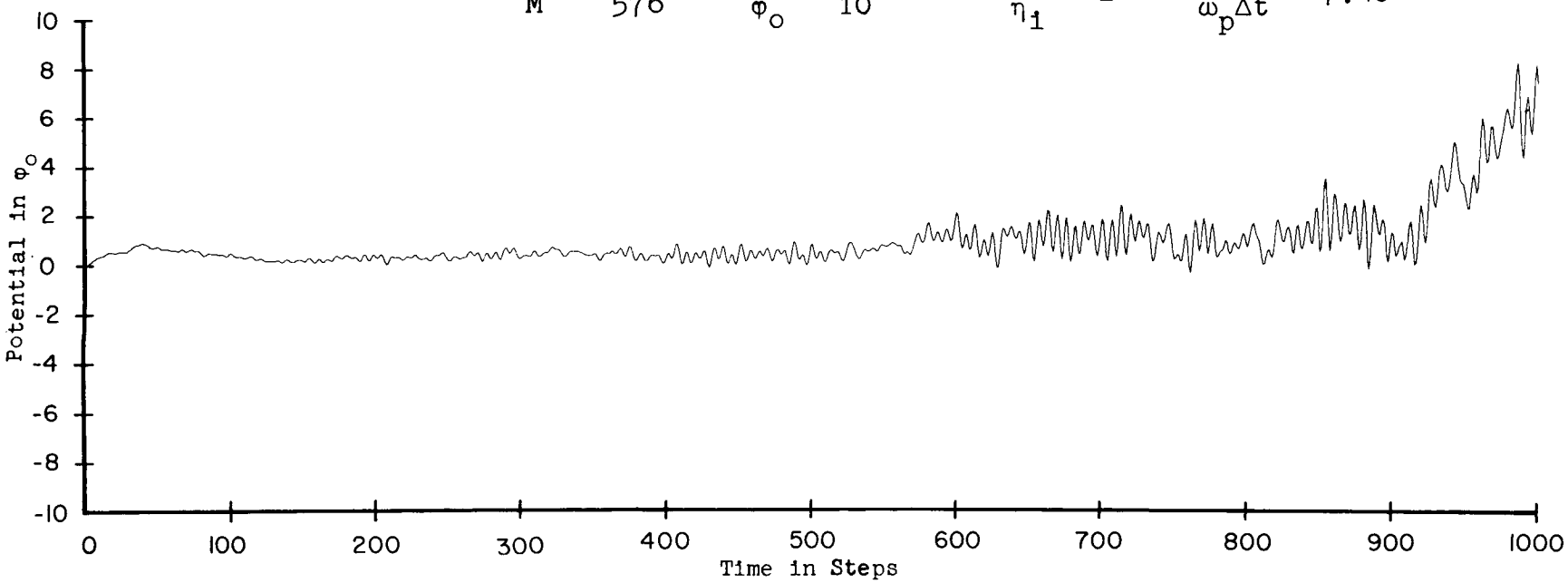

SHIP POTENTIAL VERSUS TIME (RUN 12B)

Fig. 3-7

$$\frac{3L}{2\ell} = \frac{1}{2} \qquad \frac{2kT}{e\varphi_o} = \frac{2}{64} \qquad \eta_1 = 2 \qquad N = 80$$

$$\frac{2m}{M} = \frac{2}{576} \qquad \frac{\varphi_1}{\varphi_o} = \frac{4}{10} \qquad \frac{\eta_e}{\eta_1} = 2 \qquad \frac{2\pi}{\omega_p \Delta t} = 7.40$$

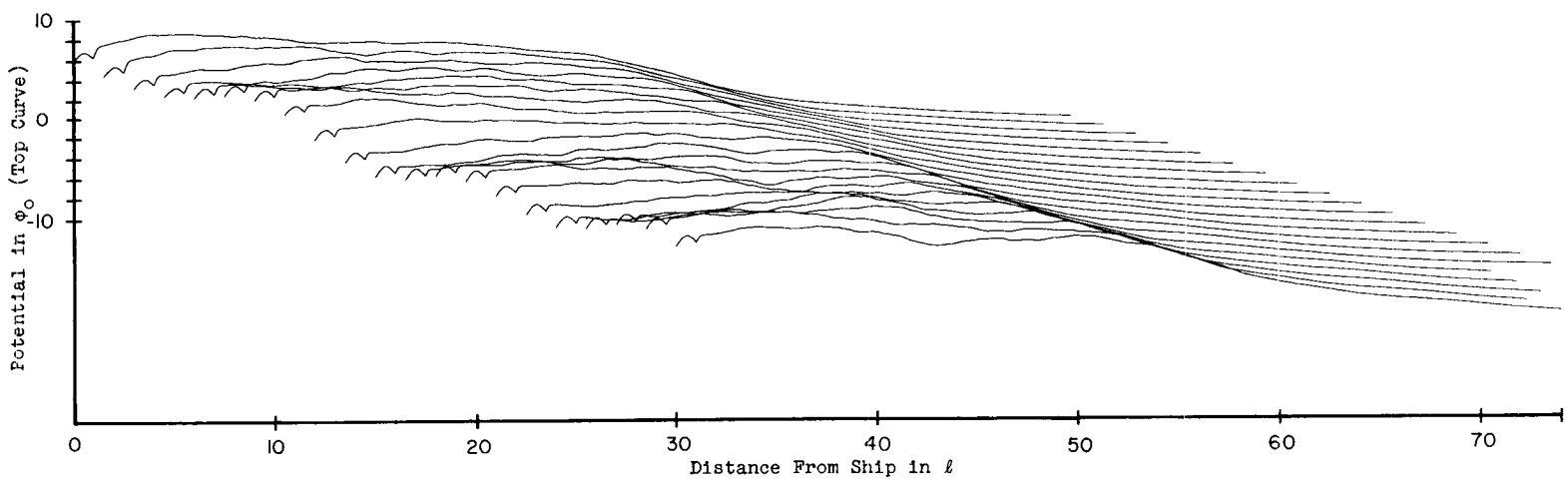

INTEGRATED POTENTIAL VS. DISTANCE (RUN 12B)
(Time Steps 980 to 1000)

Fig. 3-8

$\frac{3L}{2\ell} = \frac{1}{2}$ $\frac{2kT}{e\varphi_o} = \frac{2}{64}$ $\eta_1 = 2$ $N = 80$

$\frac{2m}{M} = \frac{2}{576}$ $\frac{\varphi_1}{\varphi_o} = \frac{4}{10}$ $\frac{\eta_e}{\eta_1} = 2$ $\frac{2\pi}{\omega_p \Delta t} = 7.40$

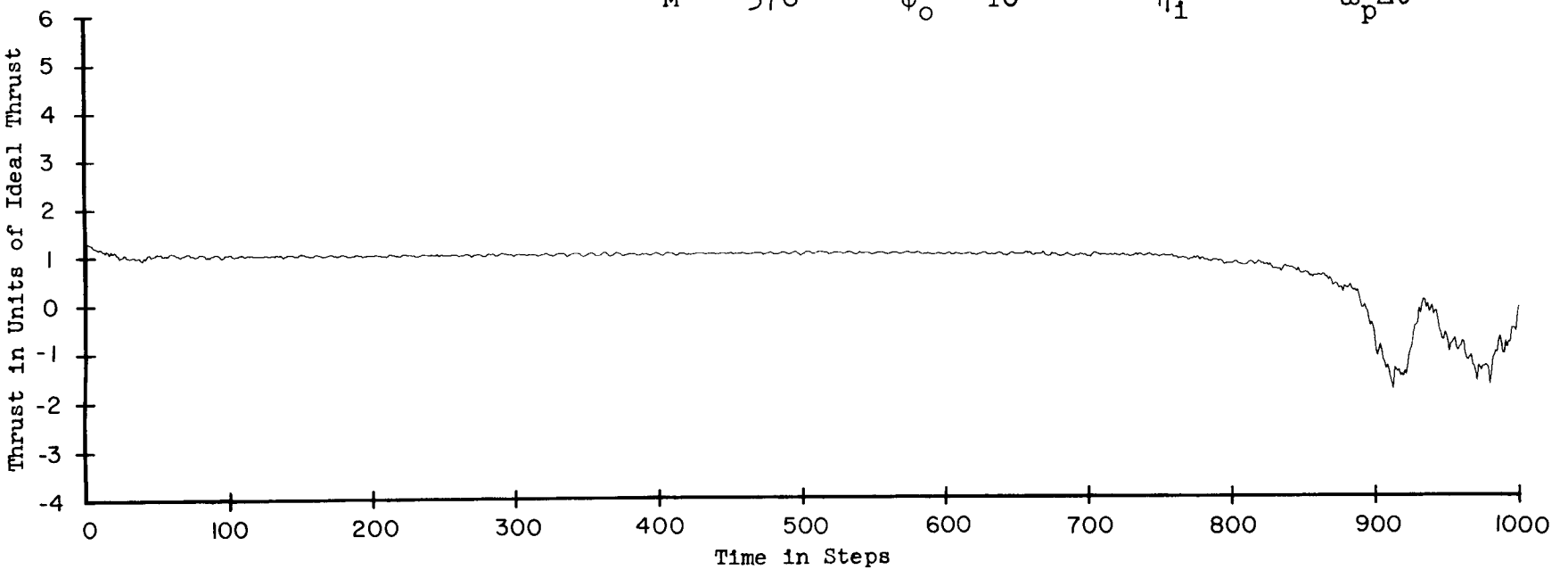

THRUST VS. TIME (RUN 12B)

Fig. 3-9

due to deficiency of electrons. An increase in electron emission did not show any such deterioration in ship potential and thrust, as shown in Figs. 3-10 and 3-11. The electron trajectories in both cases were similar to those shown in Fig. 3-3.

Subsequent calculations were made with both the large and small time steps. When large time steps are used, instabilities, if they exist with a certain set of parameters, will develop sooner in time and will then be observed. However, if small time steps are used, these instabilities may never be seen, because insufficient time is allowed for build-up. That is to say, when an inherently unstable calculation is being made, the instability will manifest itself sooner when additional noise is fed into the system by a large discrete time step.

Figures 3-2 through 3-5, given above, are plots of results of a one-dimensional calculation for hydrogen. The calculation was completed for 95.5 electron plasma periods, and good mixing and thrust were observed. Figures 3-11 through 3-14 are the same run, except that $N = 60$, and the calculations are carried out to 318 plasma periods. Observe the continuous build-up in time of the potential fluctuations in Fig. 3-13. Figure 3-14 indicates a deterioration of thrust at 2600 time steps;

$\frac{3L}{2\ell} = \frac{1}{2}$ $\frac{2m}{M} = \frac{2}{576}$ $\frac{2kT}{e\varphi_o} = \frac{2}{64}$ $\frac{\varphi_1}{\varphi_o} = \frac{4}{10}$

$\eta_i = 2$ $\frac{\eta_e}{\eta_i} = 10$ $N = 80$ $\frac{2\pi}{\omega_p \Delta t} = 7.40$

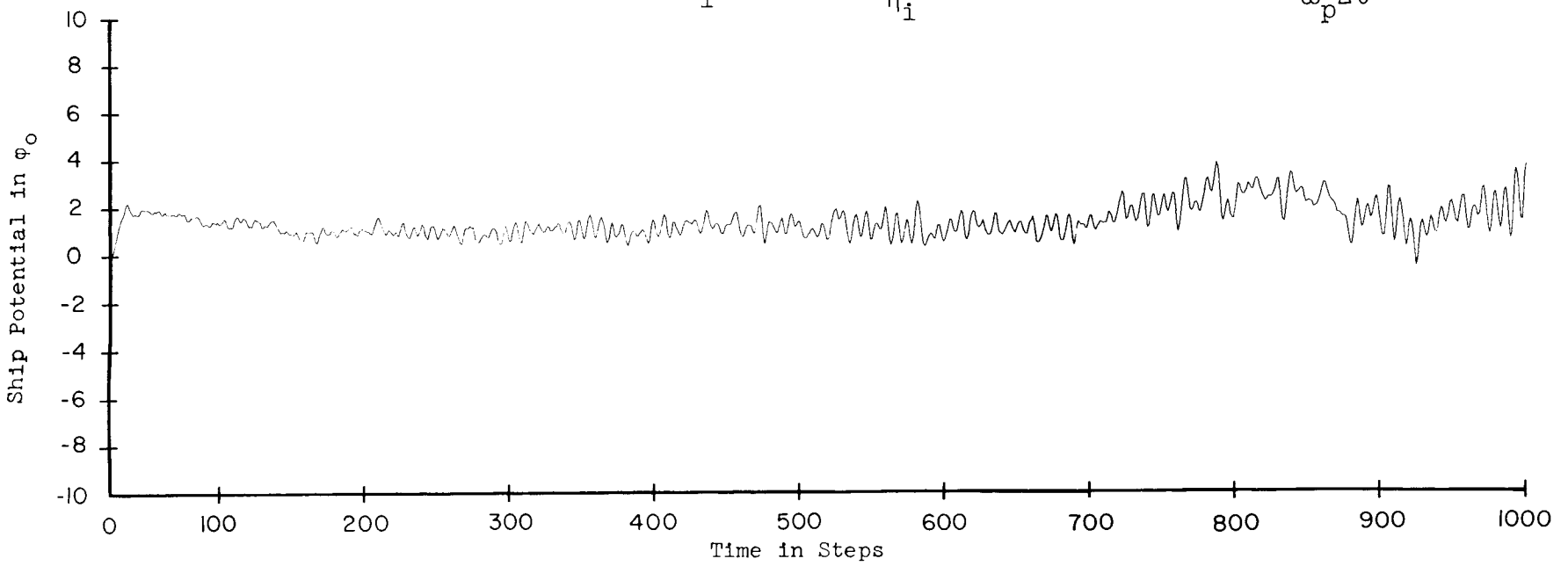

SHIP POTENTIAL VS. TIME (RUN 12BP)

Fig. 3-10

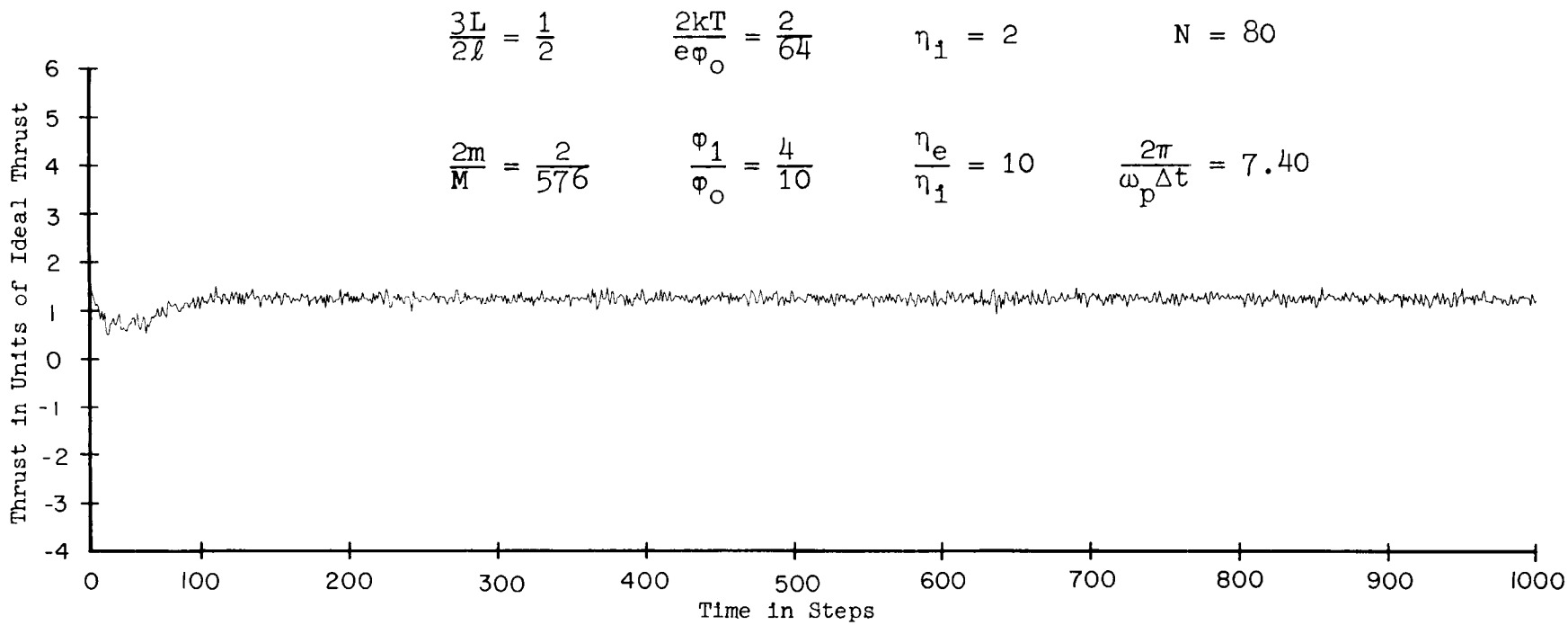

THRUST VS. TIME (RUN 12BP)

Fig. 3-11

$$\frac{3L}{2\ell} = \frac{1}{2} \qquad \frac{2kT}{e\varphi_o} = \frac{2}{180} \qquad \eta_1 = \frac{1}{2} \qquad N = 60$$

$$\frac{2m}{M} = \frac{2}{1800} \qquad \frac{\varphi_1}{\varphi_o} = \frac{4}{10} \qquad \frac{\eta_e}{\eta_1} = 2 \qquad \frac{2\pi}{\omega_p \Delta t} = 12.57$$

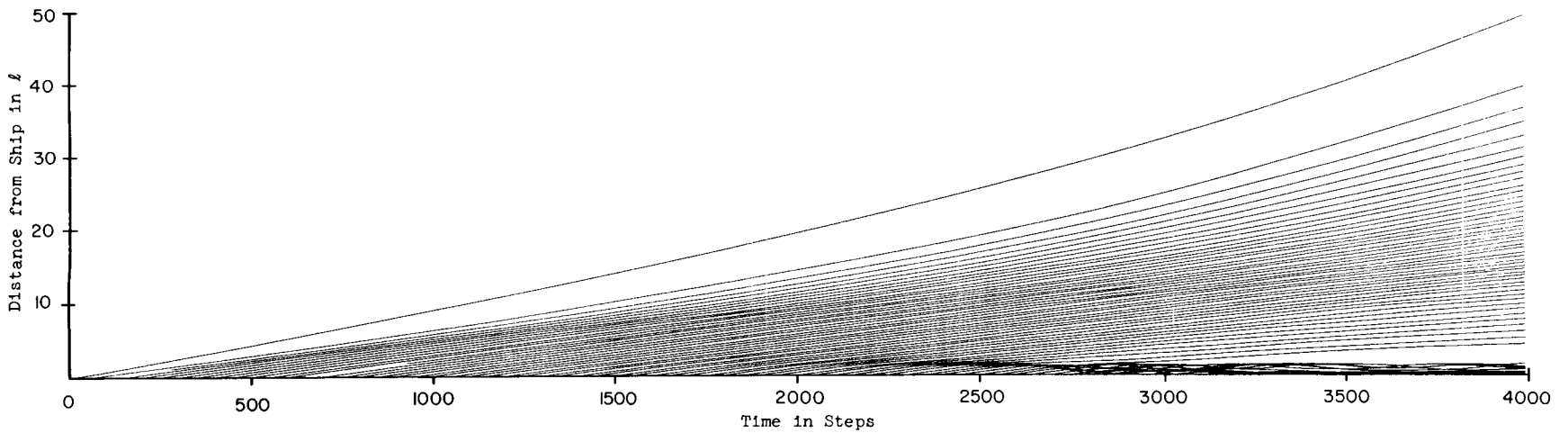

ION TRAJECTORY PLOT (RUN 12B, N = 60)

Fig. 3-12

$\frac{3L}{2\ell} = \frac{1}{2}$ $\frac{2kT}{e\varphi_o} = \frac{2}{180}$ $\eta_1 = \frac{1}{2}$ $N = 60$

$\frac{2m}{M} = \frac{2}{1800}$ $\frac{\varphi_1}{\varphi_o} = \frac{4}{10}$ $\frac{\eta_e}{\eta_1} = 2$ $\frac{2\pi}{\omega_p \Delta t} = 12.57$

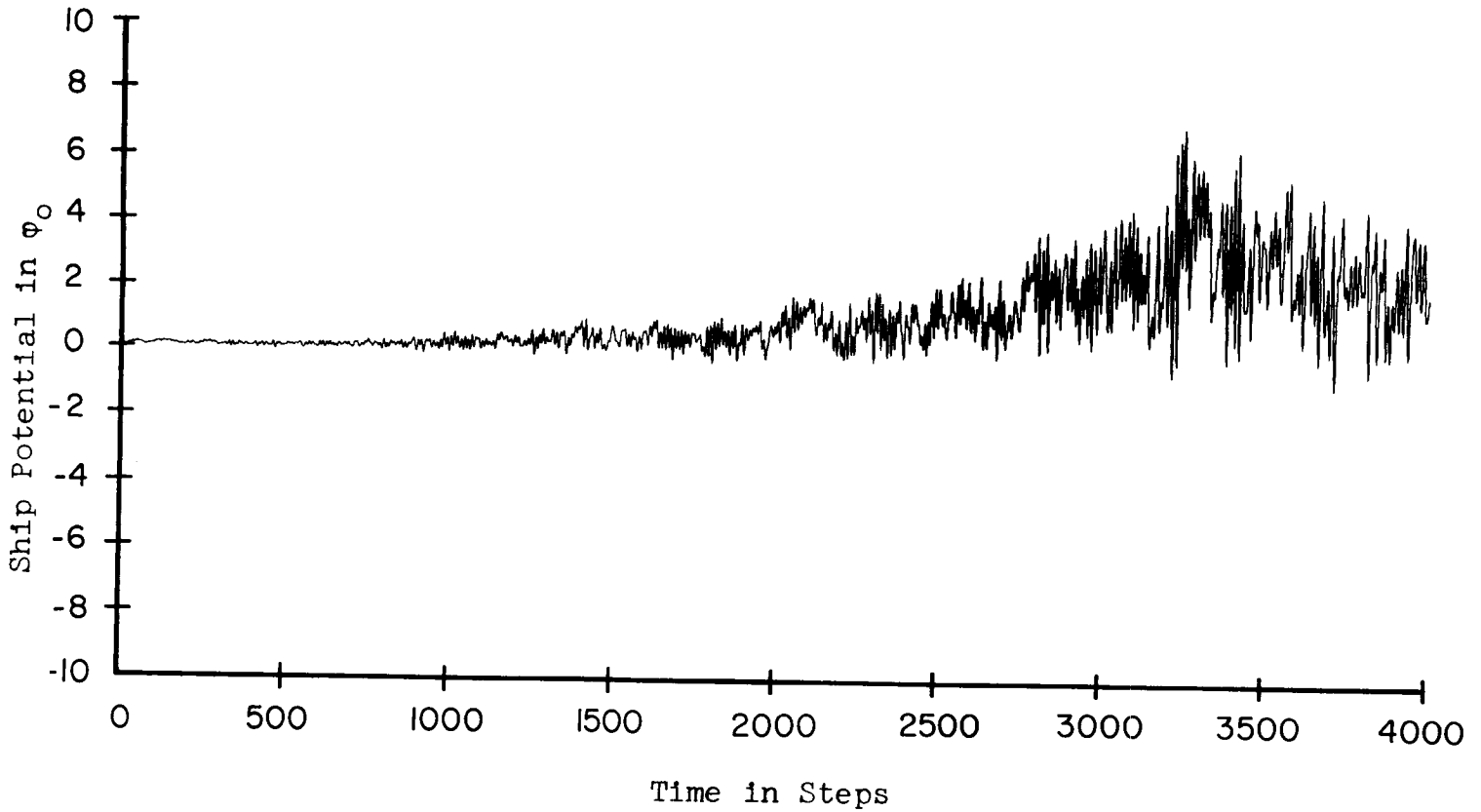

SHIP POTENTIAL VS. TIME (RUN 12B, N = 60)

Fig. 3-13

$$\frac{3L}{2\ell} = \frac{1}{2} \qquad \frac{2kT}{e\varphi_o} = \frac{2}{180} \qquad \eta_i = \frac{1}{2} \qquad N = 60$$

$$\frac{2m}{M} = \frac{2}{1800} \qquad \frac{\varphi_1}{\varphi_o} = \frac{4}{10} \qquad \frac{\eta_e}{\eta_i} = 2 \qquad \frac{2\pi}{\omega_p \Delta t} = 12.57$$

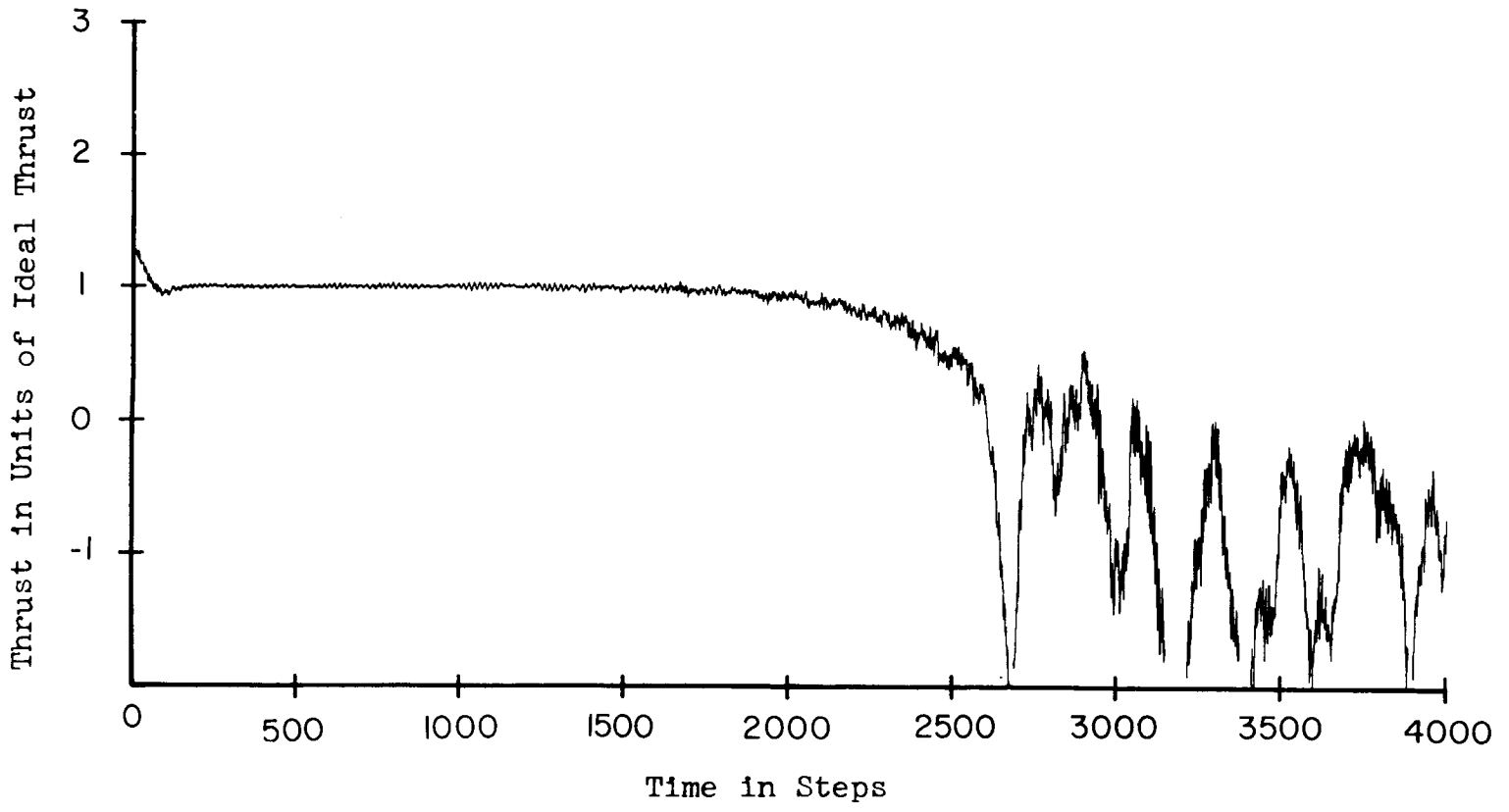

THRUST VS. TIME (RUN 12B, N = 60)

Fig. 3-14

the potential fluctuation then appears to have leveled off in subsequent time steps. However, a dc component in potential is observed. This dc potential arises in the process of thrust blow-up observed in Fig. 3-14.

The deterioration in thrust results from a deficiency of electrons in the plasma, as do all thrust blow-ups observed in the study. This electron deficiency resulted, we believe, when the rate of interception of electrons on the accelerator grid electron emitter exceeded the rate of injection of electrons.

In order to cut off electron emission so that an unrealistically high electron density did not build up around the electron emitter, an electron interception rate was programmed into the problem. For the cases plotted in this report, an interception rate of 25 percent was programmed. That is, every fourth electron to pass through the electron emitter was written off. Since the electrons, after being emitted, proceed to the front of the ion column and bounce back toward the ship, one-fourth of them are written off when they pass through the electron emitter. The rest again bounce off the potential gradient between the decel grid and the accel grid, and again pass back through the electron emitter with one-fourth again being written off. Thus, in this particular calculation, only half of the electron flux

flowing back to the ship is returned to the plasma. Since, in the transient problem being calculated, the returning flux increases with time, the returning flux eventually exceeds twice the emission flux. The plasma looses electrons faster than electrons are being received. Thus the thrust deteriorates due to lack of neutralization.

The ship potential and thrust plots for two different values of η_i are shown in Figs. 3-15 through 3-18, from which a comparison can be made. The total number of time steps in the two cases is different, so they represent the same distance traveled by the beam away from the ship. The potential fluctuations seem to be reduced for the case of smaller value of η_i, while the difference in thrust between the two cases is too small to make any general conclusion. The effect of the variation of N on the ship potential and thrust is made evident by comparing Figs. 3-19 and 3-20 with Figs. 3-17 and 3-18, respectively. For the smaller value of N, a thrust deterioration is noticed at $T/\Delta t \simeq 3500$; this is again correlated with ion bunching, as seen in Fig. 3-21. As mentioned before, this deterioration seems to be due to lack of electron emission. The effect of an increase in the electron emission on thrust is shown in Fig. 3-22; there was a significant difference in the thrust fluctuations, while the change in fluctuations of the ship

$\frac{3L}{2\ell} = \frac{1}{2}$ $\frac{2kT}{e\varphi_o} = \frac{2}{16}$ $\eta_i = 2$ $N = 40$

$\frac{2m}{M} = \frac{2}{144}$ $\frac{\varphi_1}{\varphi_o} = \frac{4}{10}$ $\frac{\eta_e}{\eta_i} = 2$ $\frac{2\pi}{\omega_p \Delta t} = 7.40$

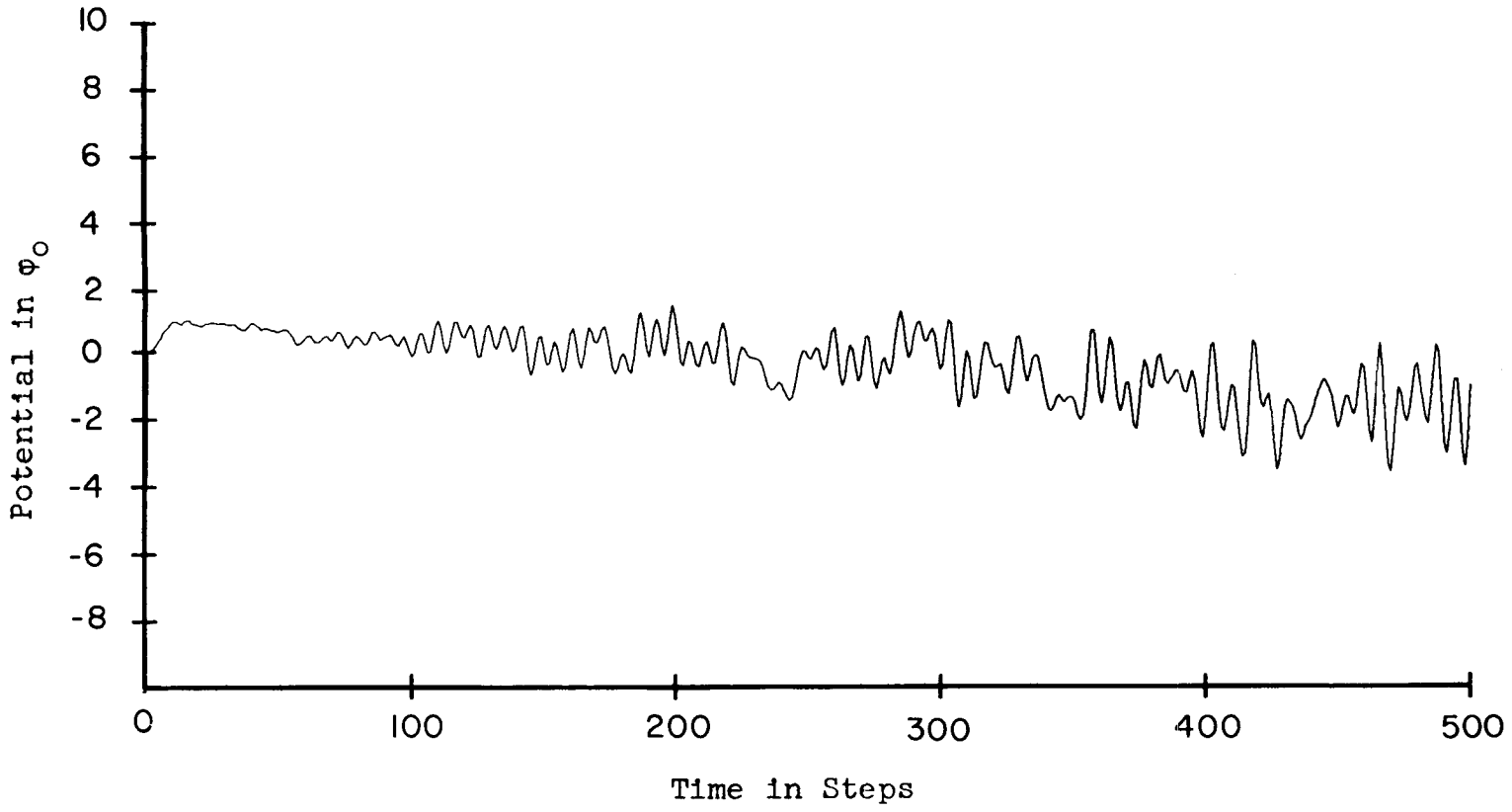

SHIP POTENTIAL VS. TIME (RUN 14D2)

Fig. 3-15

$$\frac{3L}{2\ell} = \frac{1}{2} \qquad \frac{2kT}{e\varphi_o} = \frac{2}{16} \qquad \eta_i = 2 \qquad N = 40$$

$$\frac{2m}{M} = \frac{2}{144} \qquad \frac{\varphi_1}{\varphi_o} = \frac{4}{10} \qquad \frac{\eta_e}{\eta_i} = 2 \qquad \frac{2\pi}{\omega_p \Delta t} = 7.40$$

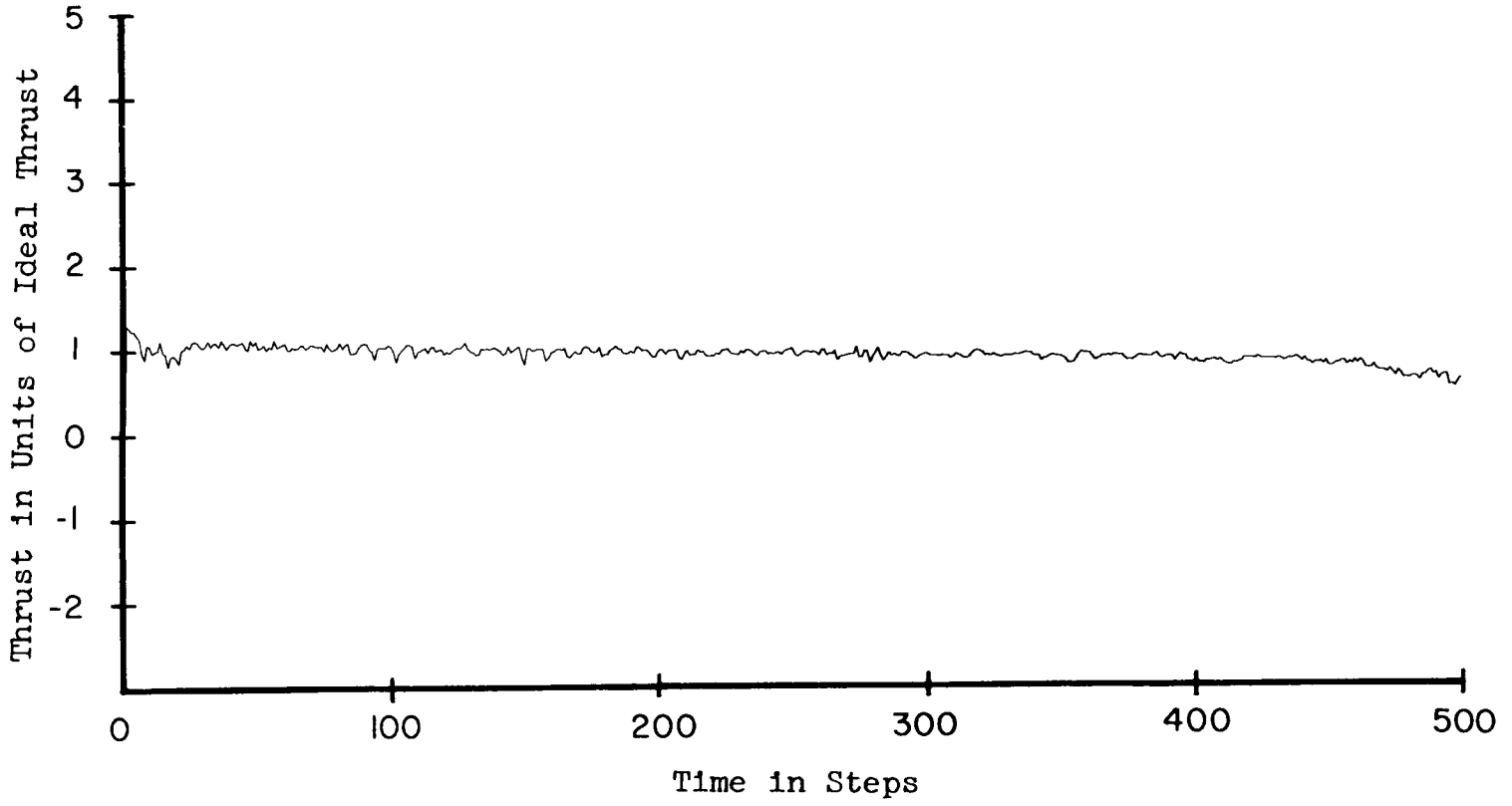

THRUST VS. TIME (RUN 14D2)

Fig. 3-16

$\frac{3L}{2\ell} = \frac{1}{2}$ $\frac{2kT}{e\varphi_o} = \frac{2}{16}$ $\eta_1 = \frac{1}{2}$ $N = 40$

$\frac{2m}{M} = \frac{2}{144}$ $\frac{\varphi_1}{\varphi_o} = \frac{4}{10}$ $\frac{\eta_e}{\eta_1} = 2$ $\frac{2\pi}{\omega_p \Delta t} = 29.6$

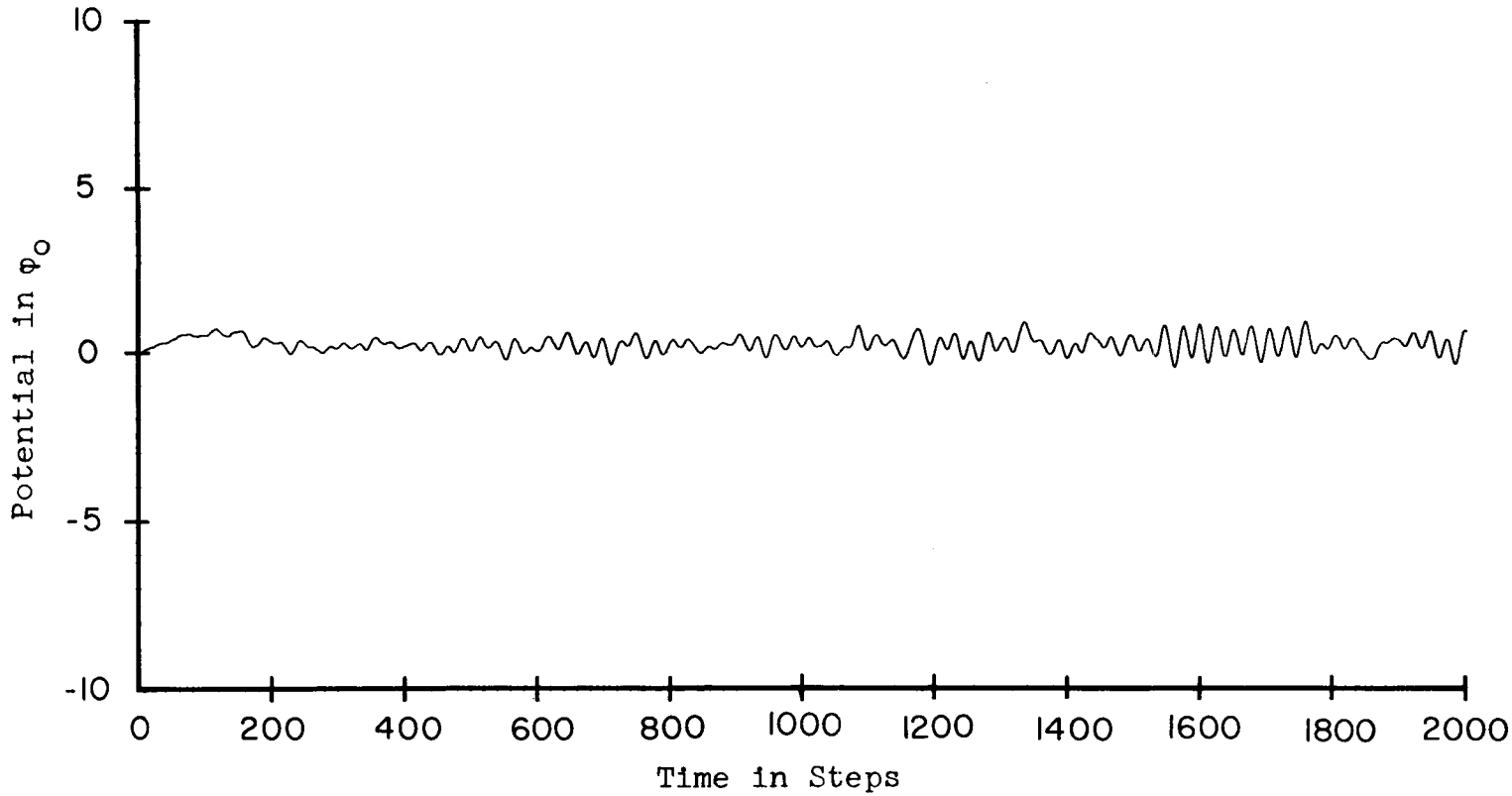

SHIP POTENTIAL VS. TIME (RUN 14F2)

Fig. 3-17

$\frac{3L}{2\ell} = \frac{1}{2}$ $\frac{2kT}{e\varphi_o} = \frac{2}{16}$ $\eta_1 = \frac{1}{2}$ $N = 40$

$\frac{2m}{M} = \frac{2}{144}$ $\frac{\varphi_1}{\varphi_o} = \frac{4}{10}$ $\frac{\eta_e}{\eta_1} = 2$ $\frac{2\pi}{\omega_p \Delta t} = 29.6$

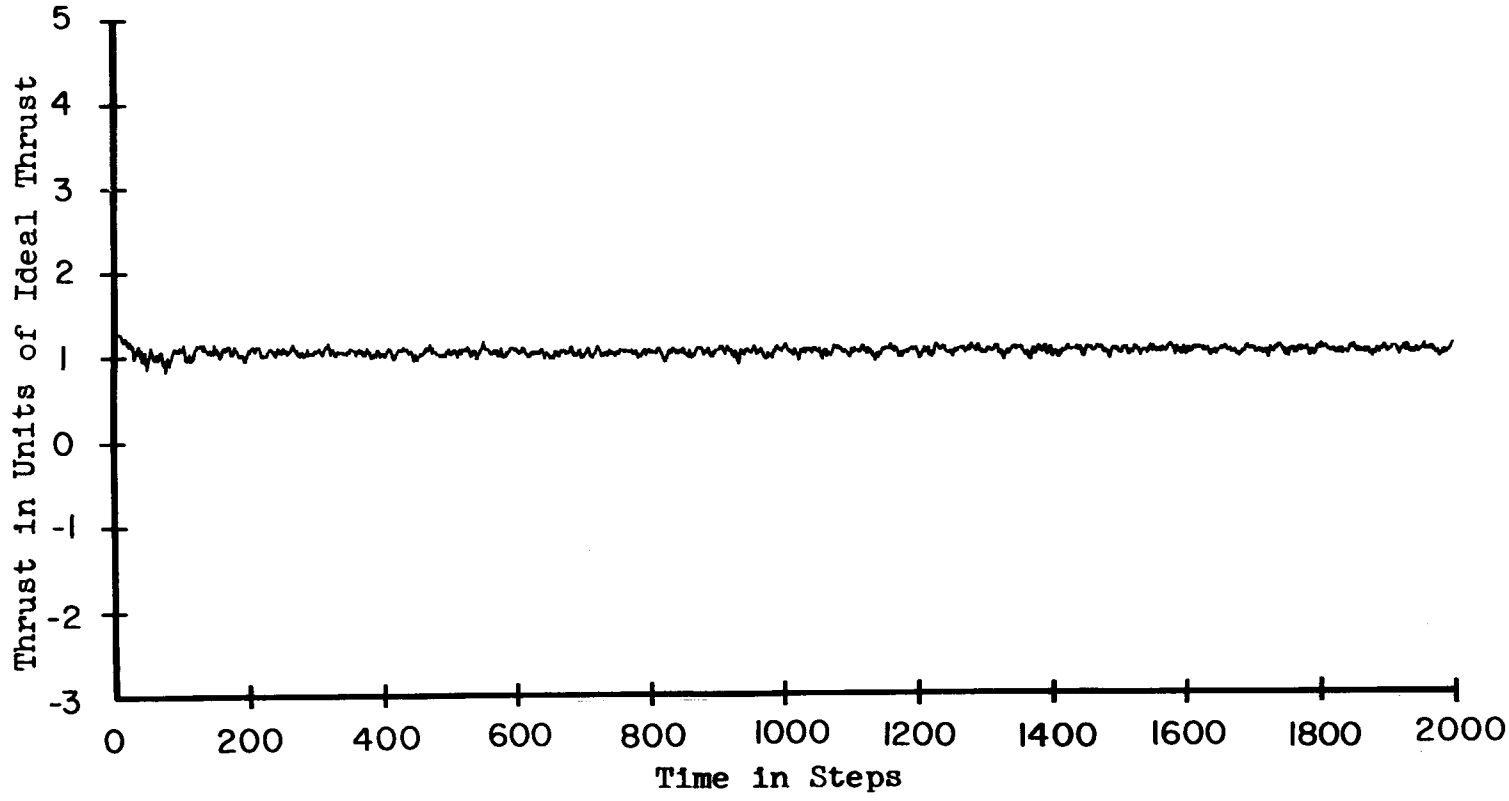

THRUST VS. TIME (RUN 14F2)

Fig. 3-18

$\frac{3L}{2\ell} = \frac{1}{2}$ $\frac{2kT}{e\varphi_o} = \frac{2}{16}$ $\eta_i = \frac{1}{2}$ $N = 24$

$\frac{2m}{M} = \frac{2}{144}$ $\frac{\varphi_1}{\varphi_o} = \frac{4}{10}$ $\frac{\eta_e}{\eta_i} = 2$ $\frac{2\pi}{\omega_p \Delta t} = 17.78$

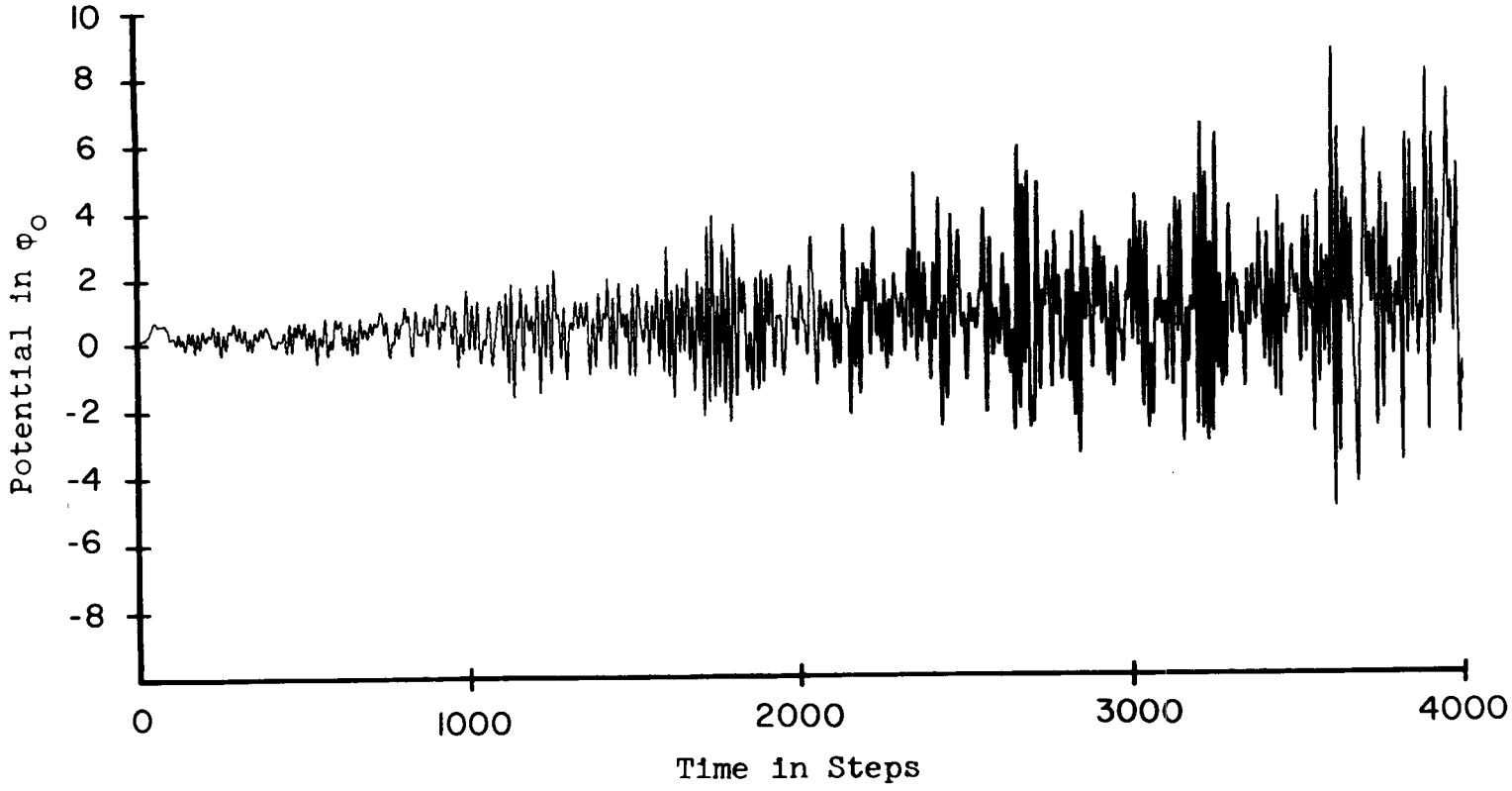

SHIP POTENTIAL VS. TIME (RUN 15F2)

Fig. 3-19

$$\frac{3L}{2\ell} = \frac{1}{2} \qquad \frac{2kT}{e\varphi_o} = \frac{2}{16} \qquad \eta_1 = \frac{1}{2} \qquad N = 24$$

$$\frac{2m}{M} = \frac{2}{144} \qquad \frac{\varphi_1}{\varphi_o} = \frac{4}{10} \qquad \frac{\eta_e}{\eta_1} = 2 \qquad \frac{2\pi}{\omega_p \Delta t} = 17.78$$

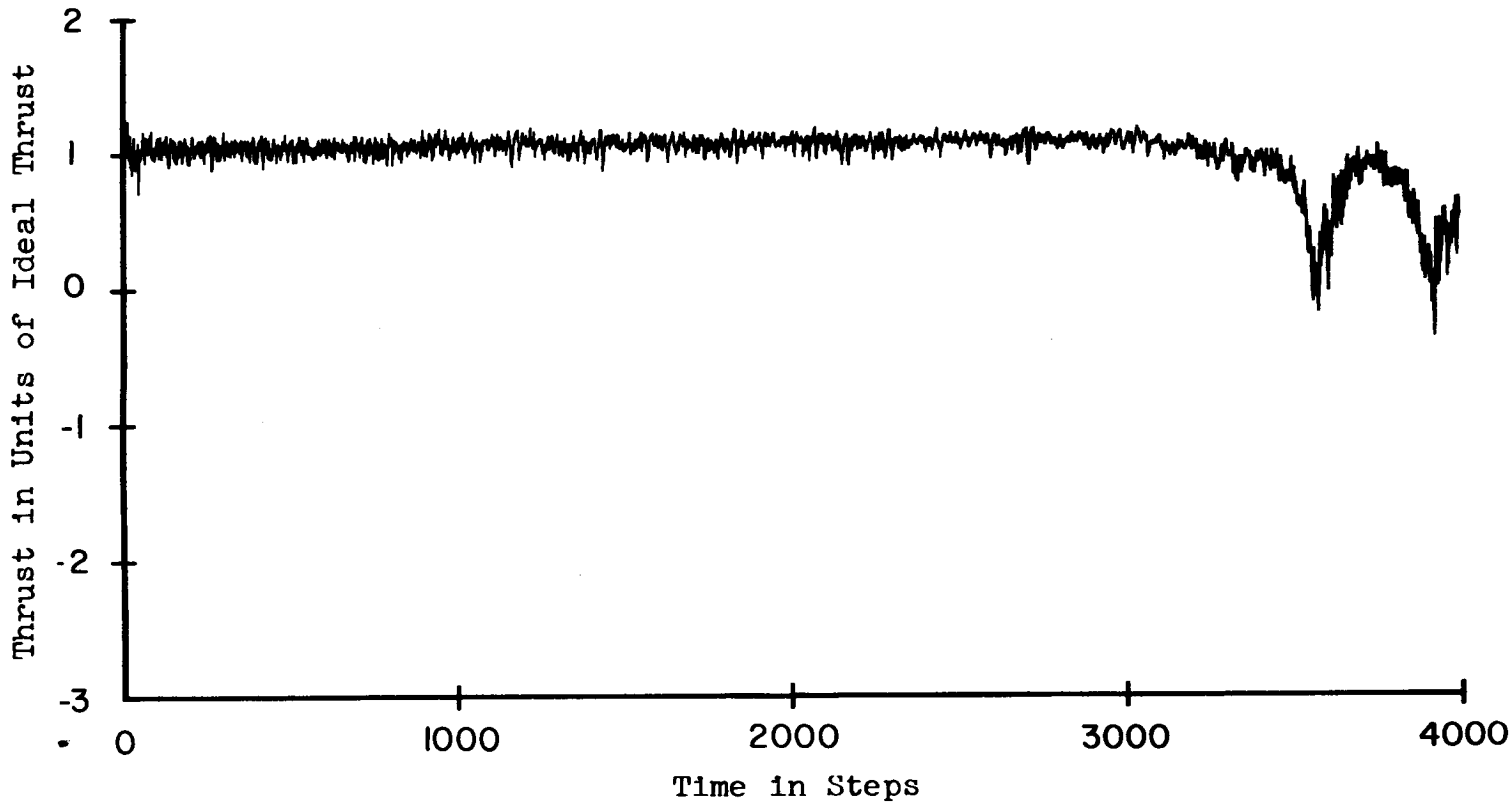

THRUST VS. TIME (RUN 15F2)

Fig. 3-20

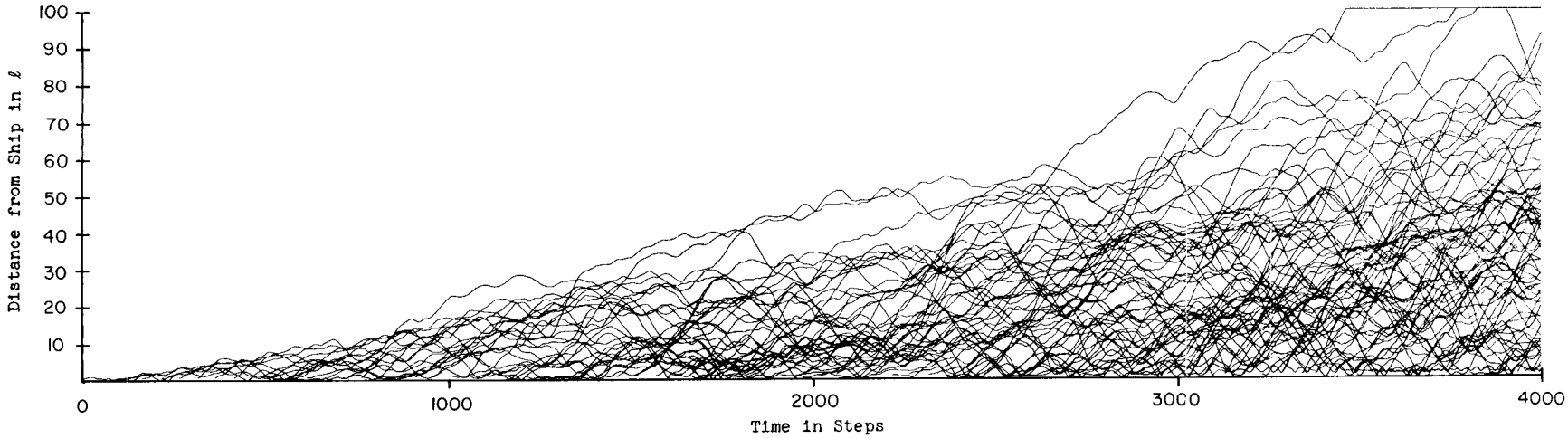

ELECTRON TRAJECTORY PLOTS (RUN 15F2)

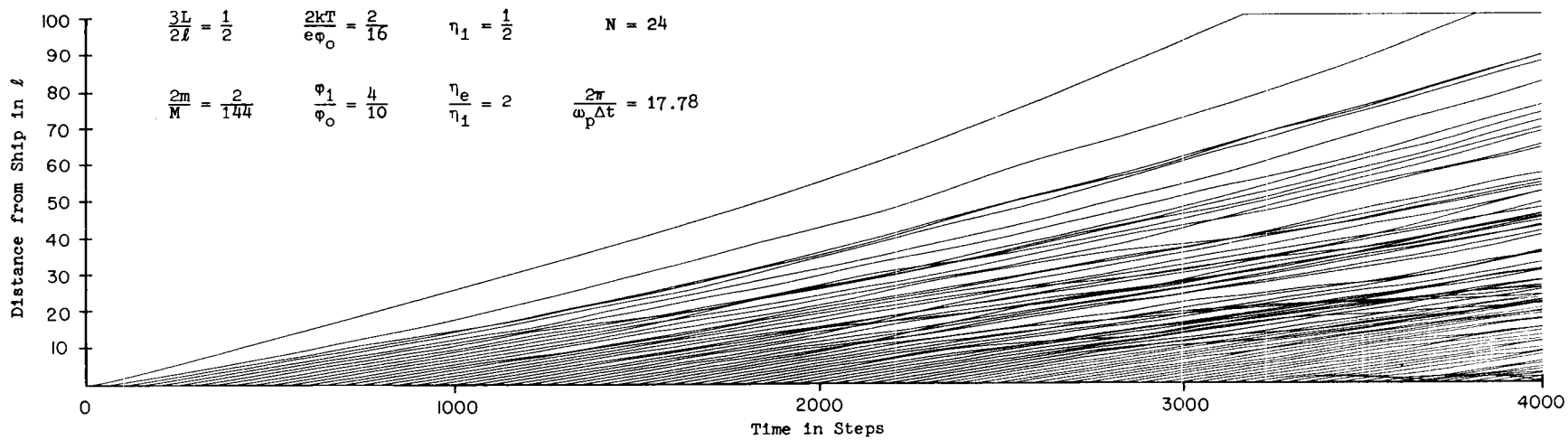

ION TRAJECTORY PLOTS (RUN 15F2)

Fig. 3-21

$\frac{3L}{2\ell} = \frac{1}{2}$ $\frac{2kT}{e\varphi_o} = \frac{2}{16}$ $\eta_i = \frac{1}{2}$ $N = 24$

$\frac{2m}{M} = \frac{2}{144}$ $\frac{\varphi_1}{\varphi_o} = \frac{4}{10}$ $\frac{\eta_e}{\eta_i} = 8$ $\frac{2\pi}{\omega_p \Delta t} = 17.78$

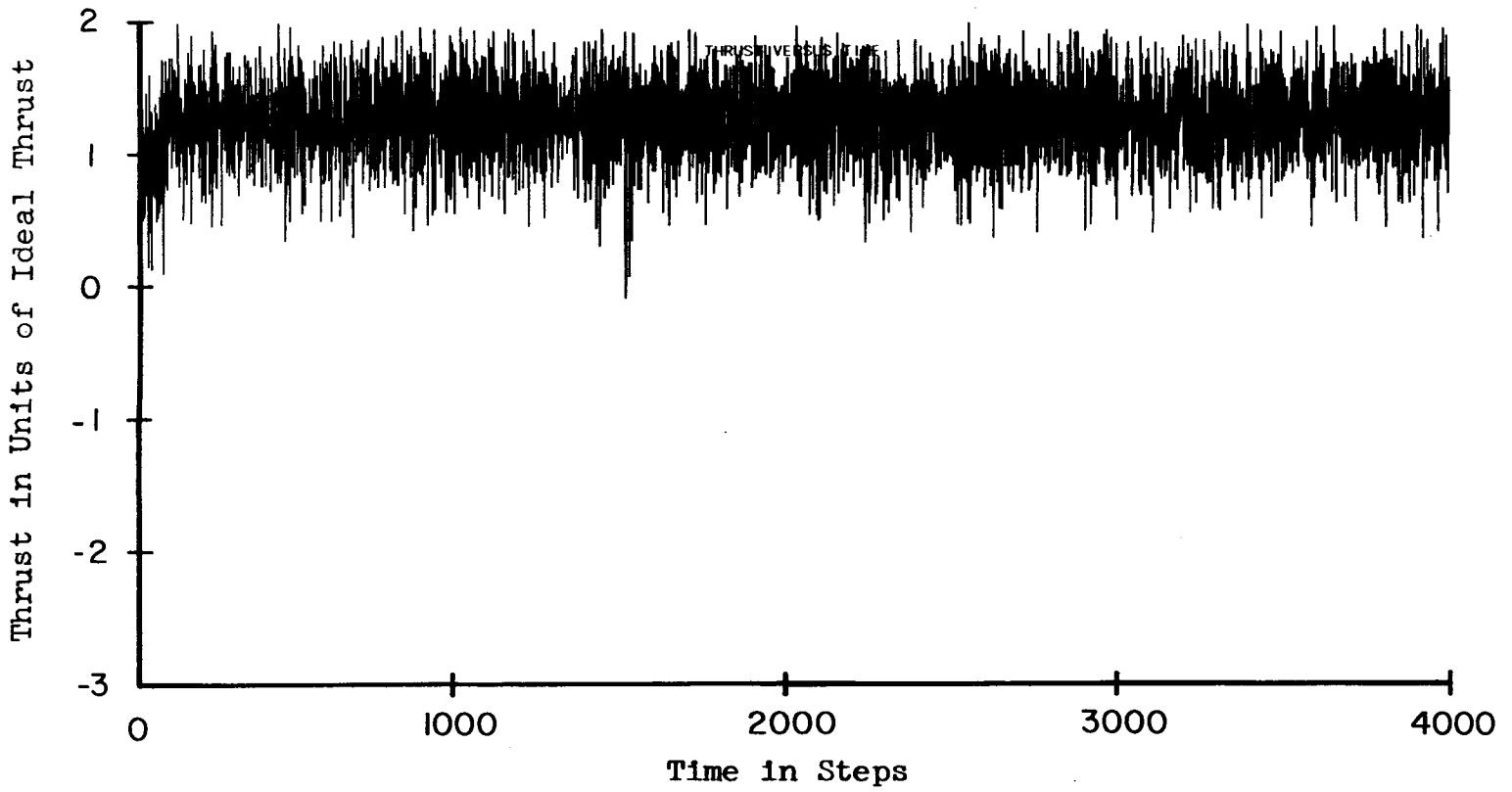

THRUST VS. TIME (RUN 15H)

Fig. 3-22

potential was insignificant. An increase in the electron emission seems to increase the fluctuations in the thrust (also noticed from the two-dimensional results given in Section V). This increase in the electron emission does not seem to improve the thrust characteristics, as compared to the case of $M/m = 576$, discussed above (compare Figs. 3-9 and 3-11). This variation is not completely understood, and sufficient data is not available to make any general conclusions.

In these calculations the transient process starts electrons from the decel grid and ions from the accel grid simultaneously. When the ions pass through the decel grid, electrons are carried along. It may be that, in the beginning, the electron flux must equal the ion flux, and, when electrons return from the outside plasma boundary, the flux being emitted from the decel grid must decrease. However, when the reduced primary flux returns from its bounce off the ion front, a deficiency of electrons occurs. This procedure is then repeated, building up an oscillation.

Thus it is concluded that this instability is due to electron deficiency. The development of instability when an electron-to-ion emission ratio of 2 is used is quite interesting and not completely understood.

An electron-to-ion emission ratio of 8 gives good thrust, but a ratio of 2 does not. Electrons which

bounce off the ion front lose energy; thus only a finite number of bounces is permitted before the electron velocity is reduced to the ion velocity in the absence of a plasma-heating mechanism.

An additional observation can be made by comparing Figs. 3-14 and 3-20. The electron deficiency instabilities seem to develop in about 200 electron plasma periods, irrespective of the difference in mass ratio.

It is intended that the plots in this report summarize the one-dimensional calculations. Additional study of the parameters is required to draw definite conclusions about the functional dependence of the output variables on the parameters of the problem.

In the previous calculations, a problem was encountered when a large electron-to-ion-emission ratio was used; the potential depression around the electron emitter grid was much larger than analytical physics had predicted. Instead of corresponding to a few kT, the potential depression around the grid was of the order of several φ_0. To eliminate this departure from the correct simulation of the problem, a change was made in the computer program.

The original electron emission process of the program consisted of giving an electron sheet a randomly selected velocity; if the initial velocity was positive, the electron was placed on the positive side of the grid;

but if the velocity were negative, the electron was placed on the negative side. However, a problem would develop if the electric field near the grid was strong enough to cause the first difference of the electron to be such that the next position of the electron would be on the other side of the grid. If this first difference were large, the electron sheet was placed at a potential difference corresponding to φ_o, instead of the few kT which normally stop and turn around electron sheets.

The program was changed so that any electron which moves back through the grid on the first step after emission is written off. Run 15H was repeated, and the results are shown in Figs. 3-23 through 3-25. This modification in the electron emission, as discussed above, does seem to improve the thrust characteristics, while the fluctuations in the ship potential are slightly increased. These results indicate that the simulation of the initially emitted electrons is very important; a similar conclusion is made from the results of the two-dimensional configuration given in Section V. The E-field may, in some cases, vary rapidly in space, but a relatively large number of time steps in each plasma period ensures more accurate results.

In summary, these calculations show good mixing. No electrons pass through the accel grid and bombard the ion emitter. The thrust is slightly greater than ideal. The reason for this is not completely understood. However, the condition seems to be correct, since the

$\frac{3L}{2\ell} = \frac{1}{2}$ $\frac{2kT}{e\varphi_o} = \frac{2}{16}$ $\eta_i = \frac{1}{2}$ $N = 24$

$\frac{2m}{M} = \frac{2}{144}$ $\frac{\varphi_1}{\varphi_o} = \frac{4}{10}$ $\frac{\eta_e}{\eta_i} = 8$ $\frac{2\pi}{\omega_p \Delta t} = 17.76$

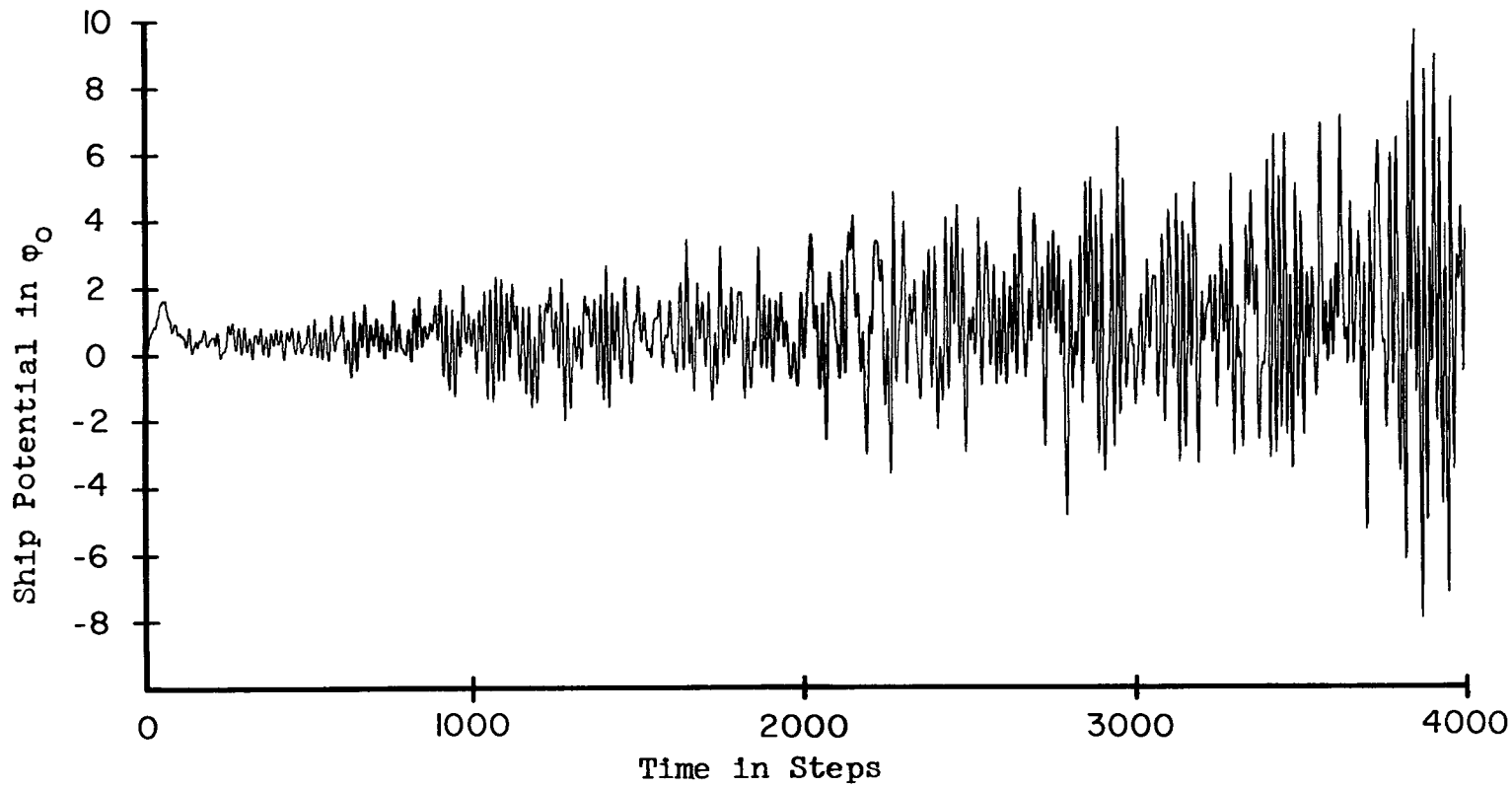

SHIP POTENTIAL VS. TIME (RUN 15HR)

Fig. 3-23

$\frac{3L}{2\ell} = \frac{1}{2}$ $\frac{2kT}{e\varphi_o} = \frac{2}{16}$ $\eta_1 = \frac{1}{2}$ $N = 24$

$\frac{2m}{M} = \frac{2}{144}$ $\frac{\varphi_1}{\varphi_o} = \frac{4}{10}$ $\frac{\eta_e}{\eta_1} = 8$ $\frac{2\pi}{\omega_p \Delta t} = 17.76$

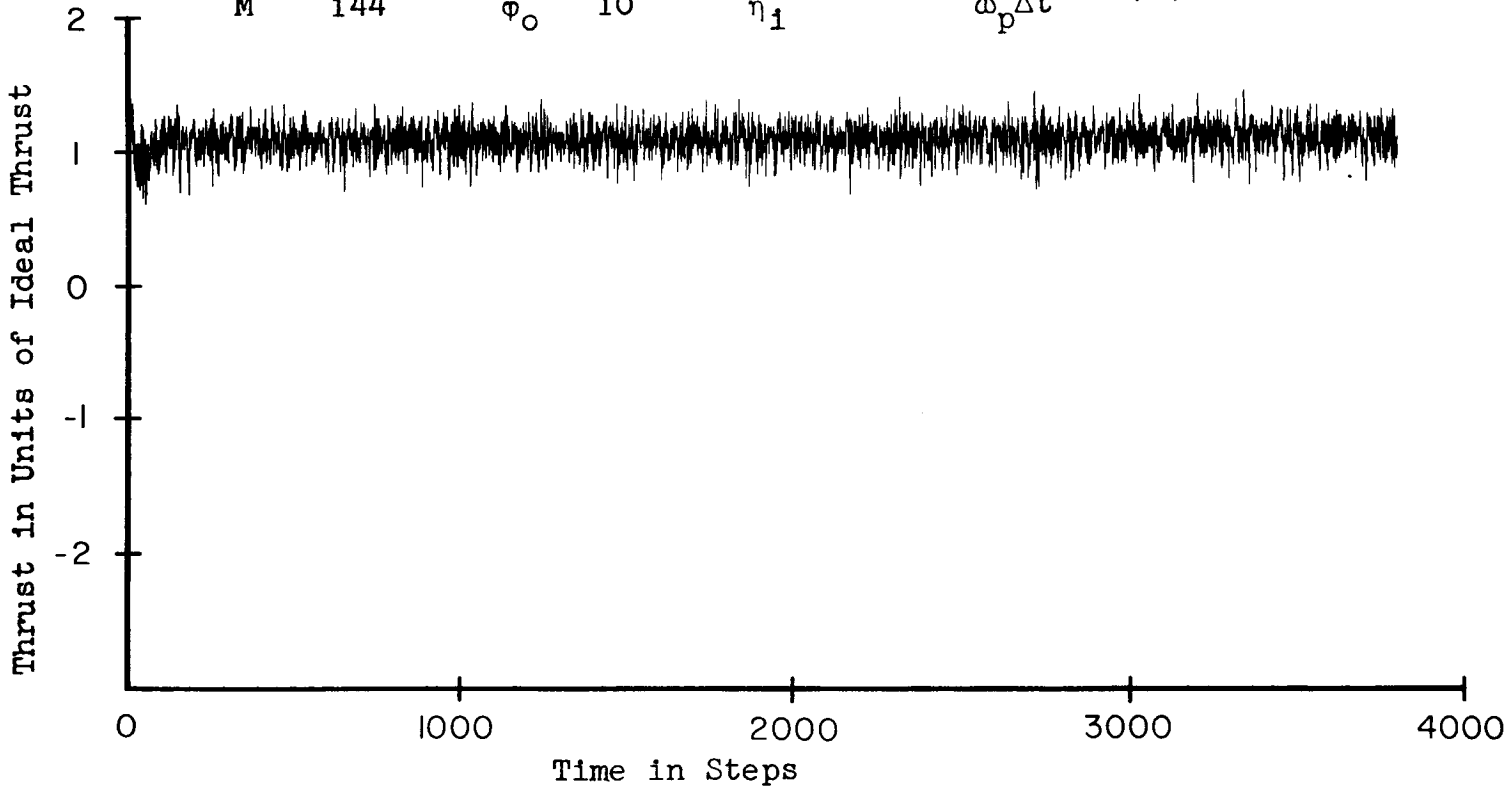

THRUST VS. TIME (RUN 15HR)

Fig. 3-24

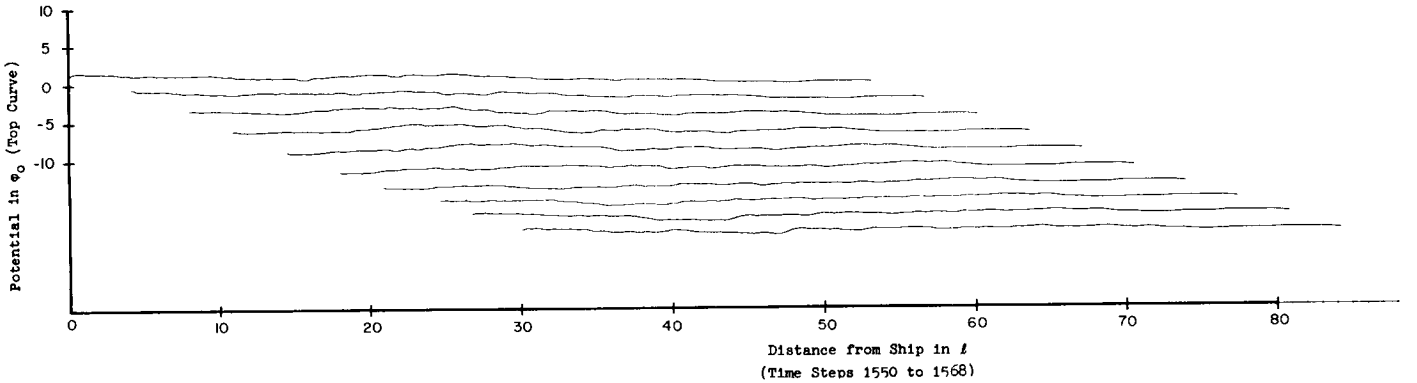

$$\frac{3L}{2\ell} = \frac{1}{2} \qquad \frac{2kT}{e\varphi_o} = \frac{2}{16} \qquad \eta_1 = \frac{1}{2} \qquad N = 24$$

$$\frac{2m}{M} = \frac{2}{144} \qquad \frac{\varphi_1}{\varphi_o} = \frac{4}{10} \qquad \frac{\eta_e}{\eta_1} = 8 \qquad \frac{2\pi}{\omega_p \Delta t} = 17.76$$

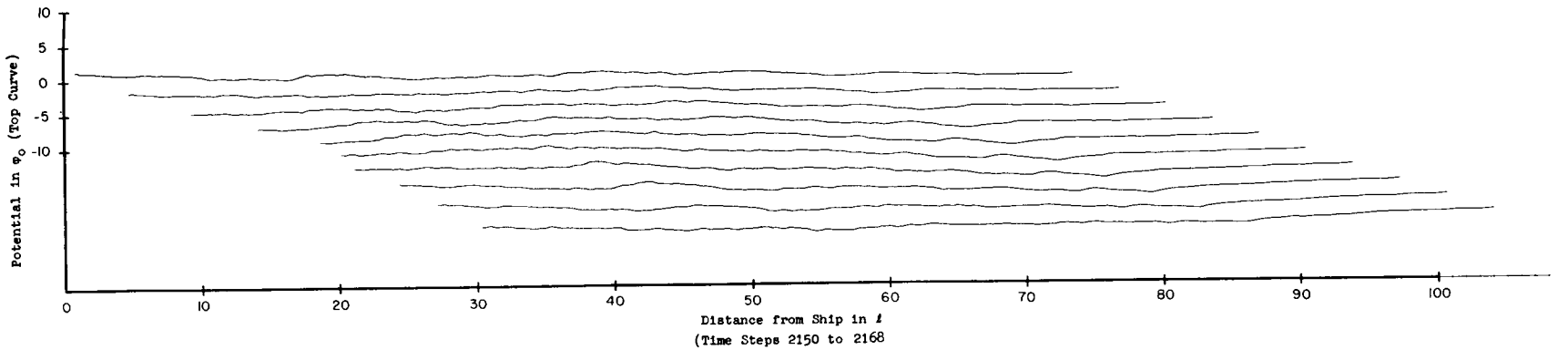

INTEGRATED POTENTIAL VS. DISTANCE (RUN 15HR)

Fig. 3-25

outer ion sheets are continually accelerating. This may be due to the force generated by the plasma pressure. The fluctuations in ship potential plotted in Fig. 3-23 continually increase in amplitude. However, great potential differences between points far apart in position are not troublesome. The integrated potential plot (Fig. 3-25) shows how the large potential difference develops.

E. Shelf Development Condition

Of interest is the comparison of the shelf developed under ideal dc conditions with that which the one-dimensional computer program predicts. The following is a derivation of the shelf conditions one would expect to develop under ideal dc conditions. The shelf formation is shown in Fig. 3-26.

Assumptions made in the analysis:

1. Distribution of electrons from emitting (decel) grid is Maxwellian.
2. Density and speed of the electrons match those of the ions.

In the shelf region, very small potential differences are able to control presence and absence of electrons; hence, from the point of view of the kilovolt scale controlling ion motion, the shelf is effectively a field-free region. We assume that

$$E = -d\varphi/dx = 0 \qquad (3\text{-}1)$$

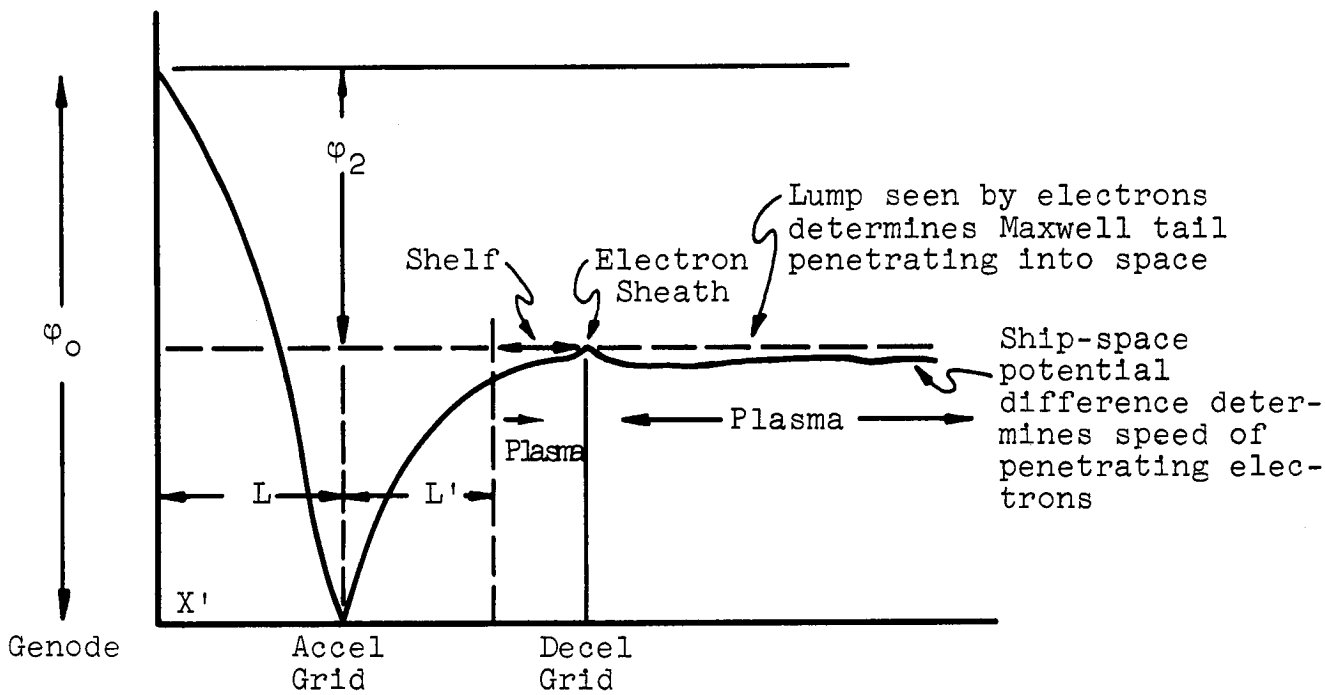

SHELF FORMATION

Fig. 3-26

at shelf. Also, in the region between genode and decel grid,

$$J = \epsilon_o \underbrace{\left[\frac{d^2\varphi}{dx'^2}\right]}_{\substack{\text{ion}\\ \text{density}}} \underbrace{\sqrt{\frac{2e\varphi}{M}}}_{\substack{\text{ion}\\ \text{velocity}}} , \qquad (3\text{-}2)$$

where x' is the distance from genode and φ is measured relative to the genode potential. From Child's law

$$J = \epsilon_o \frac{4\varphi_o}{9L^2} \left[\frac{2e\varphi_o}{M}\right]^{\frac{1}{2}} , \qquad (3\text{-}3)$$

and using the expression for ion velocity (at the accel plane) given by

$$v_o = \left[\frac{2e\varphi_o}{M}\right]^{\frac{1}{2}} , \qquad (3\text{-}4)$$

the following is obtained:

$$\frac{J}{2\epsilon_o} \frac{e}{M} = \frac{v_o^3}{(3L)^2} . \qquad (3\text{-}5)$$

Now let:

L' be distance of shelf from decel grid

x" equal running distance from shelf leftward

φ_2 equal the potential difference between genode and shelf. Then,

$$J = \epsilon_o \left[- \frac{d^2\varphi}{dx''^2} \right] \left[- \frac{2e\varphi}{M} \right]^{1/2} \qquad (3\text{-}6)$$

(This is the valid equation in the decel-shelf region, where there are assumed to be no electrons.) Equation 3-6 must be solved with the following boundary conditions:

$$\begin{aligned} \varphi &= - \varphi_o \text{ at } x'' = L \\ \varphi &= - \varphi_2 \text{ at } x'' = 0 \\ d\varphi/dx' &= 0 \text{ at } x'' = 0 \end{aligned} \qquad (3\text{-}7)$$

In the region between the decel grid and the shelf, the ion velocity v is used as the running parameter. It goes from $v = v_2$ at the shelf to $v = v_o$ at the decel grid, where

$$v = \sqrt{- \frac{2e\varphi}{M}} \ , \ v_o = \sqrt{\frac{2e\varphi_o}{M}} \text{ and } v_2 = \sqrt{\frac{2e\varphi_2}{M}} \ . \qquad (3\text{-}8)$$

Also

$$\frac{d^2\varphi}{dx'^2} = \frac{d}{dx'} \left(\frac{d\varphi}{dx'} \right) = \frac{d\varphi}{dx'} \frac{d}{d\varphi} \left(\frac{d\varphi}{dx'} \right) = \frac{d}{d\varphi} \left(\frac{1}{2} \left(\frac{d\varphi}{dx'} \right) \right) \qquad (3\text{-}9)$$

$$= \frac{d}{d\varphi} \left(\frac{E^2}{2} \right) \qquad (E = \text{field}) \ . \qquad (3\text{-}10)$$

From Eq. 3-8 we obtain

$$\frac{d^2\varphi}{dx'^2} = -\frac{2e}{M}\frac{d}{d(v^2)}\left(\frac{E^2}{2}\right) = \tag{3-11}$$

$$= -\frac{e}{Mv}\frac{d}{dv}\left(\frac{E^2}{2}\right) \quad . \tag{3-12}$$

Thus, from Eq. 3-6,

$$J = \epsilon_o \frac{e}{M}\frac{d}{dv}\left(\frac{E^2}{2}\right) \quad , \tag{3-13}$$

which, with the condition that $E = 0$ at $v = v_2$, integrates to

$$E^2 = 2\frac{M}{e}\frac{J}{\epsilon_o}(v - v_2) \quad . \tag{3-14}$$

The equation of motion is

$$\frac{dv}{dt} = v\frac{dv}{dx''} = \frac{e}{M}E \quad , \tag{3-15}$$

or

$$\frac{d}{dx''}(v^2) = \frac{zeE}{M} \quad , \tag{3-16}$$

where E is now the field reckoned in the direction of increasing x" (i.e., leftward). This is positive. Thus, from Eq. 3-14,

$$E = + \left[\frac{2M}{e} \frac{J}{\epsilon_o} (v - v_2) \right]^{\frac{1}{2}} \tag{3-17}$$

(which, incidentally, is proportional to transit time to shelf), we obtain

$$x'' = \left[\frac{M\epsilon_o}{8Je} \right]^{\frac{1}{2}} \int_{v_2}^{v} \frac{d(v^2)}{\sqrt{v - v_2}} \quad , \tag{3-18}$$

which can be integrated by change of variable, going back to E:

$$v = v_2 + \frac{e\epsilon_o}{2MJ} E^2 \quad , \tag{3-19}$$

$$dv = \frac{e\epsilon_o}{MJ} EdE \quad , \tag{3-20}$$

$$x'' = \frac{\epsilon_o}{J} \int \left(v_2 + \frac{e\epsilon_o}{2MJ} E^2 \right) dE \quad , \tag{3-21}$$

$$x'' = \frac{\epsilon_o}{J} \left(v_2 E + 1/3 \frac{e\epsilon_o}{2MJ} E^3 \right) \quad , \tag{3-22}$$

and

$$x'' = \frac{\epsilon_o}{J} \left(v_2 + 1/3 \frac{e\epsilon_o}{2MJ} E^2 \right) E \quad . \tag{3-23}$$

Substituting from Eq. 3-19, eliminating E from Eq. 3-23,

$$x'' = \frac{\epsilon_o}{J}\left[v_2 + 1/3\,(v - v_2)\right]\sqrt{\frac{2M}{e}\frac{J}{\epsilon_o}(v - v_2)} \tag{3-24}$$

$$= \frac{\epsilon_o}{3J}(v + 2v_2)\sqrt{v - v_2}\sqrt{\frac{2M}{e}\frac{J}{\epsilon_o}} \quad . \tag{3-25}$$

Letting $v = v_o$, we obtain L'.

$$L' = 1/3\sqrt{\frac{2\epsilon_o M}{eJ}}\,(v_o + 2v_2)\sqrt{v_o - v_2} \quad . \tag{3-26}$$

Multiplying through by 3 and squaring,

$$(3L')^2 = (v_0 + 2v_2)^2\,(v_o - v_2)\,\frac{2M\epsilon_o}{Je} \quad . \tag{3-27}$$

Solving for $(L'/L)^2$ in Eqs. 3-5 and 3-27,

$$\left(\frac{L'}{L}\right)^2 = \frac{(v_o + 2v_2)^2\,(v_o - v_2)}{v_o^{\,3}} = \left(1 + 2\frac{v_2}{v_o}\right)^2\left(1 - \frac{v_2}{v_o}\right) \quad . \tag{3-28}$$

Note that when $v_2 = 0$, $L' = L$, i.e., deceleration back to zero takes just the distance L.

Now, from Eq. 3-8,

$$\frac{v_2}{v_o} = \sqrt{\frac{\varphi_2}{\varphi_o}} \quad ; \tag{3-29}$$

hence

$$\frac{L'}{L} = \left(1 + 2\sqrt{\frac{\varphi_2}{\varphi_o}}\right)^2 \left(1 - \sqrt{\frac{\varphi_2}{\varphi_o}}\right) \quad . \qquad (3\text{-}30)$$

Letting

$$\frac{\varphi_2}{\varphi_o} = 0.6 \quad ,$$

we obtain

$$\frac{L'}{L} = 1.21 \quad . \qquad (3\text{-}31)$$

Hence, if ℓ is chosen greater than 1.21 L for the above case, where $\varphi_2/\varphi_o = .6$, then a shelf will develop. For the one-dimensional calculations discussed in this section, the shelf developed as predicted above.

IV. TWO-DIMENSIONAL ANALYSIS

A. Introduction

The formulation and the computational results for the one-dimensional model are presented in Sections II and III. The results have produced a fair insight into the mechanism of space-charge neutralization problem in ion engines. However, there are several limitations in the one-dimensional simulation. It does not take into account the transverse variations which may lead to beam spreading (or even beam shrinking) in the transverse direction; moreover, in the one-dimensional model the space-charge field is considered constant between any two charged sheets having a discontinuity at the location of each charged sheet. Thus, it becomes desirable to extend this analysis to a two-dimensional configuration, taking into account several practical considerations in the design of the ion beams for ion engines and the difficulties involved in solving this problem by using a high-speed digital computer.

Since the plasma electromagnetic wavelength is considerably larger than the dimensions, and as noted from the results given in Sections III and V. space-charge neutralization occurs within very small distances, retardation effects are negligible; thus, simulation and solution of a

problem involving Poisson's equation rather than the wave equation is generally correct. The Cartesian coordinate system was selected, primarily because the procedure for solving Poisson's equation developed for it and discussed in Sections IV.D and IV.E is very fast as compared to that in the other coordinate systems. The other advantage in using the Cartesian coordinate system is that the equations of motion in this system are separable.

Section IV.B describes the assumptions made in the analysis, and the description of the physical model is presented in Section IV.C. Development of Poisson's difference equation, based upon Fourier analysis[10], and evaluation of space-charge voltage are discussed in Sections IV.D and IV.E, respectively. Trajectory equations are derived in Section IV.G, and the normalization of the various parameters is discussed in Section IV.H; Sections IV.I and IV.J describe the injection conditions and evaluation of thrust.

---

10. R. Hockney and O. Buneman, "A Fast Solution of Poisson's Equations Using Fourier Analysis," paper presented at the ACM Conference, Denver; August, 1963.

B. Assumptions Made in This Analysis

The following assumptions are made in this analysis:

1. Non-relativistic mechanics are applicable.
2. The initial velocity components obey a Maxwellian distribution.
3. The effect of direct collisions between electron-electron, ion-ion, and electron-ion is neglected.
4. The electric fields remain constant within a small time interval Δt.
5. The charge enclosed in a small mesh is uniformly distributed in the mesh.
6. The system is periodic in the transverse direction with an axis of symmetry in each period.

C. Description of the Physical Model

It has been mentioned in Section IV.A that periodicity in the transverse(y) direction is assumed. This assumption is quite consistent with the experimental configurations currently being studied; moreover, this procedure requires less computer time, as a result of the grouping procedure used in this analysis (described in Quarterly Report No. 5). The periodic system in the Cartesian coordinate system is shown in Fig. 4-1. Because of periodicity, only one period is studied. A schematic drawing of a typical period is shown in Fig. 4-2. A symmetry across y=0 axis makes it convenient to study half period only, i.e., for $0 \leq y \leq b/2$, where b is length of each period in the transverse direction. The division of the half period

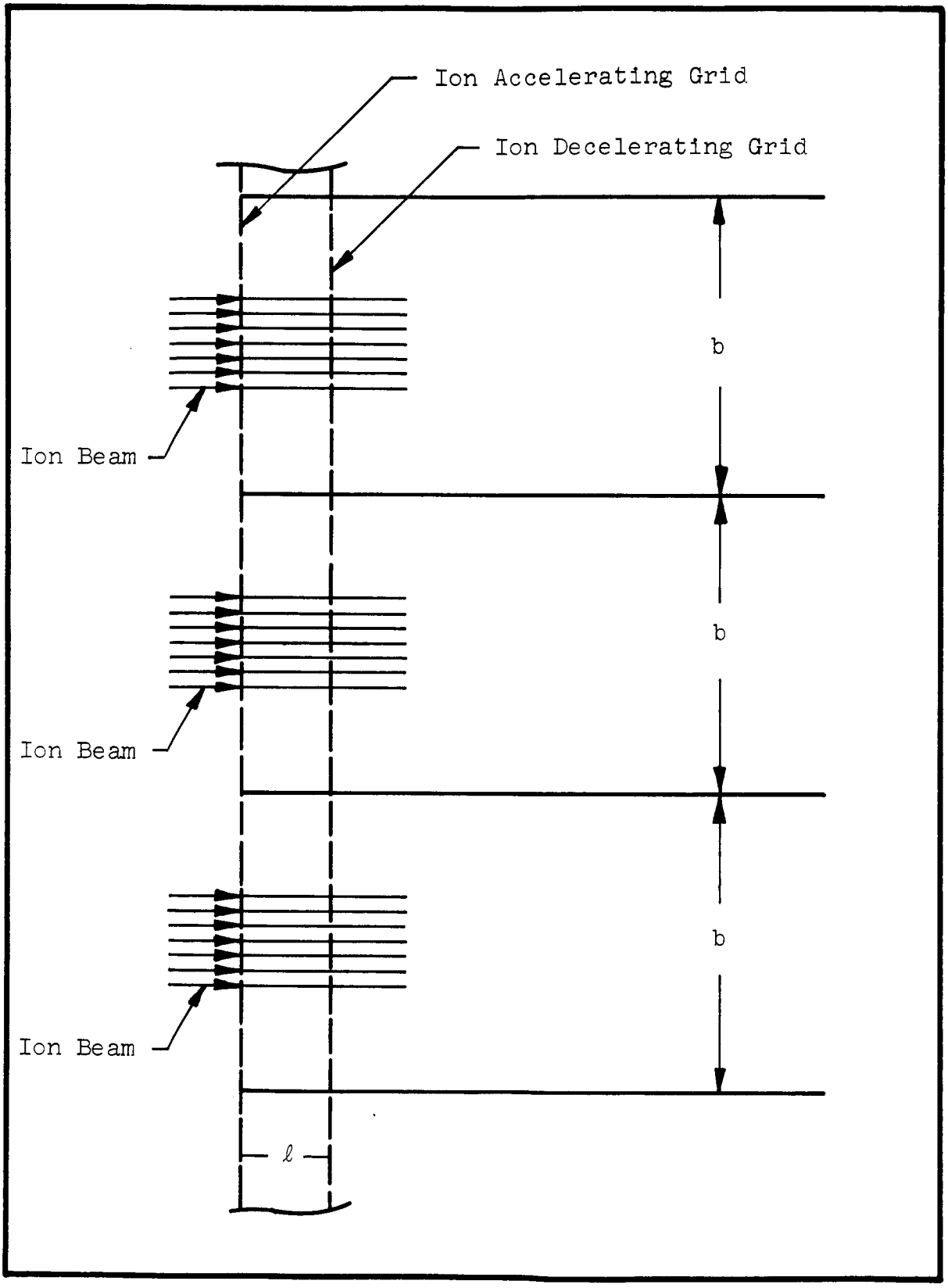

A SCHEMATIC FOR A PERIODIC IDEALIZED ION-BEAM FLOW

Fig. 4-1

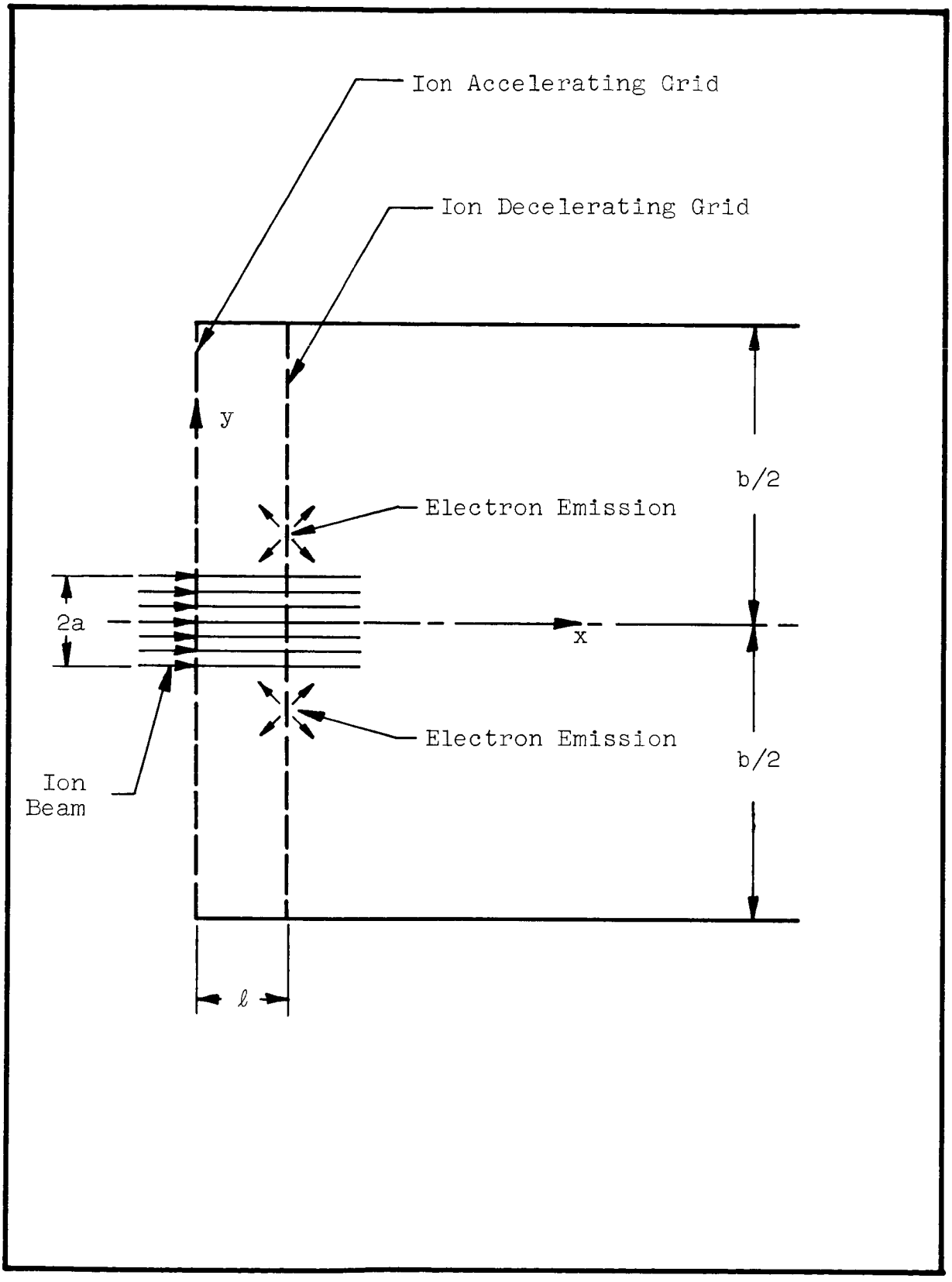

A SCHEMATIC OF AN IDEALIZED ION-BEAM FLOW IN ONE PERIOD

Fig. 4-2

under consideration, into various rectangles is illustrated in Fig. 4-3. Any electron or ion moving out of this half period has a counterpart particle which moves into this half period. The complete period is divided into 48 rectangles in the transverse direction extending infinitely along the z-axis; a different value of this number would require a different grouping system in the Fourier analysis section of the potential solver. For maximum efficiency in computer time and logic, it is always preferable to have this number equal to the least common multiplier.

With 48 rectangles in the full period (24 rectangles in the half period), a reasonably good resolution of the system has been achieved. The charge in a rectangle is assumed to be uniformly distributed in the rectangle.

The ions are injected at a constant velocity across the plane x=0 and at several points within $0 < y < a$, where a = width of the unperturbed ion beam in the half period. The plane x=0 is normally referred to as the accel grid, and ions are injected at a velocity corresponding to the accel grid potential. The plane x=8 is referred to as the decel grid. The region between the two grids is divided into 8 rectangles on the basis of resolution and computer limitations. The decel grid is at a positive voltage with respect to the accel grid; this tends to decelerate slightly the ions, and any electron moving

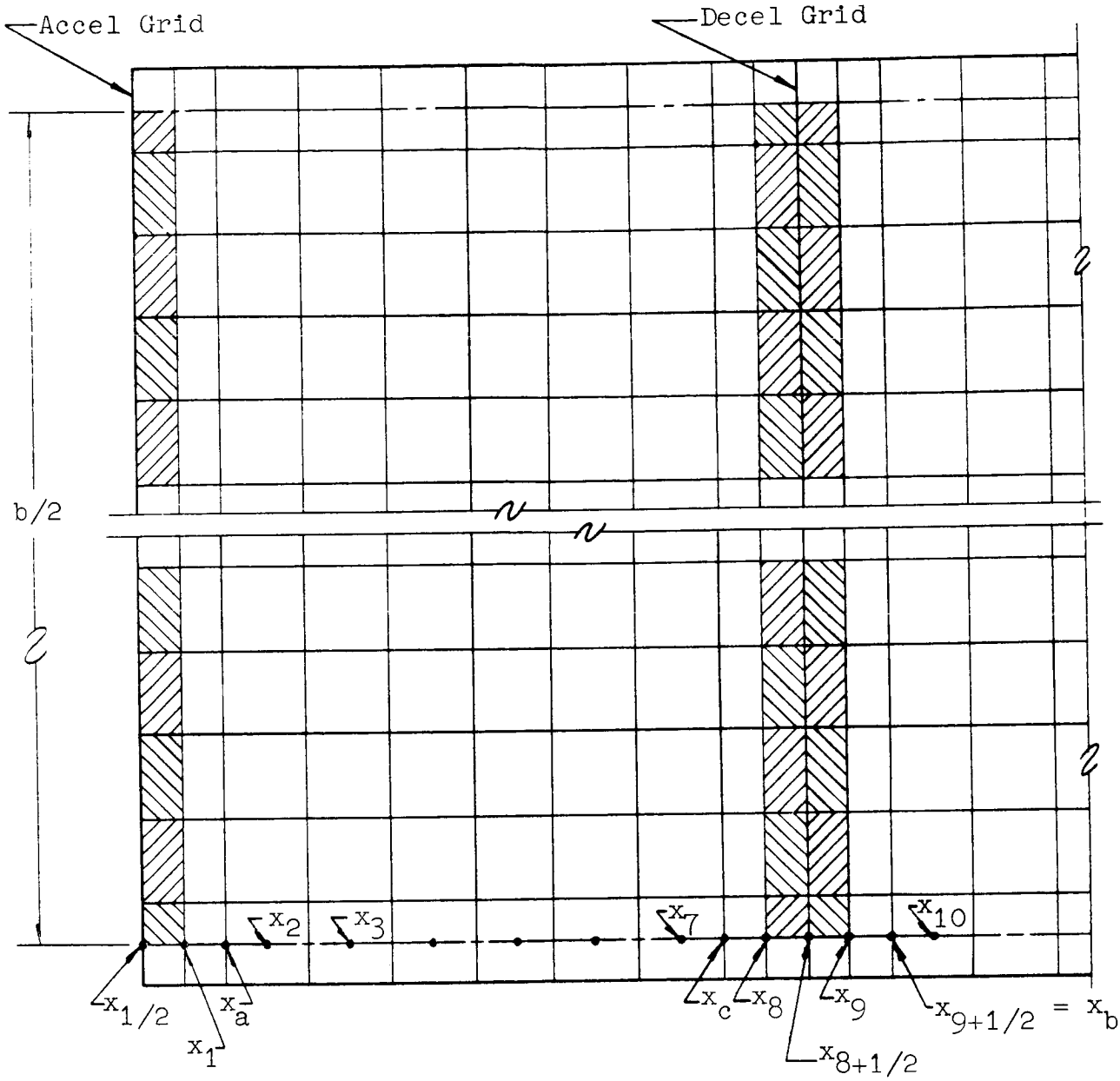

DIVISION OF THE HALF PERIOD IN THE X-Y PLANE

Fig. 4-3

into the region between the two grids is turned back. This is necessary to obtain efficient space-charge neutralization, because any electron crossing the accel grid will not come back to the region under consideration; such an electron may even affect the ion emission.

Electrons are emitted with random velocity components, according to the Maxwellian velocity distribution, from several points of the infinitesimaly thin emitting surface along the decel grid from $0 < c < d < b/2$, where c and d are the y-coordinates of the end points of the electron emitter. The electrons are emitted from both sides of the emitter. Of all electrons crossing the decel grid between $c < y < b/2$, a certain percentage are absorbed, with newly emitted electrons replacing the absorbed electrons in storage. Because of computer limitations, the space beyond the decel grid has been tracked only upto 192 rectangles (i.e. x=200). The electrons and ions reaching the plane x=200 are written off, and newly generated particles take their place in storage. This seems to be a reasonably good assumption, because the space potential observed periodically seems to remain almost constant beyond $x \simeq 100$, indicating that the beam is almost completely neutralized. This is also verified by the ion trajectory plots given in Section 5.

D. Development of Normalized Poisson's Difference Equation

Assuming periodicity for space-charge density and voltage in the transverse (y) direction, the expression for $\varphi(x,y)$, the space-charge voltage, and $\rho(x,y)$, the space-charge density, can be written correctly at the points i,j in the following manner:

$$\varphi_{i,j} = \sum_{k=0}^{K-1} U_{i,k} \cos 2\pi k \frac{y_j}{b} \quad , \qquad (4\text{-}1)$$

and

$$\rho_{i,j} = \sum_{k=0}^{K-1} \bar{\rho}_{i,k} \cos 2\pi k \frac{y_j}{b} \quad , \qquad (4\text{-}2)$$

where

$$U_{i,k} = \frac{2}{K} \sum_{y_j} \varphi_{i,j} \cos 2\pi k \frac{y_j}{b} \qquad (4\text{-}3)$$

and

$$\bar{\rho}_{i,k} = \frac{2}{K} \sum_{y_j} \rho_{i,j} \cos 2\pi k \frac{y_j}{b} \qquad (4\text{-}4)$$

for $k \neq 0$ and $k \neq 24$, where K = total number of mesh points in the transverse direction; $U_{i,k}$ and $\bar{\rho}_{i,k}$ are the Fourier transforms of $\varphi_{i,j}$ and $\rho_{i,j}$, respectively; y-direction is

Fourier-analyzed, and each Fourier harmonic is associated with the appropriate value of k; and the y_j's refer to the y-coordinates of the centroids of the various rectangles. For k=0 and k=24, the right hand sides of Eqs. 4-3 and 4-4 are divided by 2. By substituting the following identity* in Poisson's difference equation

$$\varphi_{i,j+1} + \varphi_{i,j-1} - 2\varphi_{i,j} = -\sum_k 4U_{i,k} \sin^2 \pi k \frac{\Delta y}{b} \cos 2\pi k \frac{y_j}{b} \quad , (4\text{-}5)$$

the following is obtained:

$$U_{i+1,k} + U_{i-1,k} - (2+4\lambda^2 \sin^2 \pi k \frac{\Delta y}{b}) U_{i,k}$$

$$= - \frac{2}{K} \lambda \frac{q_\ell}{\epsilon_o} \sum_{y_j} N(x_i,y_j) \cos 2\pi k \frac{y_j}{b} \quad , (4\text{-}6)$$

where

$$\lambda = \Delta x/\Delta y \quad , \qquad (4\text{-}6a)$$

$$\rho(x_i,y_j) = q_\ell \ \lambda \ N(x_i,y_j)/(\Delta x)^2 \qquad (4\text{-}6b)$$

---

* $\varphi_{i,j} = \sum_k U_{i,k} \cos 2\pi k(y_{j-1}+\Delta y)/b$

is used for deriving Eq. 4-5.

and $N(x_i, y_j)$ = total number of ions-minus-electrons in the i-jth rectangle with its centroid at (x_i, y_j) and q_ℓ is the charge per unit length. By substituting for q_ℓ/ϵ_o from Eq. 4-56 in Eq. 4-6, the following is obtained:

$$U_{i+1,k} + U_{i-1,k} - \left(2+4\lambda^2 \sin^2 \pi k \frac{\Delta y}{b}\right) U_{i,k}$$

$$= - \frac{2}{K} \frac{\lambda}{N} \left(\frac{\ell}{L}\right)^2 \frac{a}{\ell} \frac{\omega_p^2 L^2}{\eta} \sum_{y_j} N(x_i, y_j) \cos 2\pi k \frac{y_j}{b} , \quad (4\text{-}7)$$

where ℓ = accel-decel grids spacing, L = ion source-accel grid spacing, a = width of the ion beam in the transverse direction in the half period, N = total number of ions in the half period and in the spacing between the accel and decel grids when drifting at the injection velocity, ω_p = plasma frequency of electrons with N electrons in the half period and in the spacing between the accel and decel grids, and η = absolute ratio of charge to mass of an electron. By defining a new dimensionless space-charge voltage V by

$$V_{i,j} = \sum_k X_{i,k} \cos 2\pi k \frac{y_j}{b} \quad , \quad (4\text{-}8)$$

where

$$\varphi(x_i, y_j) = - \frac{8}{9} \left(\frac{\Delta x}{\ell}\right)^2 \left(\frac{\ell}{L}\right)^2 \frac{\varphi_o}{\left(\omega_p \Delta t\right)^2} V_{i,j} , \quad (4\text{-}9)$$

and Δt = time step used for updating of the charged particles, Eq. 4-7 is reduced to the following equation:

$$X_{i-1,k} + X_{i+1,k} - \left(4-2 \cos 2\pi k \frac{\Delta y}{b}\right) X_{i,k}$$

$$= q^* \sum_{y_j} N(x_i, y_j) \cos 2\pi k \frac{y_j}{b} \quad , \qquad (4\text{-}10)$$

for $k \neq 0$ and $k \neq 24$. The expression for q^*, the normalized dimensionless charge per unit length, is given by

$$q^* = \frac{\lambda}{KN} \left(\frac{\ell}{\Delta x}\right)^2 \frac{a}{\ell} (\omega_p \Delta t)^2 \qquad (4\text{-}11)$$

Derivation of Eq. 4-9 is discussed in Section IV.G and

$$\varphi_o = \frac{9}{4} \frac{\omega_p^2 L^2}{\eta} \quad , \qquad (4\text{-}12)$$

derived in Section IV.I is used in deriving Eq. 4-10. The advantage of the potential normalization given by Eq. 4-9 becomes evident from the expressions for the normalized trajectory equations derived in Section IV.G. Equation 4-10 is the normalized Poisson's difference equation. The normalized space-charge harmonic voltage for the kth harmonic is evaluated by using newly developed methods described in the following sections of this report. It may be mentioned again that for k=0 and k=24, the right hand side of Eq. 4-10 is divided by 2.

In general, the total number of space-charge harmonic potentials to be evaluated is equal to the total number of the grid points in each period. It is necessary to solve for (K/2)+1 cosine harmonics and (K/2)-1 sine harmonics. Because the condition of symmetry assumed in this case, all the sine harmonics are identically equal to zero; thus it is necessary to evaluate only (K/2)+1 cosine harmonics. Once the harmonic space charge potentials are evaluated by using Eq. 4-10, the actual space-charge voltage distribution is obtained by using Eqs. 4-8 and 4-9. It may be noticed that the evaluation of the Fourier space-charge harmonics and the use of Eq. 4-8 involve a considerable number of multiplications and additions; evaluation of cosines of several arguments, depending upon the various combinations of the values of k and y_j, is also required. The use of a systematic procedure referred to as "grouping", reduces considerably the computer time necessary for this purpose and makes this method much more attractive than others for solving voltage distribution. The summation on the right hand side of Eq. 4-10 is also made by using the grouping technique described in detail in the fifth quarterly report.

The only error in this method is due to the writing of the Poisson's differential equation in the difference form. For common problems the contributions from the

higher order derivatives are very small, and thus the solution of the Poisson's equation obtained is quite accurate. This is described in detail in Section IV.I.

An alternate method for developing Poisson's difference equation for each harmonic is substituting Eq. 4-1 directly in Poisson's differential equation. In this case it is necessary to consider an infinitely large number of Fourier harmonics, although the contributions from the higher-order harmonics are considerably reduced, and only a limited number of harmonics may be considered for most practical problems. In this case Poisson's differential equation is reduced to the following equation:

$$\frac{d^2U_{i,k}}{dx^2} - \left(\frac{2\pi k}{b}\right)^2 U_{i,k} = -\frac{4}{\pi k}\frac{\lambda q_\ell}{\epsilon_o(\Delta x)^2}\left(\sin \pi k \frac{\Delta y}{b}\right)$$

$$\sum_{y_j} N(x_i,y_j) \cos 2\pi k \frac{y_j}{b} . \qquad (4\text{-}13)$$

$$\triangleq F\ (i,k) \qquad . \qquad (4\text{-}13a)$$

Equation 4-13a may be written as a system of simultaneous linear equations:

$$\frac{dG}{dx} - \frac{2\pi k}{b} G = F(i,k) \qquad (4\text{-}14a)$$

and

$$\frac{dU}{dx} + \frac{2\pi k}{b} U = G, \qquad (4\text{-}14b)$$

where U's and G's are functions of i and k, which are omitted here for convenience. For a given value of G at one of the boundaries, G's are evaluated at the various mesh points by integrating Eq. 4-14a from one boundary to the other. U's are then evaluated at the various mesh points by integrating Eq. 4-14b from the second boundary to the first boundary. This method is described here as the "marching method" and is discussed in detail in Section IV E. It is necessary to choose the negative signs for the second term on the left hand side of Eq. 4-14a so that there is no accumulation of error; in this manner any error developed at one stage attenuates in the process of integration (marching). If Eqs. 4-14a and 4-14b are solved by using difference equations it is necessary to use a weighting factor with Δx and then by appropriate manipulation, evaluate the value of the weighting factor. It turns out that the net result is equivalent to an integration of the differential equation.

In the case that the weighting factor mentioned above is not taken into account, it can be shown that the truncation error involved is proportional to $(k\Delta x)^2/(\Delta y)^4$

which can become quite large for large values of k. In order to reduce this truncation error, it is necessary to have Δx proportional to $(\Delta y)^n$ where $n > 2$. This requirement corresponds to a considerably larger number of Δx elements for a given geometrical configuration, which greatly increases the computer time. In fact, the introduction of the weighting factor is equivalent to an appropriate reduction in the equivalent value of Δx. The accuracy of the results can be further improved by taking into account linear and higher order approximations of the function $F(k,x)$ in the process of integration from $x_i + \Delta x_i$ to x_i.

The error involved in using this alternate method is in the omission of the contributions from the higher order harmonics, while the error involved in the former method is only in writing the Poisson's differential equation in difference form; in that case the error comes from omitting the higher order derivatives. For the most common problems the error due to omission of the higher order derivatives is quite small, and for this reason, the former method is used in this analysis.

E. Evaluation of Space-Charge Voltage

In general, Poisson's difference equation may be solved by using one of the several existing methods, but unfortunately most of the methods are very time-consuming. The method for solving the two-dimensional

Poisson's difference equation, discussed in the following pages, involves considerably less computer time than other methods.

The accuracy achieved by using this method is also good. The geometrical space of interest is divided into two regions; the region between the accel and the decel grids is referred to as Region I, and the region to the right of the decel grid is referred to as Region II. The one-dimensional Poisson's difference equation given by Eq. 4-10 (for each harmonic) is solved independently in the two regions with the appropriate boundary conditions. As mentioned before, each period is divided into 48 rectangles in the transverse direction. Region I is divided into 8 rectangles along the x-axis, while Region II is divided into 192 rectangles. These numbers are rather arbitrary and can be increased or decreased, depending upon the total number of particles to be considered and the available computer memory.

The cyclic reduction method[11] is quite useful and less time-consuming in solving Eq. 4-10, particularly when the total number of mesh points is equal to 2^n-1 for $n=1, 2, 3 \ldots$, and the potentials at the two boundaries have a well defined relationship. When the total number

---

11. G. Golub and R. Hockney, Private communication.

of mesh points is not equal to 2^n-1, it is necessary to solve the reduced number of equations by any one of the other known methods. Moreover, it is almost impossible to consider appropriately the charge enclosed in the extreme-edge rectangles when cyclic reduction method is used. To do so is quite important, particularly when one of the boundaries is an emitting surface; if not done, the results can be erroneous, particularly when the charge near the emitting surface is not accounted for in an appropriate manner. For these reasons, Gauss's elimination method has been used in solving Eq. 4-10 in Region I. This method is quite flexible and the number of the mesh points in Region I can be changed arbitrarily with little change in the subroutine. The charge enclosed in the meshes near the boundaries is appropriately taken into account, and the electric fields are interpolated to update the particles enclosed in these meshes. For Region II, Eq. 4-10 is solved by a method referred to as the "marching method". This is discussed in detail in the following sections.

1. Region I

By using suffixes 1/2, 1, 2, 3, 4 .... 8 and 8+1/2, 9, 9+1/2, 10, 11 .... for the accel grid, mesh points, and decel grid, as shown in Fig. 4-3, Poisson's difference equation may be written as

$$X_{i-1,k} + X_{i+1,k} - \left(4-2 \cos 2\pi k \frac{\Delta y}{b}\right) X_{i,k}$$

$$= q^* \sum_{y_j} N(x_i, y_j) \cos 2\pi k \frac{y_j}{b} \qquad (4\text{-}15)$$

for $i = 2,3, \ldots. 7$, where $X_{i,k}$ is the kth Fourier harmonic space-charge voltage. The space-charge voltages at points designated by suffixes 1/2, 1, and 2 are related by the Taylor's series expansion as

$$X_{1/2} = X_1 - \frac{\Delta x}{2} X_1' + \frac{1}{2} \left(\frac{\Delta x}{2}\right)^2 X_1'' - \ldots. \qquad (4\text{-}16a)$$

and

$$X_2 = X_1 + \Delta x\, X_1' + \frac{1}{2} (\Delta x)^2 X_1'' + \ldots. \qquad (4\text{-}16b)$$

By combining Eqs. 4-16a and 4-16b, the following equation for X_1'' is obtained:

$$X_1'' = \frac{4}{3}\left(\frac{X_2 + 2X_{1/2} - 3X_1}{(\Delta X)^2}\right) \quad . \qquad (4\text{-}17)$$

Since the electric field is normal to the grid, there is no change in writing the second derivative with respect to y in Poisson's differential equation in difference

form. By substituting for X_1'' from Eq. 4-17 in the two-dimensional Poisson's differential equation, and then reducing it to a one-dimensional equation (as Eq. 4-10), the following is obtained:

$$2X_{1/2,k} + X_{2,k} - 1.5(3 - \cos 2\pi k \frac{\Delta y}{b}) X_{1,k}$$

$$= \frac{3}{4} q^* \sum_{y_j} N(x_1, y_j) \cos 2\pi k \frac{y_j}{b} \quad . \qquad (4\text{-}18)$$

Preceeding in a similar manner, the difference equations for the other two end half rectangles (as shown by cross hatched areas in Fig. 4-3) are given by;

$$2X_{8+1/2,k} + X_{7,k} - 1.5(3 - \cos 2\pi k \frac{\Delta y}{b}) X_{8,k}$$

$$= \frac{3}{4} q^* \sum_{y_j} N(x_8, y_j) \cos 2\pi k \frac{y_j}{b} \qquad (4\text{-}19)$$

and

$$2X_{8+1/2,k} + X_{10,k} - 1.5(3 - \cos 2\pi k \frac{\Delta y}{b}) X_{9,k}$$

$$= \frac{3}{4} q^* \sum_{y_j} N(x_9, y_j) \cos 2\pi k \frac{y_j}{b} \quad . \qquad (4\text{-}20)$$

Equation 4-20 is helpful in solving Poisson's difference equation in Region II, as discussed in the next section. Equations 4-15, 4-18 and 4-19 form a set of equations needed to solve for the $X_{i,k}$'s in Region I by Gauss's elimination method. For k=0 and k=24, it is necessary to divide the right hand sides of these equations by 2, as discussed previously. The details of Gauss's elimination method can be obtained in any standard book on numerical analysis (for example, Scarborough[12]). The execution of the computer program written for this purpose is almost as fast as that for the cyclic reduction method.

2. Region II

For space-charge voltage evaluation in Region II, Eq. 4-10 is factorized to give the following two equations:

$$\psi_{i+1/2,k} - \beta\psi_{i-1/2,k} = q^* \sum_{y_j} N(x_i, y_j) \cos 2\pi k \frac{y_j}{b} \qquad (4\text{-}21)$$

and

$$X_{i+1,k} = \frac{X_{i,k}}{\beta} + \psi_{i+1/2,k} \quad , \qquad (4\text{-}22)$$

where β is the larger root of the algebraic equation given by

---

12. Scarborough, J.B., Numerical Mathematical Analysis, The Johns Hopkins Press, Baltimore; 1955.

$$\beta^2 - 2(2 - \cos 2\pi k \frac{\Delta y}{b})\, \beta + 1 = 0 \quad ; \qquad (4\text{-}23)$$

i.e.,

$$\beta = 2 - \cos 2\pi k \frac{\Delta y}{b} + \sqrt{(2 - \cos 2\pi k \frac{\Delta y}{b})^2 - 1} \; . \qquad (4\text{-}24)$$

Equation 4-21 is solved by starting at the maximum value of i (farthest position of the charged particle from the decel grid) and marching towards the decel grid. Equation 4-22 is solved by starting at the decel grid and marching towards the maximum value of i; the values of $\psi_{i+1/2}$'s evaluated from Eq. 4-21 are used in solving Eq. 4-22. This explains why the larger value of the root of Eq. 4-23 is used in Eqs. 4-21 and 4-22; in this way any error introduced at any stage is attenuated depending upon the value of β (which in turn depends upon the value of k). If the smaller root is used, any error introduced at one stage will grow depending upon the value of β. This can cause a considerable accumulation of error, leading to erroneous results. Equation 4-21 can be rewritten in the following form:

$$\psi_{i-1/2,k} = \frac{\psi_{i+1/2,k} - q^* \sum_{y_j} N(x_i, y_j) \cos 2\pi k \frac{y_j}{b}}{\beta} \; . \qquad (4\text{-}25)$$

For $k=0$, $\beta=1$, and for $k > 0$, $\beta > 1$: k in this case is always ≤ 24. For larger distances from the decel grid, i.e., for $x \longrightarrow \infty$ there is no charge and $N(x_i, y_j)=0$; this assumes that either the beam is completely neutralized at sufficiently large distances away from the decel grid under steady-state conditions, or there is no charge beyond i_{max} under transient-state conditions. Furthermore, for $x \longrightarrow \infty$ there are no transverse variations in the space-charge voltage, and thus $X_{i,k}=0$ for $k > 0$; for $k=0$, $X_{i+1} = X_i$ (the gradient of the potential = 0), and thus $\psi_{i+1/2,k}=0$ for all values of k and $x \longrightarrow \infty$. The advantage of factorization of Eq. 4-10 into Eqs. 4-21 and 4-22 is now evident, because the space conditions are easily simulated in the model considered here. This means that the boundary condition at $x \longrightarrow \infty$ has been simulated indirectly at the position of the charged particle farthest from the decel grid; of course, the two field components need not be zero at this location. In this method ψ's are evaluated at the boundaries of the meshes, while X's are evaluated at the centers of the meshes. In the former case one marches towards the decel grid, and in the latter case one marches away from the decel grid; hence, the name "marching method" is used for this method. In order to account properly for the contributions of the charge enclosed in the end half rectangles on the right hand

side of the decel grid (shown in Fig. 4-3), Eq. 4-20 is also used in evaluating space-charge voltage distribution in Region II. For this purpose, it is assumed that the decel grid is at zero potential. Actually, potential at $x \to \infty$ is equal to zero, which shifts the origin; this is discussed in Section IV.E.4. Combining Eqs. 4-20 and 4-25 with the condition $X_{i+1/2} = 0$,

$$X_{9,k} = \frac{-\frac{3}{4} q^* \sum_{y_i} N(x_9, y_j) \cos 2\pi k \frac{y_j}{b} + \psi_{9+1/2,k}}{1.5 \left(3 - \cos 2\pi k \frac{\Delta y}{b}\right) - \frac{1}{\beta}} \quad . \quad (4\text{-}26)$$

After $X_{9,k}$ is evaluated, the potentials $X_{i,k}$ for $i>9$ are evaluated by using Eq. 4-22.

3. Inclusion of the DC Terms in Field Computations

It has been mentioned before that there is a dc voltage across the two grids, and its presence is mainly to avoid any crossing of electrons towards the ion source. It becomes necessary to take into account the contributions from the dc field also in the updating of the particle positions from one time step to the next time step. If this is accounted for separately, it is necessary to test the region of location of each particle and then add the appropriate contribution. The logic and computer time involved are then increased. It has been found convenient to take into account the dc potential as an equivalent

charge in the Poisson's difference equation for the zeroth harmonic. Since the decel grid is assumed to be at zero potential, the potential at the accel grid is then equal to $-\varphi_d$. Using Eq. 4-9, the potential $X_{1/2}$ at the accel grid is given by

$$X_{1/2} = \frac{1}{2}\left(\frac{\ell}{\Delta x}\right)^2 \left(\frac{3L}{2\ell}\right)^2 (\omega_p \Delta t)^2 \frac{\varphi_d}{\varphi_o} \quad . \qquad (4\text{-}27)$$

By substituting for $X_{1/2}$ from Eq. 4-27 into Eq. 4-18 for k=0, and dividing the right hand side of Eq. 4-18 by 2, the following is obtained:

$$-3X_{1,0} + X_{2,0} = \frac{3}{8} q^* \sum_{y_j} N(x_1, y_j) - (\omega_p \Delta t)^2 \left(\frac{\ell}{\Delta x}\right)^2 \left(\frac{3L}{2\ell}\right)^2 \frac{\varphi_d}{\varphi_o} \ , \qquad (4\text{-}28)$$

where $\varphi_d/\varphi_o > 0$. In this manner the complete voltage distribution (from dc and space-charge effects) is evaluated in Region I; there is no contribution from dc voltage in Region II.

The consideration of the decel grid at a zero potential shifts the origin of the potential distribution, but this does not effect the particle trajectories. This makes the potential at $X \longrightarrow \infty$ equal to $X_{i_{max}}$, which varies with time depending upon the space-charge distribution. Thus in the actual case the decel grid is at a floating potential equal to $-X_{i_{max,t}}$ when referred to potential at infinity; for perfect space-charge

neutralization $X_{i_{max,o}}$ should be equal to zero.

4. Evaluation of Ship Potential

In evaluating the potential distribution, described in Section IV.E. the decel grid is assumed to be at zero potential. While the electrons and ions are traced only up to x=200 plane, it is assumed that the beam beyond x=200 is completely neutralized. This means that the potential distribution is a function of the charge distribution only in the region under consideration. The zeroth harmonic voltage beyond x=200 (x-coordinate value of the farthest charged particle away from the decel grid under initial observation) does not change while the higher order harmonic voltages attenuate depending upon the value of the harmonic. This means that the potential at $x \longrightarrow \infty$ is equal to the value of the zeroth harmonic voltage at x=200 (or the x-coordinate value of the farthest charged particle away from the decel grid under initial observation), referred to here as $X_{i_{max,o}}$. Since the potential at infinity is equal to zero, the potential at the decel grid is equal to $-X_{i_{max,o}}$.

F. Interpolation of Fields Near the Grids

The solution of Poisson's difference equation, as discussed in the above sections, gives the voltage

distribution at the centroids of the various meshes. The expressions for the electric fields acting upon the various charged particles located in the various rectangles are derived in Section IV.G. However, for the charged particles located in rectangles close to the accel and decel grids, it is necessary to interpolate potentials at points located along planes $x=x_a$, $x=x_b$, $x=x_c$ shown in Fig. 4-3. From these potentials, the general formulas for evaluation of fields discussed in the next section can be used, except that in this case the mesh size is reduced by a factor of 2. The voltages $V_{a,j}$ may be written in a Taylor's series form as

$$V_{a,j} = V_{2,j} - \frac{V_{3,j} - V_{1,j}}{2\Delta x}\frac{\Delta x}{2} + \frac{V_{3,j}+V_{1,j}-2V_{2,j}}{(\Delta x)^2}\frac{1}{2}\left(\frac{\Delta x}{2}\right)^2 - \cdots \tag{4-29}$$

$$\simeq \frac{3}{8}V_{1,j} + \frac{3}{4}V_{2,j} - \frac{1}{8}V_{3,j} \quad , \tag{4-29a}$$

where the higher-order derivatives are neglected in writing Eq. 4-29a from Eq. 4-29. Similarly, the expressions for $V_{b,j}$ and $V_{c,j}$ are given by

$$V_{b,j} = \frac{3}{8}V_{9,j} + \frac{3}{4}V_{10,j} - \frac{1}{8}V_{11,j} \tag{4-30}$$

and

$$V_{c,j} = -\frac{1}{8} V_{6,j} + \frac{3}{4} V_{7,j} + \frac{3}{8} V_{8,j} \quad . \tag{4-31}$$

Thus, the fields evaluated for the charged particles enclosed in rectangles close to the two grids are computed more accurately; this is important, because there can be considerable space-charge in the vicinity of these grids, particularly near the decel grid.

G. Trajectory Equations

The equations of motion of an electron are given by

$$\ddot{x} = - \eta E_{xT} = \eta \frac{\partial \varphi(x,y)}{\partial x} \tag{4-32}$$

and

$$\ddot{y} = - \eta E_{yT} = \eta \frac{\partial \varphi(x,y)}{\partial y} \quad , \tag{4-33}$$

and the equations of motion of an ion are given by

$$\ddot{x} = - \eta \frac{m}{M} \frac{\partial \varphi(x,y)}{\partial x} \tag{4-34}$$

and

$$\ddot{y} = - \eta \frac{m}{M} \frac{\partial \varphi(x,y)}{\partial y} \quad , \tag{4-35}$$

where η = absolute ratio of electron charge to its mass and m/M = ratio of electron mass to ion mass.

Equation 4-32 may be written in the difference form given by

$$\frac{x_{n+1}}{\Delta x} - 2\,\frac{x_n}{\Delta x} + \frac{x_{n-1}}{\Delta x} = \left(\frac{2\partial V(x,y)}{\partial x/\Delta x} \right)_n , \tag{4-36}$$

where Eqs. 4-9 and 4-12 are used in deriving Eq. 4-36 and suffixes n-1, n, and n+1 correspond to various time intervals. Similarly, the other trajectory equation is written as

$$\frac{y_{n+1}}{\Delta y} - 2\,\frac{y_n}{\Delta y} + \frac{y_{n-1}}{\Delta y} = \left(\frac{2\ \partial V(x,y)}{\partial y/\Delta y} \right)_n . \tag{4-37}$$

The corresponding equations for ions are given by

$$\frac{x_{n+1}}{\Delta x} - 2\,\frac{x_n}{\Delta x} + \frac{x_{n-1}}{\Delta x} = -\,\frac{m}{M} \left(\frac{2\ \partial V(x,y)}{\partial x/\Delta x} \right)_n \tag{4-38}$$

and

$$\frac{y_{n+1}}{\Delta y} - 2\,\frac{y_n}{\Delta y} + \frac{y_{n-1}}{\Delta y} = -\,\frac{m}{M} \left(\frac{2\ \partial V(x,y)}{\partial y/\Delta y} \right)_n \tag{4-39}$$

$$= \Delta\left(\frac{y_n}{\Delta y}\right) - \Delta\left(\frac{y_{n-1}}{\Delta y}\right) , \tag{4-40}$$

where $\Delta(y_n/\Delta y) = (y_{n+1} - y_n)/\Delta y$. The expressions for the electric fields at (x,y), may be written down from the Taylor's series expansion in the neighborhood of (x_i,y_i) and are given by

$$\left(\frac{\partial V}{\partial x/\Delta x}\right)_{x,y} = \left(\frac{\partial V}{\partial x/\Delta x}\right)_{i,j} + \left(\frac{x}{\Delta x} - \frac{x_i}{\Delta x}\right)\left(\frac{\partial^2 V}{\partial(x/\Delta x)^2}\right)_{i,j}$$

$$+\left(\frac{y}{\Delta y} - \frac{y_j}{\Delta y}\right)\left(\frac{\partial^2 V}{\partial x/\Delta x \;\; \partial y/\Delta y}\right)_{i,j} \qquad (4\text{-}41)$$

and

$$\left(\frac{\partial V}{\partial y/\Delta y}\right)_{x,y} = \left(\frac{\partial V}{\partial y/\Delta y}\right)_{i,j} + \left(\frac{y}{\Delta y} - \frac{y_j}{\Delta y}\right)\left(\frac{\partial^2 V}{\partial(x/\Delta x)^2}\right)_{i,j}$$

$$+\left(\frac{x}{\Delta x} - \frac{x_i}{\Delta x}\right)\left(\frac{\partial^2 V}{\partial x/\Delta x \;\; \partial y/\Delta y}\right)_{i,j} , \qquad (4\text{-}42)$$

where $x_i - \frac{1}{2} < x < x_i + \frac{1}{2}$ and $y_j - \frac{1}{2} < y < y_j + \frac{1}{2}$. The first and second order derivatives of potential are evaluated at the point (x_i,y_j), the centroid of the rectangle. These derivatives may be written as

$$\left(\frac{\partial V}{\partial x/\Delta x} \right)_{i,j} = \frac{V_{i+1,j} - V_{i-1,j}}{2} \quad , \tag{4-43}$$

$$\left(\frac{\partial V}{\partial y/\Delta y} \right)_{i,j} = \frac{V_{i,j+1} - V_{i,j-1}}{2} \quad , \tag{4-44}$$

$$\left(\frac{\partial^2 V}{\partial (x/\Delta x)^2} \right)_{i,j} = V_{i-1,j} - 2V_{i,j} + V_{i+1,j} \quad , \tag{4-45}$$

$$\left(\frac{\partial^2 V}{\partial (y/\Delta y)^2} \right)_{i,j} = V_{i,j-1} - 2V_{i,j} + V_{i,j+1} \quad , \tag{4-46}$$

and

$$\left(\frac{\partial^2 V}{\partial x/\Delta x \; \partial y/\Delta y} \right)_{i,j} = \frac{V_{i+1,j+1} - V_{i+1,j-1} - V_{i-1,j+1} + V_{i-1,j-1}}{4} \quad . \tag{4-47}$$

For the present problem (as noticed from the results of the one-dimensional analysis and the results given in Section V and VI), the total number of electrons is larger than the total number of ions; this illustrates the advantage of defining the normalized voltage V(x,y), as given by Eq. 4-9. (The total number of electrons is larger than the total number of ions because, in general, more electrons are needed for appropriate space-charge neutralization, the excessive electrons are absorbed by the electron emitter.) This involves minimum number of computations and, hence, minimum

computer time. The electric fields used for updating of the charged particles are evaluated by using Eqs. 4-41 through 4-47; thus the results given in the next section are quite accurate.

H. Normalization of the Various Parameters and Injection Conditions

The trajectory equations derived in the above section are normalized so as to yield accurate results within minimum computer time. In order to evaluate V, it is necessary to determine the value of $\omega_p \Delta t$ and derive some equations which have been used in obtaining the various normalized equations in the previous sections. It has been mentioned before that ions cross the accel grid at a constant velocity and with an energy equivalent to $e\varphi_o$ electron volts. Assuming the validity of Child's law in the region between the ion source and the accel grid (space-charge-limited conditions), the relation between the current density J and potential φ_o is given by

$$\varphi_o^{3/4} = \frac{3}{2} \left(\frac{J}{\epsilon_o}\right)^{1/2} \left(\frac{M}{2e}\right)^{1/4} L \quad . \tag{4-48}$$

The space-charge density ρ_o of the ion beam is given by

$$\rho_o = \frac{J}{u_o} = \frac{J}{\sqrt{2\eta\varphi_o}} \left(\frac{M}{m}\right)^{1/2} , \tag{4-49}$$

where u_o = ion exit velocity at the accel grid. Eliminating J from Eqs. 4-48 and 4-49,

$$\rho_o = \frac{4}{9} \epsilon_o \frac{\varphi_o}{L^2} \quad . \tag{4-50}$$

The electron plasma frequency is defined as

$$\omega_p^2 \overset{\Delta}{=} \eta \frac{\rho_o}{\epsilon_o} \tag{4-51}$$

$$= \frac{4}{9} \eta \frac{\varphi_o}{L^2} \quad .$$

The parameter N_i, the number of ions emitted across the decel grid per unit time is given by

$$N_i = \frac{J \, a\omega_p \Delta t}{\omega_p \, q_\ell} \quad , \tag{4-52}$$

where a = ion beam width (in the upper half period when N_i is taken as the number of ions emitted per unit-time interval in the upper half period also). In order to simulate the total ion beam, ions are emitted at several points (0.2 Δx apart) located in the range $o<y<a$ along $x=0$ axis; this insures that the ion beam will be well represented by the sample of ion trajectories. The

parameter N, the total number of ions within the region between the two grids, if drifted at the injected velocity u_o, is given by

$$N = \frac{\ell}{u_o} \frac{\omega_p}{\omega_p \Delta t} N_1 \tag{4-53}$$

By combining Eqs. 4-52 and 4-53 the following is obtained:

$$\frac{N}{N_1} = \left(\frac{M}{2m}\right)^{1/2} \frac{1}{\omega_p \Delta t} \frac{2\ell}{3L} \quad , \tag{4-54}$$

where Eq. 4-12 is used in deriving Eq. 4-54. In an actual case, the ions experience a decelerating force in the region $o<x/\ell<1$. The total number of ions in this region is greater than N; however, N/N_1 is a useful parameter in making a rough estimate for the total number of particles to be considered for a given value of N, this depends upon the values of $\omega_p \Delta t$ and the maximum number of time steps to be used in the problem. Furthermore, the space-charge density ρ_o derived in Eq. 4-50 can be written as

$$\rho_o = \frac{Nq_\ell}{\ell a} \tag{4-55}$$

or

$$\frac{q_\ell}{\epsilon_o} = \frac{\rho_o \ \ell a}{N\epsilon_o} = \frac{1}{N} \left(\frac{\ell}{L}\right)^2 \frac{a}{\ell} \frac{\omega_p{}^2 L^2}{\eta} \quad , \tag{4-56}$$

where Eq. 4-51 is used in deriving Eq. 4-56. This equation was used in deriving Eq. 4-7.

I. Injection Conditions

It has been mentioned in Section IV.C. that ions are injected across the plane x=0 at a velocity corresponding to the accel grid potential. Thus, the x-component ion-injection velocity is given by

$$\dot{x}_{i,o} = \sqrt{2\eta \ \varphi_o} \sqrt{\frac{m}{M}} \quad , \tag{4-57}$$

where φ_o = potential difference between ion source and the accel grid. The y-component of velocity of the injected ions is assumed to be zero. The electrons are emitted with random emission velocities corresponding to the Maxwellian velocity distribution. The number and emission time of the electrons emitted per unit time are kept constant during a specific computer run. The normalized electron velocity distribution with velocities $\dot{x}_i$ and $\dot{y}_i$ ($\dot{x}<\dot{x}_i<\dot{x}+d\dot{x}$, $\dot{y}<\dot{y}_i<\dot{y}+d\dot{y}$) is given by

$$f(v) = \frac{m}{kT} \sqrt{\frac{m}{2\pi kT}}\ \dot{x}\ e^{-\frac{m\dot{x}^2}{2kT}}\ e^{-\frac{m\dot{y}^2}{2kT}}\ d\dot{x}\ d\dot{y}\ , \qquad (4\text{-}58)$$

where the x- and y-velocity components correspond to the geometrical configuration used in this analysis, i.e., x- and y-components, normal and parallel to the two grids, respectively.

The distribution function f(v) may be separated to give the x- and y-components distribution functions as

$$f(\dot{x}) = \frac{m}{kT}\ \dot{x}\ e^{-\frac{m\dot{x}^2}{2kT}}\ d\dot{x} \qquad (4\text{-}59)$$

and

$$f(\dot{y}) = \sqrt{\frac{m}{2\pi kT}}\ e^{-\frac{m\dot{y}^2}{2kT}}\ d\dot{y} \quad . \qquad (4\text{-}60)$$

Equations 4-59 and 4-60 may be solved to give the two random velocity components by the following two equations:

$$\dot{x} = \sqrt{\frac{2kT}{m}}\ (-\ \ell n\ R)^{1/2} \qquad (4\text{-}61)$$

and

$$\dot{y} = \pm \sqrt{\frac{2kT}{m}}\ \text{Inverse}\ \left\{\text{erf}(G)\right\} \quad , \qquad (4\text{-}62)$$

where R and G are random numbers lying between 0 and 1. The inverse erf(G) corresponds to the following equations:

$$\mathrm{erf}(U) = G \quad , \tag{4-63}$$

and

$$U = \text{Inverse erf}(G) \quad , \tag{4-64}$$

i.e, random U is evaluated from the random generated number G by using Eq. 4-64, and erf(G) is the error function of the argument G. This corresponds to an evaluation of erf(U) for several numbers and storing of this information in the computer. G's, the randomly generated numbers are then matched with the stored numbers to give U. The plus and minus signs in Eq. 4-62 are also added to the y-component velocity in a random manner.

The normalized expressions for $\dot{x}_{e,p}$ and $\dot{y}_{e,p}$ of the emitted electrons are given by

$$\frac{\dot{x}_{e,p}}{\dot{x}_{i,o}} = \sqrt{\frac{kT}{|e|\,\varphi_o}}\sqrt{\frac{M}{m}}\,(-\,\ell n\,R)^{1/2} \tag{4-65}$$

and

$$\frac{\dot{y}_{e,p}}{\dot{x}_{i,o}} = \pm\sqrt{\frac{kT}{|e|\,\varphi_o}}\sqrt{\frac{M}{m}}\ \text{Inverse}\ \left\{\mathrm{erf}(G)\right\} \ , \tag{4-66}$$

where $\dot{x}_{i,o}$ refers to the ion injection velocity at the plane x=0, and $\dot{x}_{e,p}$ and $\dot{y}_{e,p}$ refer to the two velocity

components of an electron emitted at the pth time interval.

J. Evaluation of Thrust

The thrust on a ship is caused by electrostatic forces on the two conducting grids. The expression for T, the thrust per unit area on a conducting plane, is given by

$$T = \frac{q_s}{g} \frac{E_{right} + E_{left}}{2} , \tag{4-67}$$

where q_s = charge per unit area, g = weight-to-mass ratio, E_{right} and E_{left} are the normal electric fields on the two sides of the conducting plane, and division by 2 is made to take the average value of the field. From Maxwell equations the surface charge q_s is given by

$$q_s = - \epsilon_o (E_{right} - E_{left}) . \tag{4-68}$$

By using Eqs. 4-67 and 4-68, the following is obtained:

$$T = \frac{\epsilon_o}{2g} \left[E^2_{left} - E^2_{right} \right] . \tag{4-69}$$

For the two conducting grids the expression T_j is given by

$$T_j = \frac{\epsilon_o}{2g} \left[E^2_{4,j} - E^2_{3,j} + E^2_{2,j} - E^2_{1,j} \right] , \tag{4-70}$$

where suffix j refers to a particular rectangle in the transverse direction and E_1, E_2, E_3 and E_4 are the fields on the two sides of the two grids, as indicated in Fig. 4-4. Under ideal conditions $E_{1,j} = 0$,

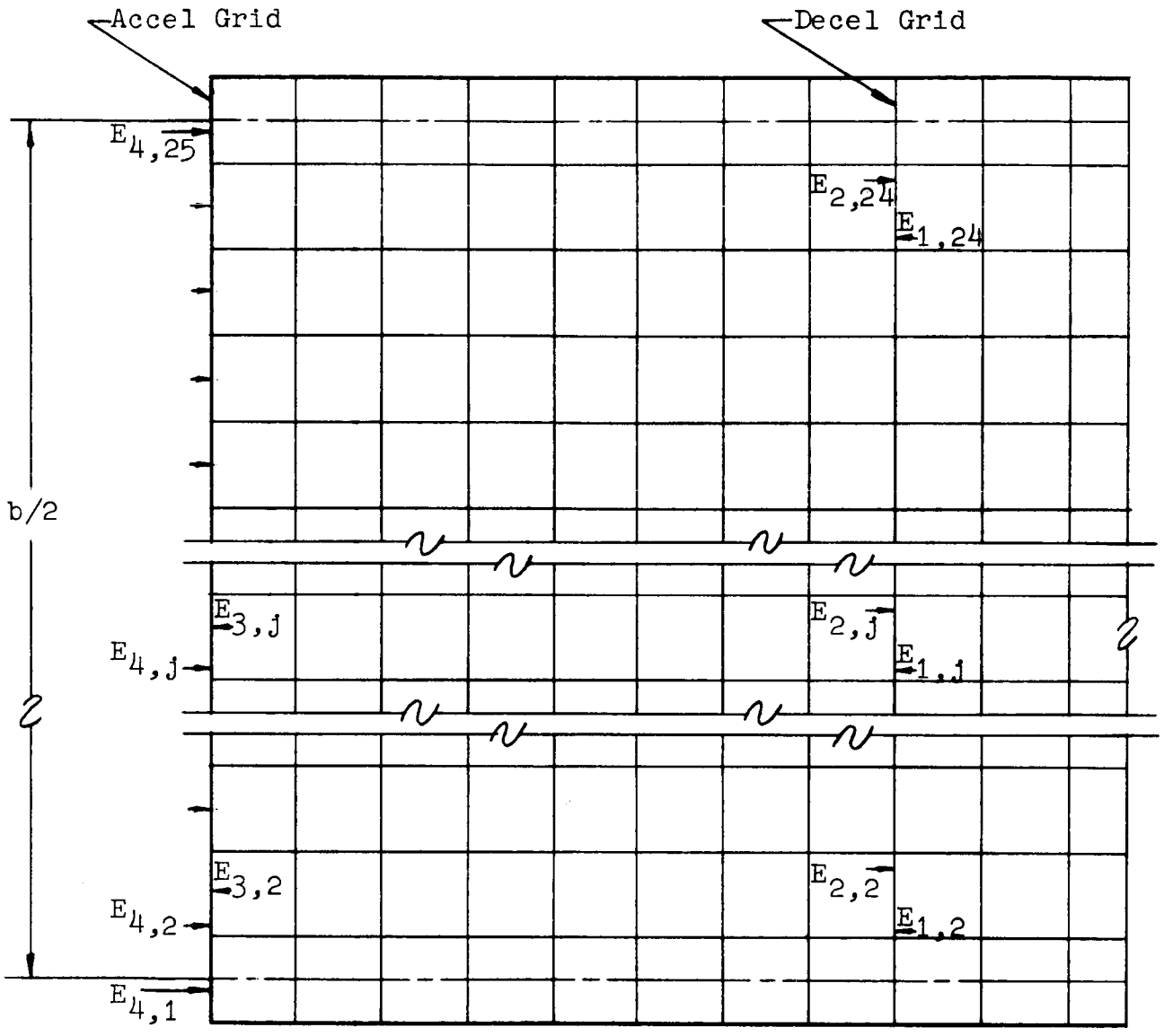

SCHEMATIC OF DIVISION OF THE HALF PERIOD FOR THRUST EVALUATION

Fig. 4-4

$$E_4 = \frac{4}{3}\frac{\varphi_o}{L} \quad , \tag{4-71}$$

and

$$E_3 = E_2 = -\frac{\varphi_o}{\ell}\left(1 - \frac{\varphi_1}{\varphi_o}\right) \quad . \tag{4-72}$$

Thus, the ideal value of T^*, the thrust per unit area, is given by

$$T^* = \frac{8}{9}\frac{\epsilon_o}{g}\left(\frac{\varphi_o}{L}\right)^2 \quad . \tag{4-73}$$

The normalized value of T with respect to T^* is then given by

$$\frac{T_j}{T^*} = \frac{9}{16}\left(\frac{L}{\varphi_o}\right)^2 \left[E_{4,j}^2 - E_{3,j}^2 + E_{2,j}^2 - E_{1,j}^2\right] \tag{4-74}$$

The average value of T, the normalized thrust, is then given by

$$\frac{T}{T^*} = \frac{9}{8}\frac{\Delta y}{b}\left(\frac{L}{\varphi_o}\right)^2 \sum_j \left[E_{4,j}^2 - E_{3,j}^2 + E_{2,j}^2 - E_{1,j}^2\right] \quad , \tag{4-75}$$

where summation over j refers to summing over the appropriate sums for the various rectangles in the transverse direction in the half period only, and a division by $b/2\Delta y$ is made to obtain the average value of the normalized thrust. Since the contributions due to dc fields have been taken into account by adding an equivalent charge, as indicated in Eq. 4-28, the evaluation of E's in Eq. 4-75 corresponds to contribution from both dc fields and space-charge fields. Using Eqs. 4-71 and the definition of V given by Eq. 4-9, the following is obtained:

$$\frac{T}{T^*} = \frac{2\Delta y}{b} \sum_j \left\{ 1 - \frac{\left(\frac{\Delta x}{\ell}\,\frac{2\ell}{3L}\right)^2}{(\omega_p \Delta t)^4} \left[\left(\frac{\partial V_j}{\partial x/\Delta x}\right)_3^2 + \left(\frac{\partial V_j}{\partial x/\Delta x}\right)_1^2 - \left(\frac{\partial V_j}{\partial x/\Delta x}\right)_2^2 \right] \right\} , \quad (4\text{-}76)$$

where suffixes 1, 2, and 3 refer to the corresponding suffixes for E's defined earlier and suffix i with V's is omitted for convenience. In each rectangle the contributions in evaluating normal fields from the third term on the right-hand side of Eq. 4-41 for $y-y_j > o$ will cancel with those for $y-y_j < o$. The value of $(x/\Delta x - x_1/\Delta x)$ for the grids is equal to 1/2, and thus the fields used in Eq. 4-76 are given by

$$\left(\frac{\partial V}{\partial x/\Delta x}\right)_3 = - V_a + 4V_1 + 3\varphi_1 \quad , \quad (4\text{-}77)$$

$$\left(\frac{\partial V}{\partial x/\Delta x}\right)_1 = - V_b + 4V_9 \quad , \quad (4\text{-}78)$$

and

$$\left(\frac{\partial V}{\partial x/\Delta x}\right)_2 = V_c - 4V_8 \quad , \quad (4\text{-}79)$$

where

$$\varphi_1 = - \left(\frac{3L}{2\ell}\right)^2 \left(\frac{\ell}{\Delta x}\right)^2 (\omega_p \Delta t)^2 \, \frac{1}{2} \, \frac{\varphi_d}{\varphi_o} \quad , \quad (4\text{-}80)$$

and is derived by using Eq. 4-9. The value of φ_d/φ_o is taken as positive. In the derivation of fields as given by Eqs. 4-77,

4-78, and 4-79, only linear terms are included, which is quite reasonable. By substituting for fields as given by Eqs. 4-77 through 4-80, the expression for thrust is given by

$$\frac{b}{2\Delta y}\frac{T}{T^*} = \sum_j \left\{ 1 - \frac{\left(\frac{\Delta x}{\ell}\frac{2\ell}{3L}\right)^2}{(\omega_p \Delta t)^4} \left[(-V_a + 4V_1 + 3\varphi_1)^2 + (-V_b + 4V_9)^2 - (V_c - 4V_8)^2 \right] \right\} \tag{4-81}$$

For an ideal case, when there is complete space-charge neutralization $(\partial V/\partial x/\Delta x)_1$, which is the middle term within parenthesis on the right hand side of Eq. 4-81, is equal to zero. Under these conditions

$$(-V_a + 4V_1 + 3\varphi_1) = (V_c - 4V_8) \quad , \tag{4-82}$$

and an ideal thrust is produced on the ship.

K. Definition of Symbols used in Two-Dimensional Configuration

a	width of the ion beam (in half period) at the accel grid plane
b	length of period in the transverse direction
c	y-coordinate of the lower edge of the electron emitter
d	y-coordinate of the upper edge of the electron emitter
E_{xT}	total x-component electric field
E_{yT}	total y-component electric field
e	charge of an ion
G	random number associated with y-component electron velocity
g	weight-to-mass ratio
J	ion current density at the accel grid plane
K	total number of rectangles in the half period (along the y-axis)
kT	Boltzman constant multiplied by electron emitter temperature in ^{o}K
k	order of harmonic, k=0, 1, 2, ..., 24
L	ion gun-accel grid spacing
L'	distance of the shelf (beam-plasma boundary) from the accel grid
ℓ	accel-decel grids spacing
M	ion mass
m	electron mass
N	total number of ions in the region between the accel and decel grids, when drifting at the injection velocity
$N(x_i, y_j)$	total number of ions-minus-electrons in the i-jth rectangle
N_e	number of electrons emitted per unit time interval
N_i	number of ions injected across the accel grid in a unit time interval
q^*	normalized charge per unit length
q_ℓ	line charge per unit length
q_s	surface charge per unit area
R	random number associated with x-component electron velocity
T	thrust per unit area
T^*	ideal thrust per unit area
$U_{i,k}$	kth harmonic of $\varphi_{i,j}$

u_o ion velocity at the accel grid plane

$V_{i,j}$ normalized potential corresponding to $\varphi_{i,j}$

X (units) normalized x distance

$X_{i,k}$ kth harmonic of $V_{i,j}$

$\dot{x}_{e,p}$ x-component of electron velocity emitted at the pth time interval

$\dot{x}_{i,o}$ x-component of the ion injection velocity

x_n x-coordinate of a particle at nth time step

Y (units) normalized y distance

$\dot{y}_{e,p}$ y-component of electron velocity emitted at the pth time interval

y_n y-coordinate of a particle at nth time step

β larger root of the algebraic equation given by Eq. 4-23

Δt unit time interval

Δx spacing between two consecutive centroids along the x-axis

Δy spacing between two consecutive centroids along the y-axis

ϵ_o free space permittivity

η absolute value of the ratio of electron charge to its mass

λ $\Delta x/\Delta y$

λ_D Debye length

ρ_o ion space-charge density at the accel grid plane

$\rho_{i,j}$ space-charge density at the i-jth centroid

$\bar{\rho}_{i,k}$ kth harmonic of $\rho_{i,j}$

$\sum$ summation

φ_o accel grid potential

φ_1 normalized value of φ_d

φ_d potential difference between the accel and decel grids

$\varphi_{i,j}$ actual potential at the i-jth centroid

φ/φ_o normalized ship potential

$\psi_{i+1/2,k}$ kth harmonic of a quantity analogus to field

ω_p electron plasma radian frequency

V. RESULTS OF TWO-DIMENSIONAL ELECTRON-ION MIXING

A. Considerations in Computer Simulation

Because of the enormity of the two-dimensional problem, it was found necessary to consider computer efficiency and storage in simulating the problem on the computer. While efficiency in computer time has been appreciably improved by using new techniques, the limited computer memory restricts the tracking of the charged particles to somewhat shorter distances from the decel grid, as compared to those possible in the one-dimensional model. In selecting the size of each mesh, it is necessary that the space-charge fields be resolved within a Debye length. From the results of the one-dimensional analysis it appears that adequate space-charge neutralization occurs within short distances from the decel grid; this makes it convenient to specify, within computer limitations, the distance beyond the decel grid which may be desirable for tracking the charged particles. Based on these considerations, the total number of rectangles (meshes) in the transverse direction in each period was taken as 48 (because of symmetry, only half of the period was analyzed). There are eight rectangles between the two grids and 192 rectangles beyond the decel grid. Such a division has yielded a fairly good resolution, and adequate space-charge neutralization seems

to occur within the region studied.

Because of computer memory limitations, relatively few locations were left to store the coordinates of the particles, and it was considered necessary to pack the x- and y-coordinates of each particle in a single computer word. This arrangement restricted the range of mass ratios which could be used, because heavy ions experience space-charge forces which cannot be specified within the number of decimal places allowed. Nevertheless, a comparison of data for several mass ratios has enabled us to extrapolate the results for high mass ratios. The necessity for increasing the value of the normalized charge for achieving maximum possible accuracy is explained in the next few sections. All the subroutines used in the main program were checked independently against several test cases.

B. Choice of Parameters

Because of the several computer limitations described in Section A, considerations of Debye length and application of the results to practical cases, etc., it was considered important to optimize the various parameters, such as ion and electron injection currents and velocities, ion beam width, electron emission ratio, etc. As mentioned in Section V.A, the accuracy in the decimal parts of the x- and y-coordinates of a particle are limited; this made it

necessary to consider larger values of the normalized charge to make the space-charge forces more applicable. For small values of the normalized charge, the space-charge forces may not be large enough to show any ion-beam spreading (as noticed from the plots in the next section), particularly when the value of the ion-mass ratio is increased. However, due to this change, the value of the unit-time interval is also increased, causing the particles to move very rapidly during one interval. Thus, it is important to make a compromise so that accuracy in results is not impaired. (It may be mentioned here, however, that in every case the results were in good agreement with the results of several test cases simulated for checking accuracy.) Moreover, with increased value of the unit-time interval, the electrons, particularly those with high initial velocities, move a considerable distance in the first unit-time interval; in some cases this may even cause some electrons to travel to the accel grid. This effect is more pronounced, especially for small values of ion-mass ratio, when the value of the dc voltage between the two grids is small. For this reason, a modification, successfully used by Berger[13], was used for the initially emitted electrons: the trajectory equations for such an electron are given by the following:

---

13. Berger, P., Stanford University. Private communication.

$$x - x_o = \frac{1}{2} \dot{x}_o \Delta t + \frac{1}{6} \ddot{x}_o \frac{(\Delta t)^2}{2} \qquad (5\text{-}1)$$

and

$$y - y_o = \frac{1}{2} \dot{y}_o \Delta t + \frac{1}{6} \ddot{y}_o \frac{(\Delta t)^2}{2} \quad , \qquad (5\text{-}2)$$

where suffix o refers to the initial time. The derivation of these equations assumes that electrons are emitted continuously rather than at discrete time intervals. These trajectory equations are also used in the normalized form as discussed in Section IV.

The total number of binary bits in a 36-bit IBM 7094 word is most efficiently used; the first 18 bits are used to store the y-coordinate, while the last 18 bits are used to store the x-coordinate. These coordinates are stored in fixed point mode, which makes it necessary to use a combination of fixed and floating point modes in the computer program, since most of the program is in floating point words.

C. Variation with Ion Mass Ratio

After the optimization of the various parameters and the modifications mentioned in the last section were incorporated, the electron-ion mixing mechanism was studied for three values of mass ratio. This study made it possible to extrapolate the results to the actual values of the mass ratio, as described in Section V.G. The various

input parameters and calculated constants for the three cases described in this section are given in Table 5-1.

Table 5-1

Input Parameters and Calculated Constants										
Run No.	M/m	ℓ/L	$\frac{e\varphi_o}{kT}$	N_i	N	C/φ_o	θ	q^* $\times 10^{-3}$	V_R	$\frac{\lambda_D}{\Delta x}$
3B	64	2.25	6.4	3	90	-0.88	0.2822	1.777	3.61	2.11
2E	144	1.5	14.4	"	"	-0.39	"	"	"	"
4A	256	1.125	25.6	"	"	-0.22	"	"	"	"

λ_D = Debye length (defined by Eq. 5-3), $\theta = \omega_p \Delta t$ (defined by Eq. 4-54), q^* = normalized dimensionless charge per unit length (defined by Eq. 4-11), v_R = ratio of the average electron emission velocity to the ion exit velocity (defined by Eq. 5-4), and C = normalization constant for potential (defined by Eq. 4-9). The run numbers (2E, 3B, 4A) are used here merely for reference purposes. The variations in ℓ/L and $e\varphi_o/kT$, as mentioned above, were necessary to maintain identical conditions in all the three cases (except M/m). In all the cases mentioned in Table 5-1, $a/\ell = 0.75$ (defined by Eq. 4-52), $\varphi_d/\varphi_o = 0.25$ (defined in Section IV.E.3), $N_e/N_i = 4$, and the absorption ratio = 1/4, where N_e and N_i represent the number of

electrons and ions emitted per unit time interval, respectively, and the absorption ratio is defined as the number of electrons absorbed over the number of electrons crossing the decel grid above the ion beam. In all cases $\ell/\Delta x=8$. The other parameters are defined in Section IV.H. The expression for $\lambda D/\Delta x$ is given by the following equation:

$$\frac{\lambda_D}{\Delta x} = \frac{v}{\Delta x\ \omega_p}$$

$$= \frac{3}{2}\frac{L}{\ell}\frac{\ell}{\Delta x}\sqrt{\frac{kT}{e\varphi_o}} \quad , \qquad (5\text{-}3)$$

where v = average electron velocity; Eq. 4-12 is used in deriving Eq. 5-3. It is assumed that the presence of ions does not significantly change the plasma frequency of the system. The expression for v_R in Table 5-1 is given by the following equation:

$$v_R = \sqrt{\frac{\pi kT}{2m}} \left[\frac{1}{2\eta\varphi_o(1 - \frac{\varphi_1}{\varphi_o})\ \frac{m}{M}}\right]^{1/2}$$

$$= \left[\frac{\pi}{4}\ \frac{kT}{e\varphi_o}\ \frac{M}{m}\ \frac{1}{(1 - \frac{\varphi_1}{\varphi_o})}\right]^{1/2} \qquad (5\text{-}4)$$

Ions are injected across the plane x=0, 0.2 Δy apart, between 0 and 5.8 Δy, and electrons are emitted with random initial velocity components at the plane x=8 from points 0.2 Δy apart between 6 and 10 Δy. One particle for every 26 particles was selected for trajectory plotting purposes. Figures 5-1 through 5-3 show the trajectories of typical ions in the x-y space for the three cases mentioned in Table 5-1. Because of the symmetry across y=0 (and y=24) the movement of particles from one half period to the other half period may easily be seen in the plots in Figs. 5-1 through 5-3. The ion-beam spreading for the three cases is compared in Table 5-2.

Table 5-2

Variation of Ion-Beam Spread with Ion Mass

Run No.	M_1/M_s	N_e/N_1	ℓ_1/ℓ_2
2E	2.25	4	2.19
2F	2.25	2	2.32
4A	4	4	4.35

M_s refers to the mass of an ion with an ion-electron mass ratio of 64; the cases of different values of mass ratio are compared with respect to the case of M/m=64. The ratio ℓ_1/ℓ_2 is a measure of the ion-beam spread

$\frac{M}{m} = 64, \quad \frac{\ell}{L} = 2.25, \quad N_i = 3, \quad N = 90, \quad \frac{a}{\ell} = 0.75,$

$\frac{\varphi_1}{\varphi_o} = 0.4, \quad \frac{N_e}{N_i} = 4, \quad \omega_p \Delta t = 0.2822, \quad \frac{e\varphi_o}{kT} = 6.4$

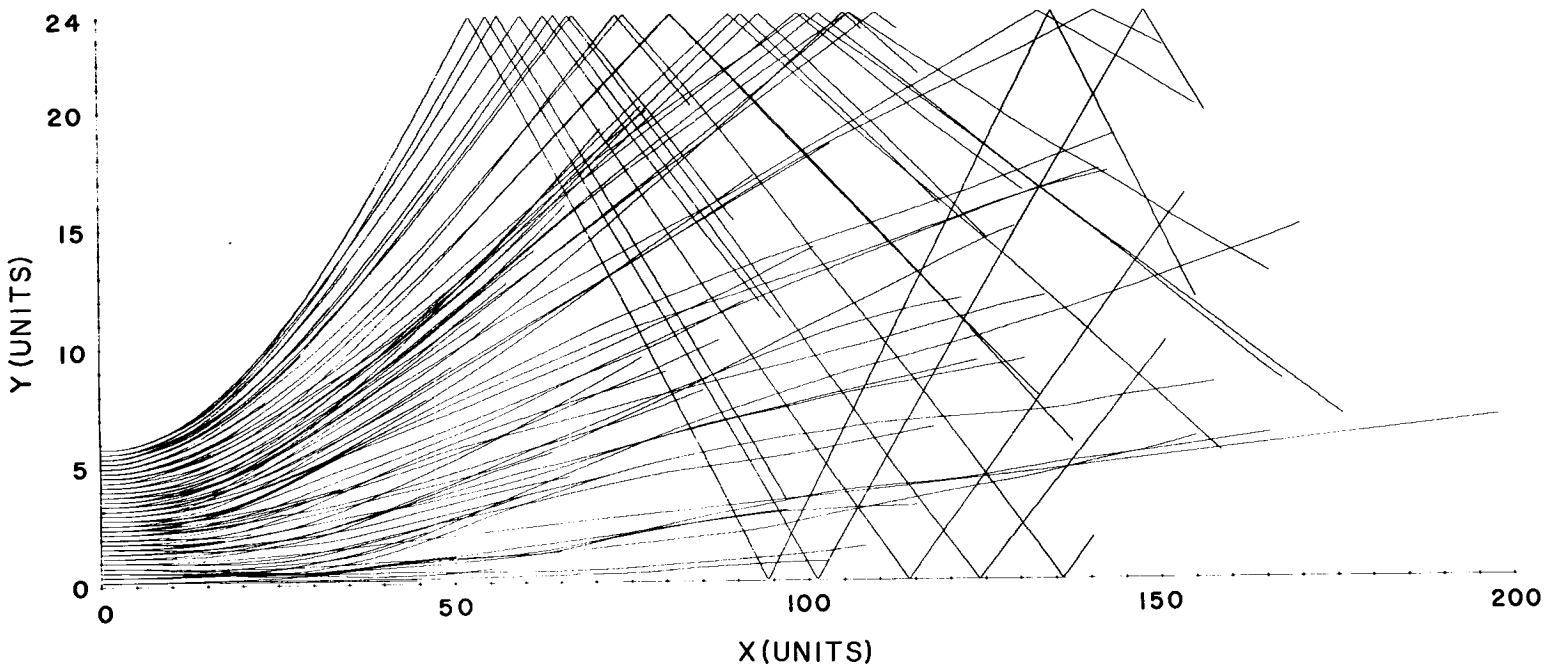

Y VERSUS X, IONS, (RUN 3B)

Fig. 5-1

$$\frac{M}{m} = 144, \quad \frac{\ell}{L} = 1.5, \quad N_i = 3, \quad N = 90, \quad \frac{a}{\ell} = 0.75,$$

$$\frac{\varphi_1}{\varphi_o} = 0.4, \quad \frac{N_e}{N_i} = 4, \quad \omega_p \Delta t = 0.2822, \quad \frac{e\varphi_o}{kT} = 14.4$$

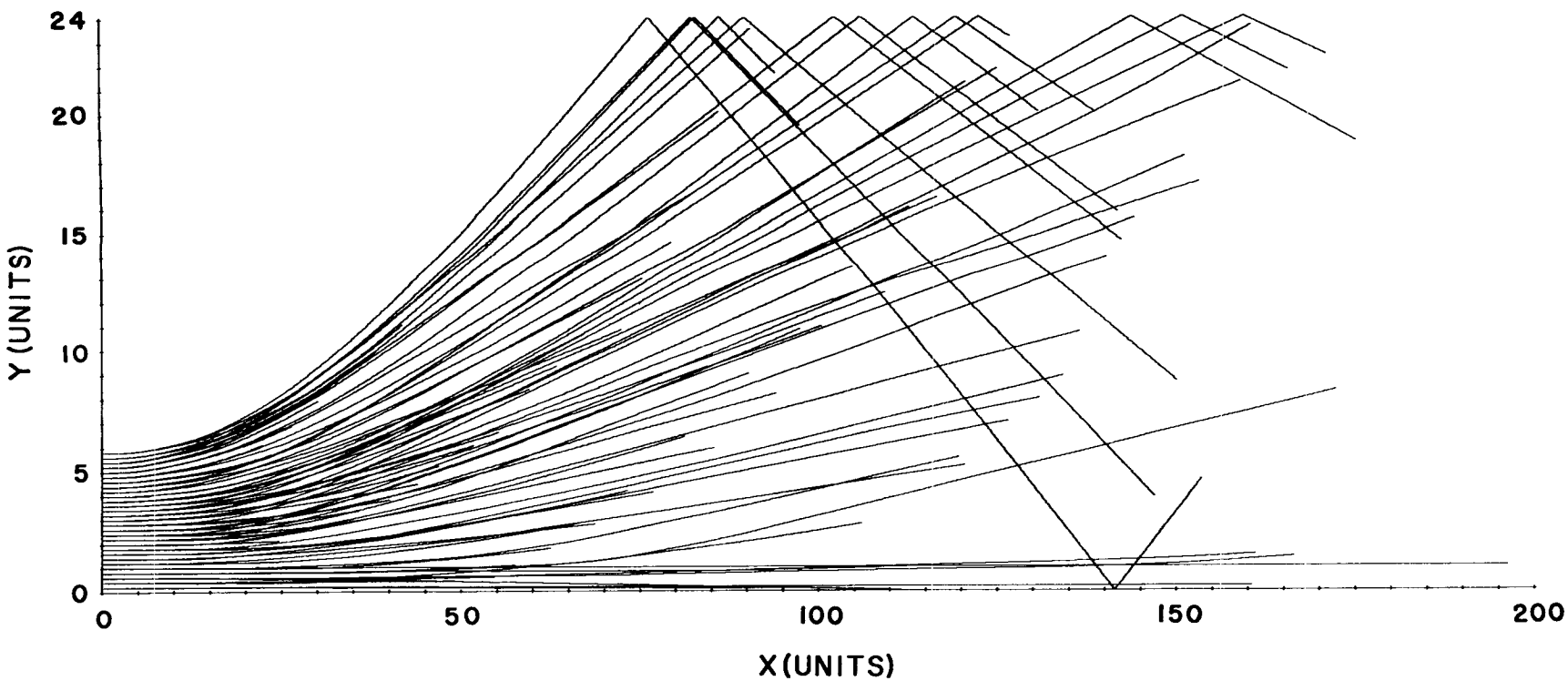

Y VERSUS X, IONS, (RUN 2E)

Fig. 5-2

$$\frac{M}{m} = 256, \quad \frac{\ell}{L} = 1.125, \quad N_i = 3, \quad N = 90, \quad \frac{a}{\ell} = 0.75,$$

$$\frac{\varphi_1}{\varphi_o} = 0.4, \quad \frac{N_e}{N_i} = 4, \quad \omega_p \Delta t = 0.2822, \quad \frac{e\varphi_o}{kT} = 25.6$$

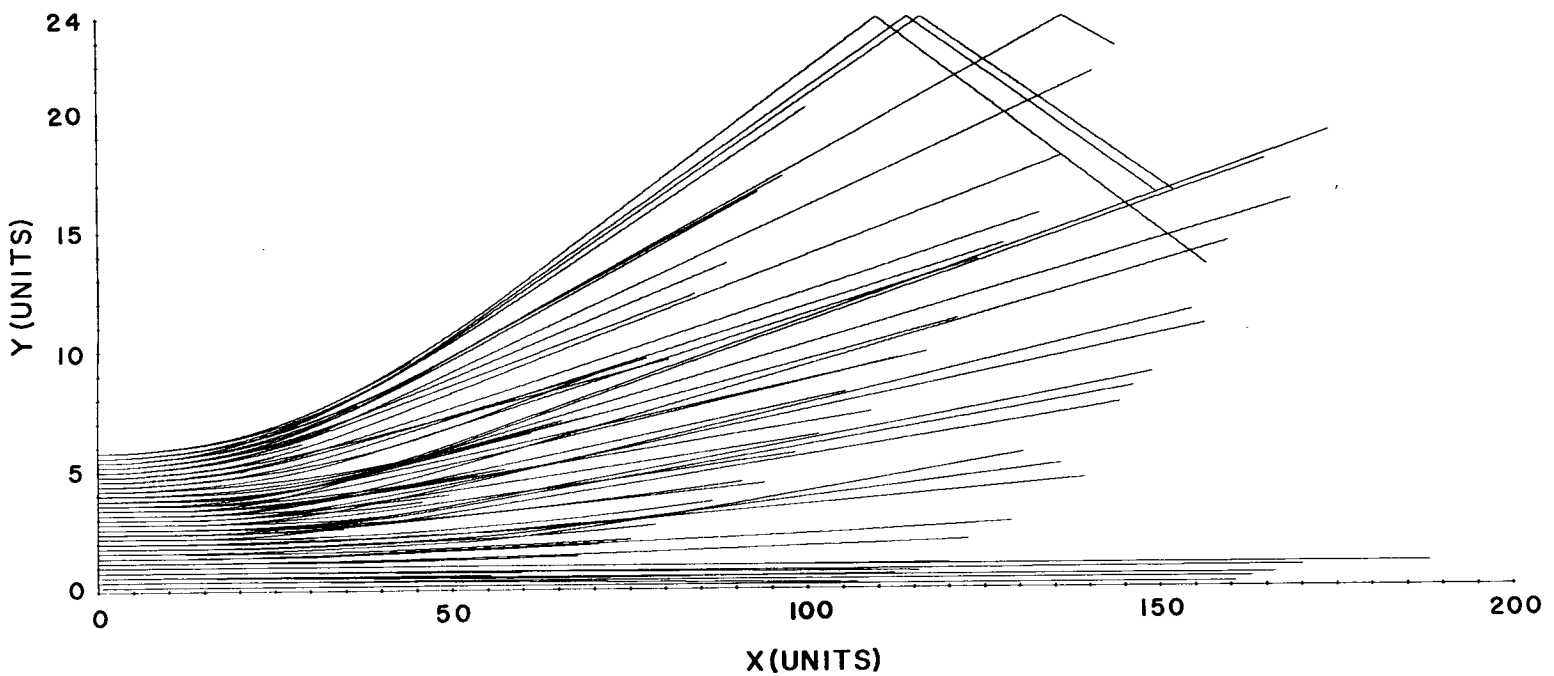

Y VERSUS X, IONS, (RUN 4A)

Fig. 5-3

(ℓ_1 and ℓ_2 are defined in Fig. 5-4). Run 2F, where electron emission has been reduced (as compared to that in Run 2E) is discussed in detail in the next section. It may be noticed that the ion-beam spread is inversely proportional to the ion mass, and, for the case of reduced electron emission, the ion beam spread is slightly increased. The transverse movement of ions, as seen in Figs. 5-1 through 5-3, is caused by their own space-charge, which is partially neutralized by electrons. Beyond some value of x (different for each case), no further transverse bending of ions occurs, which may be due either to small ion density or adequate space-charge neutralization; a close comparison of the trajectory plots does seem to favor the second explanation.

Figure 5-5 shows the typical ion trajectories (x vs. t) for the case of M/m=144. The ions experience straight line movement, except for some initial deceleration due to the decel voltage, indicated by slight bending of the ion beam in the range $0<x<8$. The initially emitted ions experience slight acceleration due to a finite attraction by several electrons. The initial injection velocity and decel voltage are kept constant in all the three cases described in Table 5-1; the trajectories for the other two cases are found to be identical, except that the acceleration of the initially emitted ions is <u>increased</u> for the

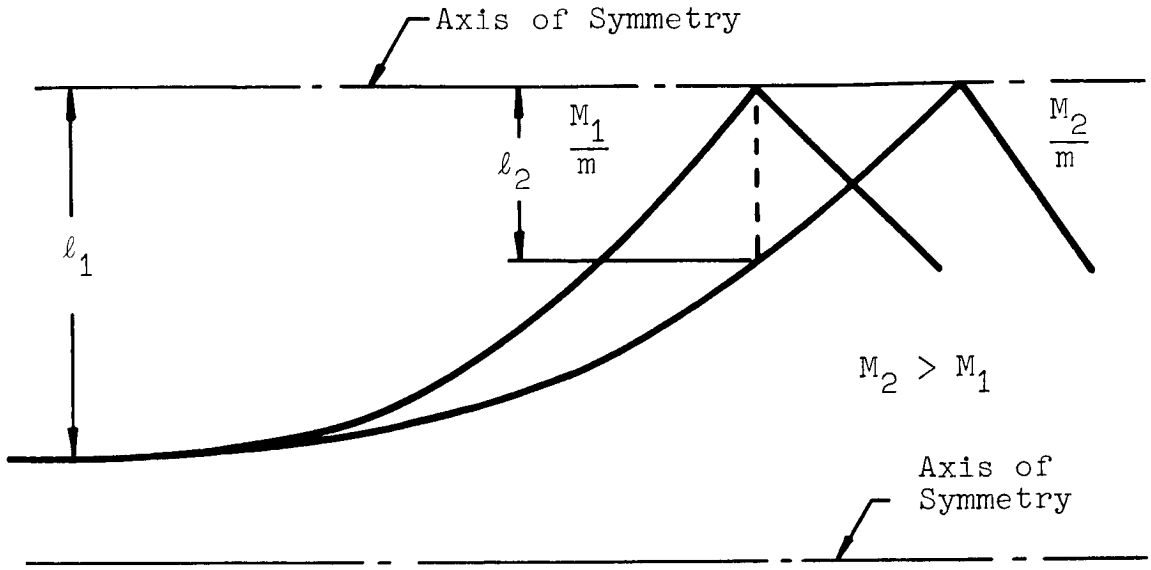

VARIATION OF ION-BEAM SPREADING WITH ION MASS

Fig. 5-4

$\frac{M}{m} = 144, \quad \frac{\ell}{L} = 1.5, \quad N_i = 3, \quad N = 90, \quad \frac{a}{\ell} = 0.75$

$\frac{\varphi_1}{\varphi_2} = 0.4, \quad \frac{N_e}{N_i} = 4, \quad \omega_p \Delta t = 0.2822, \quad \frac{e\varphi_o}{kT} = 14.4$

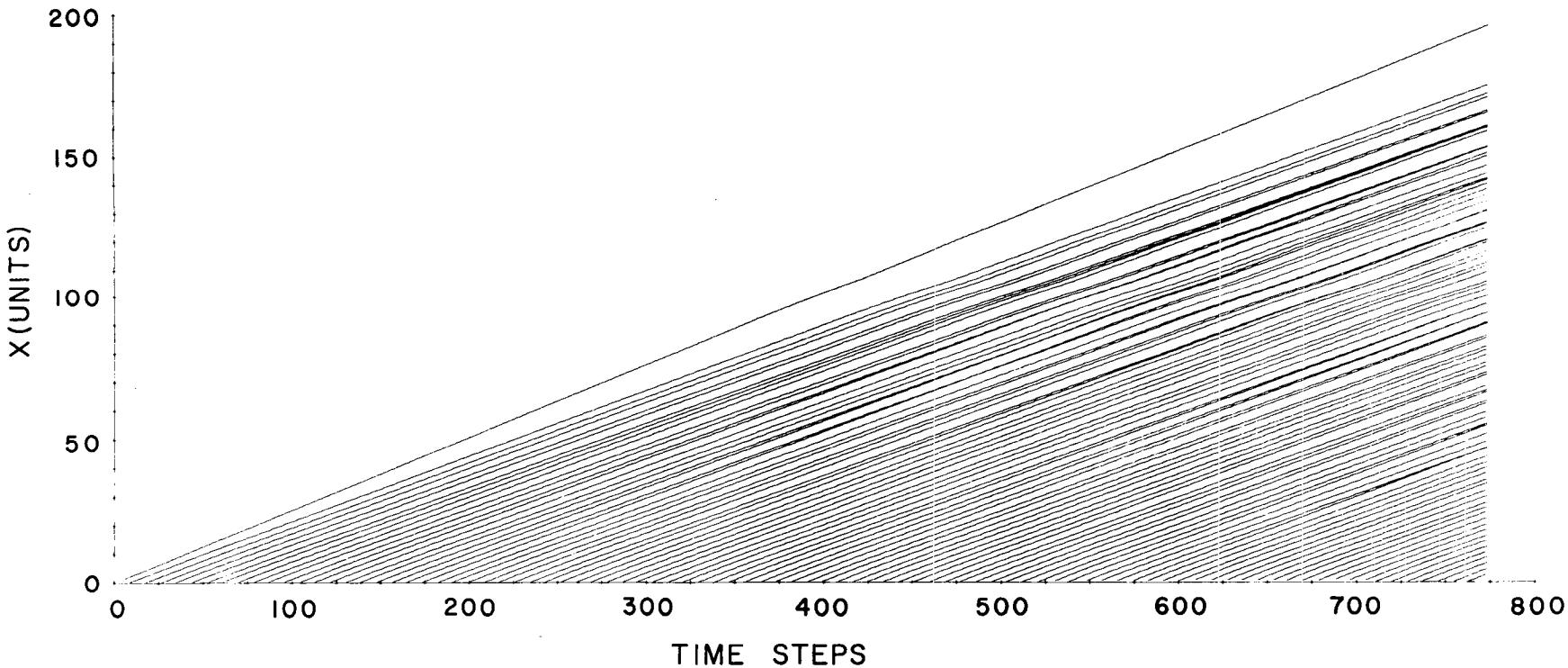

X VERSUS TIME, IONS, (RUN 2E)

Fig. 5-5

case of M/m=64 and decreased for the case of M/m=256; this is due to change in ion mass. Figure 5-6 shows the typical electron trajectories in the x-y space for the entire run. It is interesting to note that the complete decel grid forms a virtual electron emitter, although electrons are emitted from a rather narrow strip. This is primarily due to the potential distribution in the neighborhood of the decel grid, shown in Figs. 6-8 and 6-9. The electrons mix into the ion beam by means of fluctuating fields which admit nearly the correct number of electrons with approximately the required velocity into the ion beam. This was qualitatively explained in the sixth quarterly report[14], where the total number of electrons-minus-ions reached a steady-state level with oscillations at approximately electron plasma frequency. A close examination of the electron trajectories indicates that the electrons experience oscillatory motion in the transverse direction; an electron moving towards y=0 goes into the lower half symmetric period, and an electron moving away from y=0 actually comes from the lower half period. This oscillatory motion is found to be very closely correlated with the plasma frequency oscillations

---

14. R.P. Wadhwa, "Analysis of Electron-Ion Mixing in Ion Engines", Quarterly Rpt. No. 6, Contract No. NAS 3-2503; December. 1963.

$$\frac{M}{m} = 256, \quad \frac{\ell}{L} = 1.125, \quad N_i = 3, \quad N = 90, \quad \frac{a}{\ell} = 0.75,$$

$$\frac{\varphi_1}{\varphi_o} = 0.4, \quad \frac{N_e}{N_i} = 4, \quad \omega_p \Delta t = 0.2822, \quad \frac{e\varphi_o}{kT} = 25.6$$

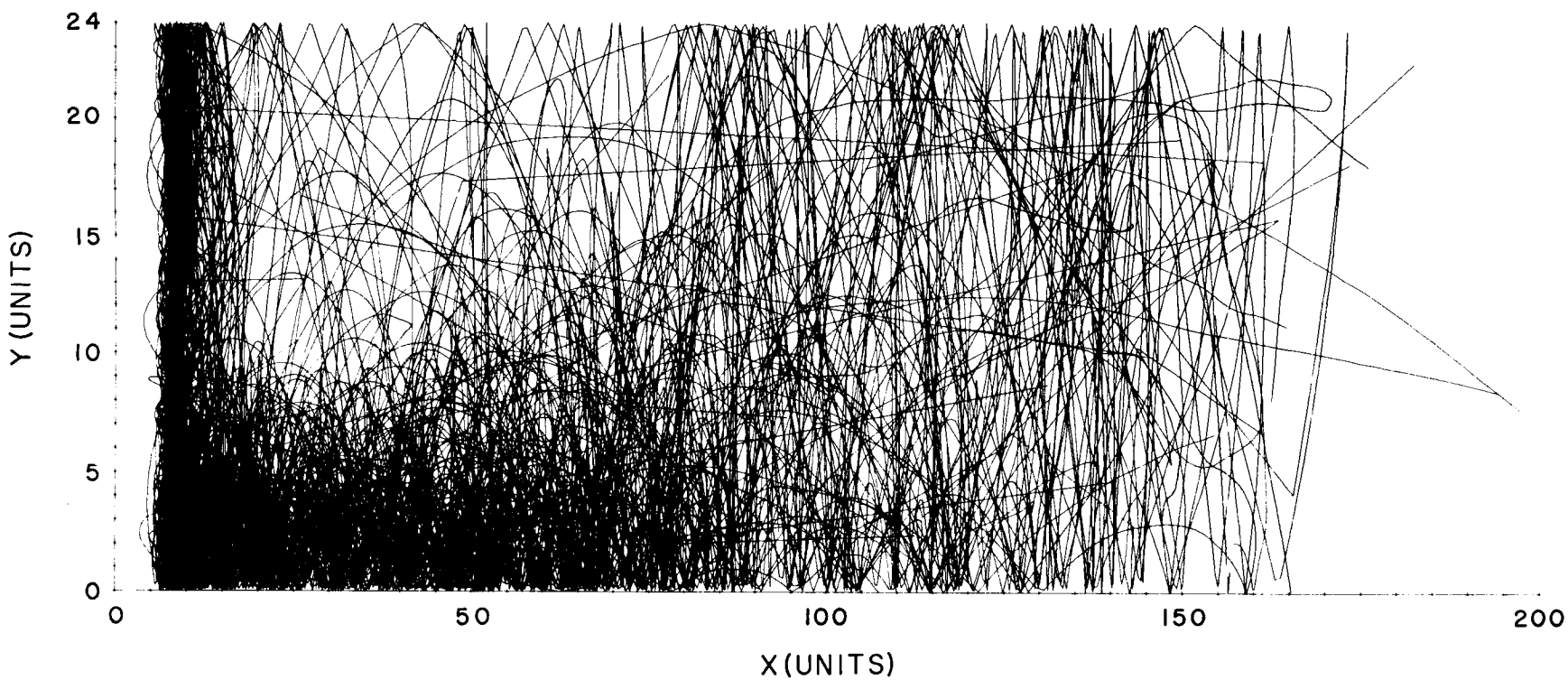

Y VERSUS X, ELECTRONS, (RUN 4A)

Fig. 5-6

in the transverse direction visible on the plots for a relatively small sample of electrons in the time and space domain, given in the sixth quarterly report[14], although the system plasma frequency seems to be modified because of the presence of ions.

Figure 5-7 shows the envelopes for the high electron density regions for the three cases mentioned in Table 5-1. These curves show a qualitative but comparative illustration of electron trajectories in the various cases; a comparison of trajectories in Fig. 5-6 with the corresponding envelope in Fig. 5-7 qualitatively indicates what the trajectories should look like for other cases. The location of the electron emitter is also shown in Fig. 5-7. A comparison of electron cloud envelopes with the ion trajectories in Figs. 5-1 through 5-3 indicates that electrons follow ions very closely. After a certain value of x (different for three cases) which nearly corresponds to ion moving toward y=0, the whole space is filled with electrons. The formation of the electron cloud envelope in the region between the two grids is correlated with the shelf development for the one-dimensional case in Section V.H.

Typical electron trajectories (x vs. time) are shown in Figs. 5-8 and 5-9 for the cases of M/m=256 and 64, respectively. The fast electrons moving ahead of the beam bounce from free space, and are eventually carried along with the ion beam. The value of v_R in this case,

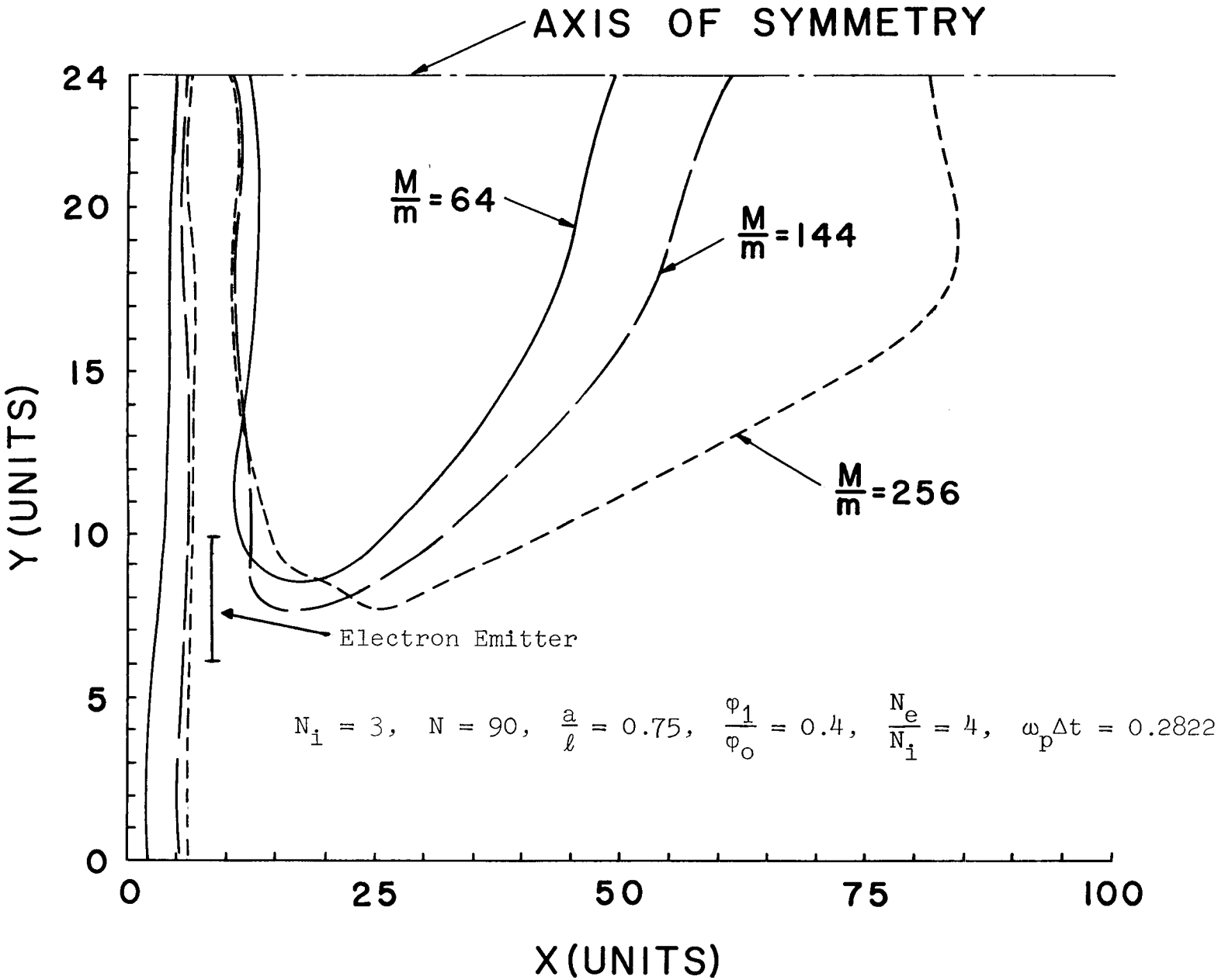

ELECTRON CLOUD ENVELOPE IN NORMALIZED SPACE
(FOR DIFFERENT ION MASS RATIOS)

Fig. 5-7

$\frac{M}{m} = 256, \quad \frac{\ell}{L} = 1.125, \quad N_i = 3, \quad N = 90, \quad \frac{a}{\ell} = 0.75,$

$\frac{\varphi_1}{\varphi_o} = 0.4, \quad \frac{N_e}{N_i} = 4, \quad \omega_p t = 0.2822, \quad \frac{e\varphi_o}{kT} = 25.6$

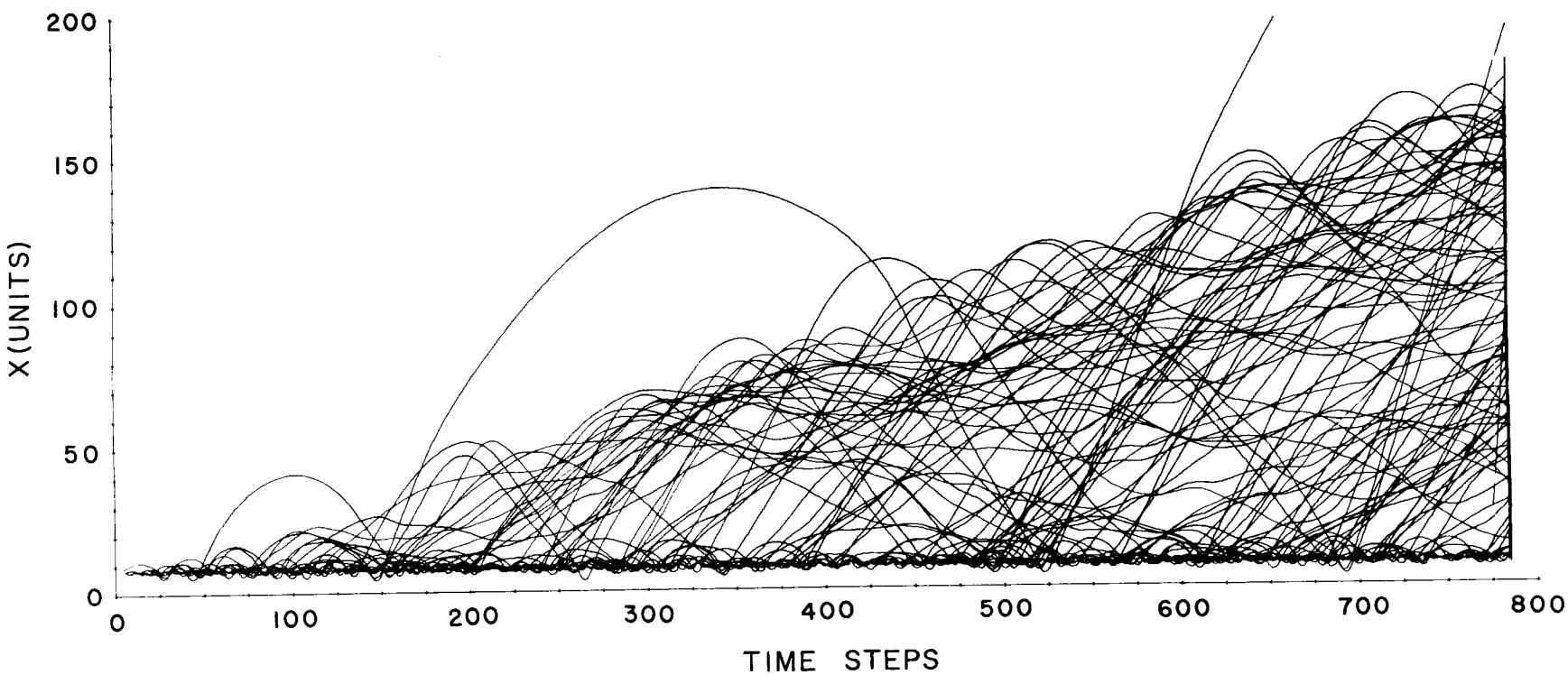

X VERSUS TIME, ELECTRONS, (RUN 4A)

Fig. 5-8

$\frac{M}{m} = 64, \quad \frac{\ell}{L} = 2.25, \quad N_i = 3, \quad N = 90, \quad \frac{a}{\ell} = 0.75,$

$\frac{\varphi_1}{\varphi_o} = 0.4, \quad \frac{N_e}{N_i} = 4, \quad \omega_p t = 0.2822, \quad \frac{e\varphi_o}{kT} = 6.4$

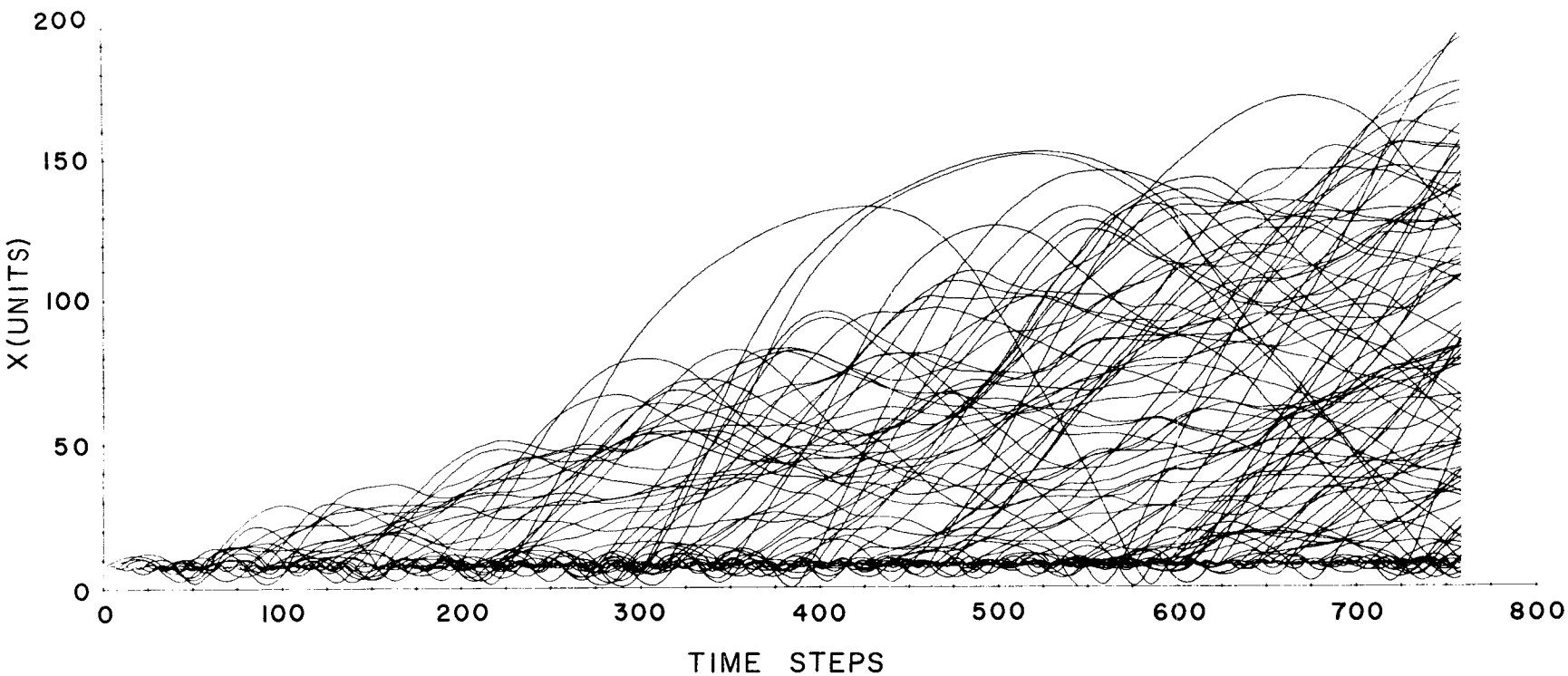

X VERSUS TIME, ELECTRONS, (RUN 3B)

Fig. 5-9

as mentioned in Table 5-1, is equal to 3.61, although the ultimate velocity of electrons seems to be very close to that of the ions; this indicates that electrons slow down and lose energy. Because of heavy mass of ions, the increase in ion energy (which is gained from electrons) is not evident from the trajectories in Fig. 5-5. For the case of small mass ratio (M/m=64), the value of the dc field between the two grids is small, and some of the fast-velocity electrons do reach the accel grid, as noticed from the plots in Fig. 5-9. These electrons will eventually be accelerated towards the ion source. In a practical case, the value of M/m is very high, and the turning back of electrons, as noticed for the case of M/m=64, should not be of any concern.

The variation of the normalized thrust as a function of time for the two cases (M/m=64 and 256) is shown in Fig. 5-10. In general, the variations in thrust are small and are not detrimental to the ion engine performance. It is interesting to note that the variations for the case of M/m=256 (heavy ion) are smaller than those for the case of M/m=64 (lighter ion). The variations in the thrust for the case of M/m=144 are in between those for the cases of M/m=64 and 256; the corresponding curve is not drawn here, because this would reduce the distinction in the variations for the various cases. The reduction in

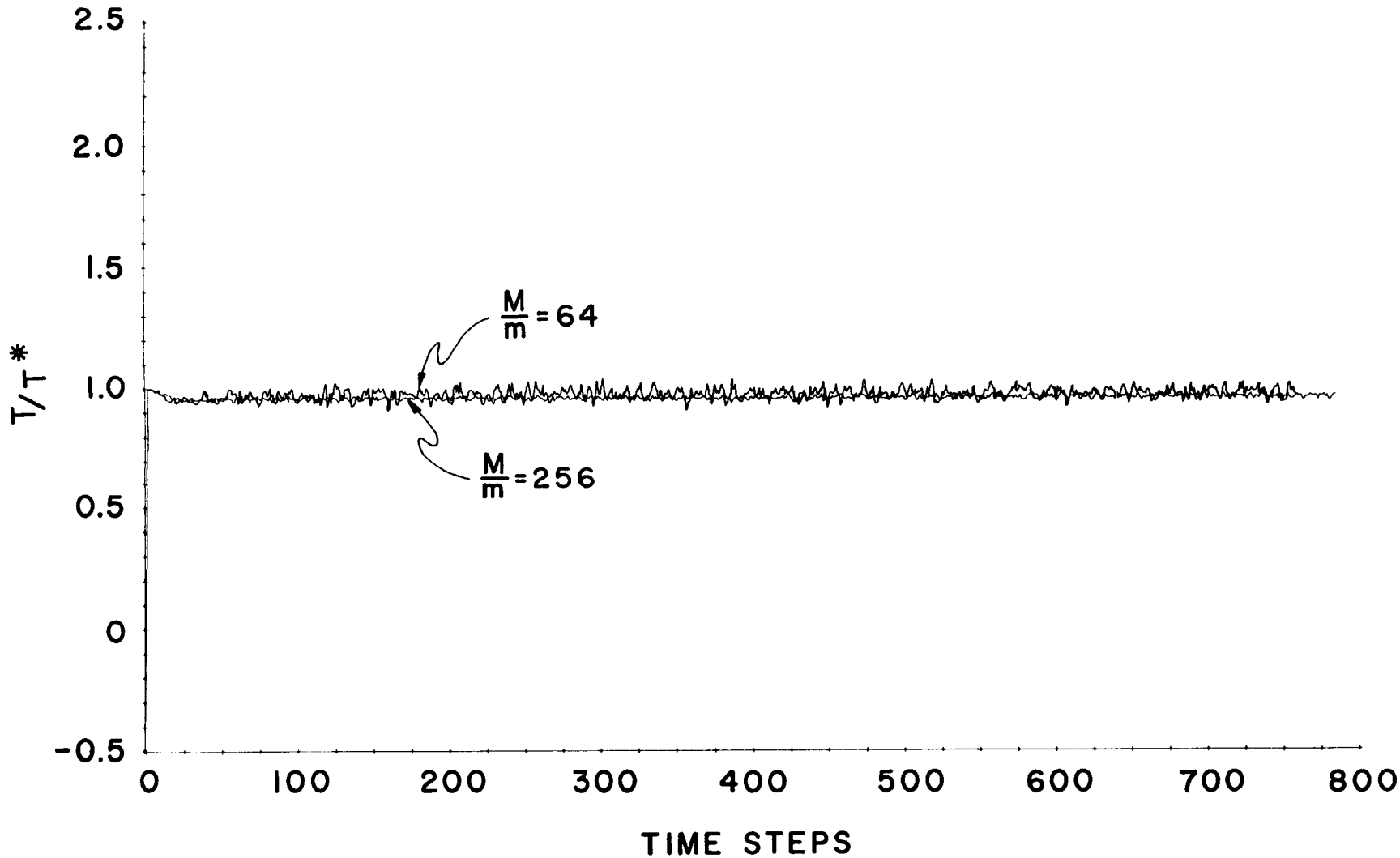

THRUST VERSUS TIME; VARIATION WITH ION MASS

Fig. 5-10

thrust variations for the heavy ion seems to be due to reduction in ion-beam spreading. For practical cases the ion beam spreading would be very small (because of increase in ion mass), and the thrust variations are expected to be considerably less than those observed for the cases studied in this section.

In general, the value of the normalized thrust is slightly less than unity, which is probably due to the fact that under conditions of neutralization plasma extends in the region between the two grids; the value of $|E_2|$ (see Fig. 4-4) is thus reduced, while the value of $|E_3|$ is not changed appreciably. As noticed from the expression for the normalized thrust, such a condition would lead to a reduction in thrust. From the curves given in Fig. 5-10 it appears that such a condition is reached within very few unit intervals, and the variations in thrust are too small to be identified by electron or ion plasma frequency oscillations.

Figure 5-11 shows the variation of the normalized ship potential as a function of time for the three different cases. In general, the ship potential is positive, because more electrons have left the ship at the time when ship potential is evaluated. As mentioned earlier, in evaluating ship potential it is assumed that the beam beyond x=200 is completely neutralized, so that the effect of particles beyond x=200 is negligible.

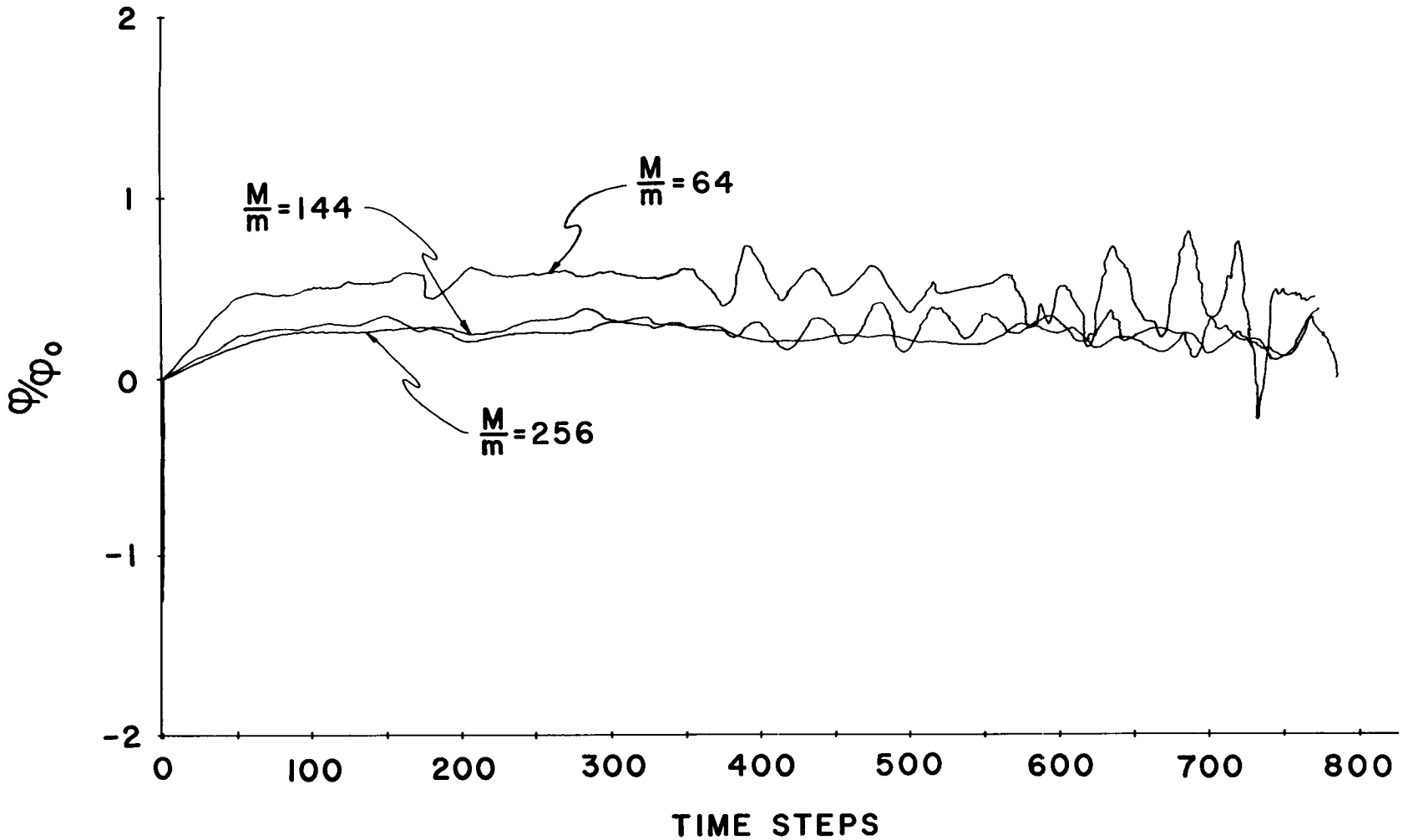

SHIP POTENTIAL VERSUS TIME; VARIATION WITH ION MASS

Fig. 5-11

The ship potential and potential distribution are calculated precisely until the particles reach x=200. When a particle or particles reach x=200 and are written off, the evaluation of the ship potential in particular is no longer precise; the neglect of these particles affects potential distribution appreciably only in the vicinity of x=200. This discrepancy in evaluating the ship potential is indicated by relatively large fluctuations at large values of time.

The fluctuations in the ship potential are less for the case of heavy ions, and, moreover, the average value of the ship potential is closer to zero for heavy ions. These observations indicate that the fluctuations for the thrust and ship potential for cesium (and mercury) ions would be extremely small. A higher degree of space-charge neutralization seems to occur for the case of heavy ions, primarily because the ion-beam spread is less; all the electrons are drawn into the ion-beam instead of filling up the whole space.

D. Variation with Electron Emission

It is shown in Section 5.C that the ion beam spread is inversely proportional to the value of the ion mass. Some calculations for the ion beam spread without any space-charge neutralization indicated that there was definitely adequate space-charge neutralization in the vicinity of the decel grid. The effect of variable electron emission on the performance of the ion engine is compared for three different values of

N_e/N_i (these parameters are defined in Section V.C), namely, 4, 2 and 0 corresponding to Runs 2E (described in Section V.C), 2F, and 2G, respectively, while all the other variables are maintained constant. This comparison is of interest since the performance of the ion engine can be impaired if the electron emission is not sufficient; it should be almost optimum. For the case of $N_e/N_i = 2$ the ion beam spread was slightly increased (as mentioned in Table 5-2). The envelopes for high density electron clouds for the two cases, namely $N_e/N_i = 4$ and 2 are shown in Fig. 5-12 which also shows the location of the electron emitter. Because of reduced number of electrons in the second case, the space-charge forces on electrons are reduced, and the electrons move shorter distances from the decel grid; most of the electrons move into the ion beam, and the qualitative behavior of electrons away from the decel grid is similar in the two cases. These results indicate that even this reduced electron emission is adequate for space-charge neutralization. There seems to be no significant difference in the other trajectories for ions and electrons. Figures 5-13 and 5-14 show the typical ion trajectories for the case of $N_e/N_i = 0$ in the x-y and x-t domains, respectively; all the other parameters are the same as those for Run 2E mentioned in Table 5-1. It may be clearly seen that the ions can be drawn back to the ship, when the space-charge neutralization is not adequate and only very few ions would be able to move into free space. A comparison of

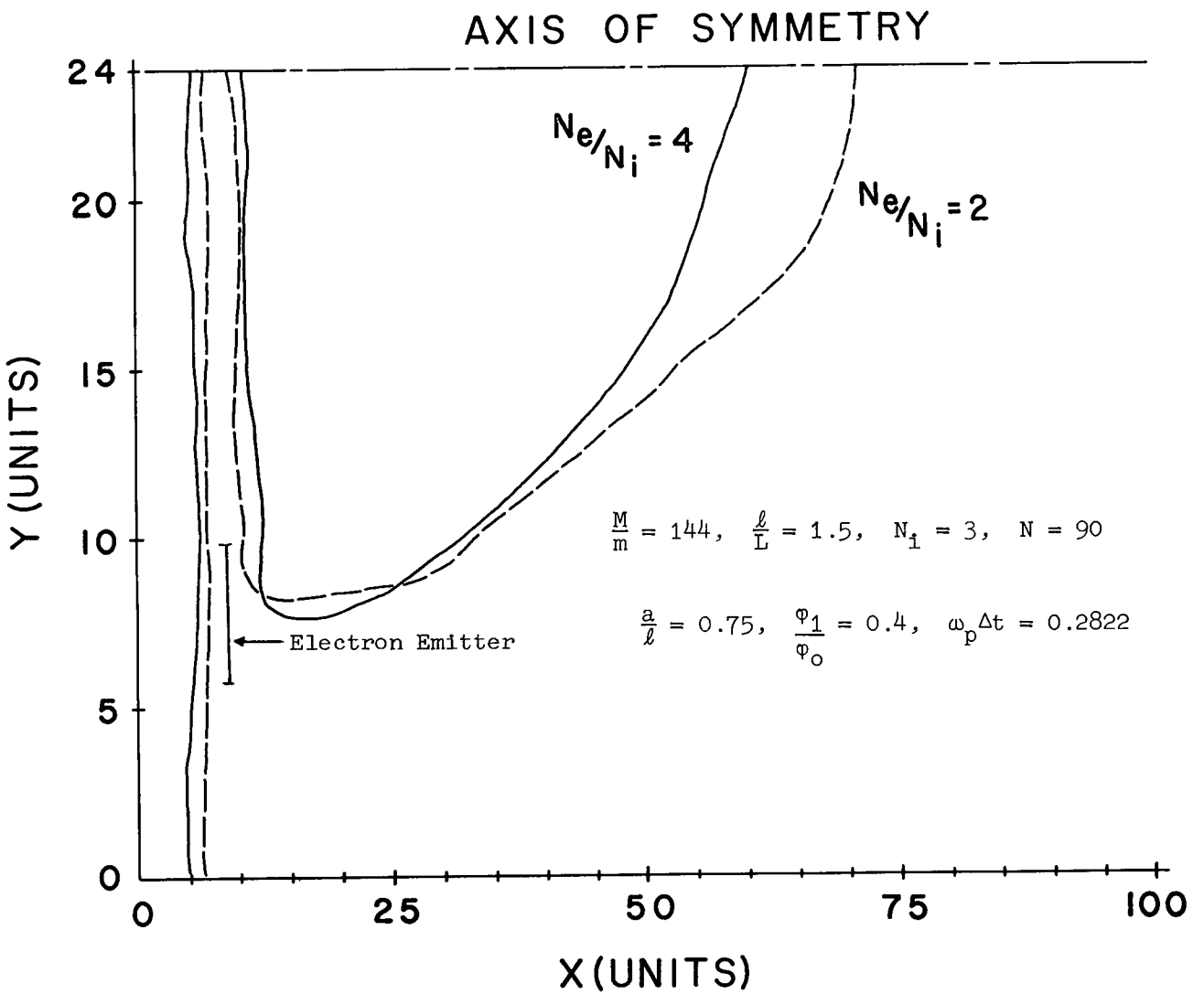

ELECTRON CLOUD ENVELOPE IN NORMALIZED SPACE FOR DIFFERENT ELECTRON EMISSIONS

Fig. 5-12

$\frac{M}{m} = 144, \quad L = 1.5, \quad N_i = 3, \quad N = 90, \quad \frac{a}{L} = 0.75,$

$\frac{\varphi_1}{\varphi_o} = 0.4, \quad \frac{N_e}{N_i} = 0, \quad \omega_p \Delta t = 0.2822$

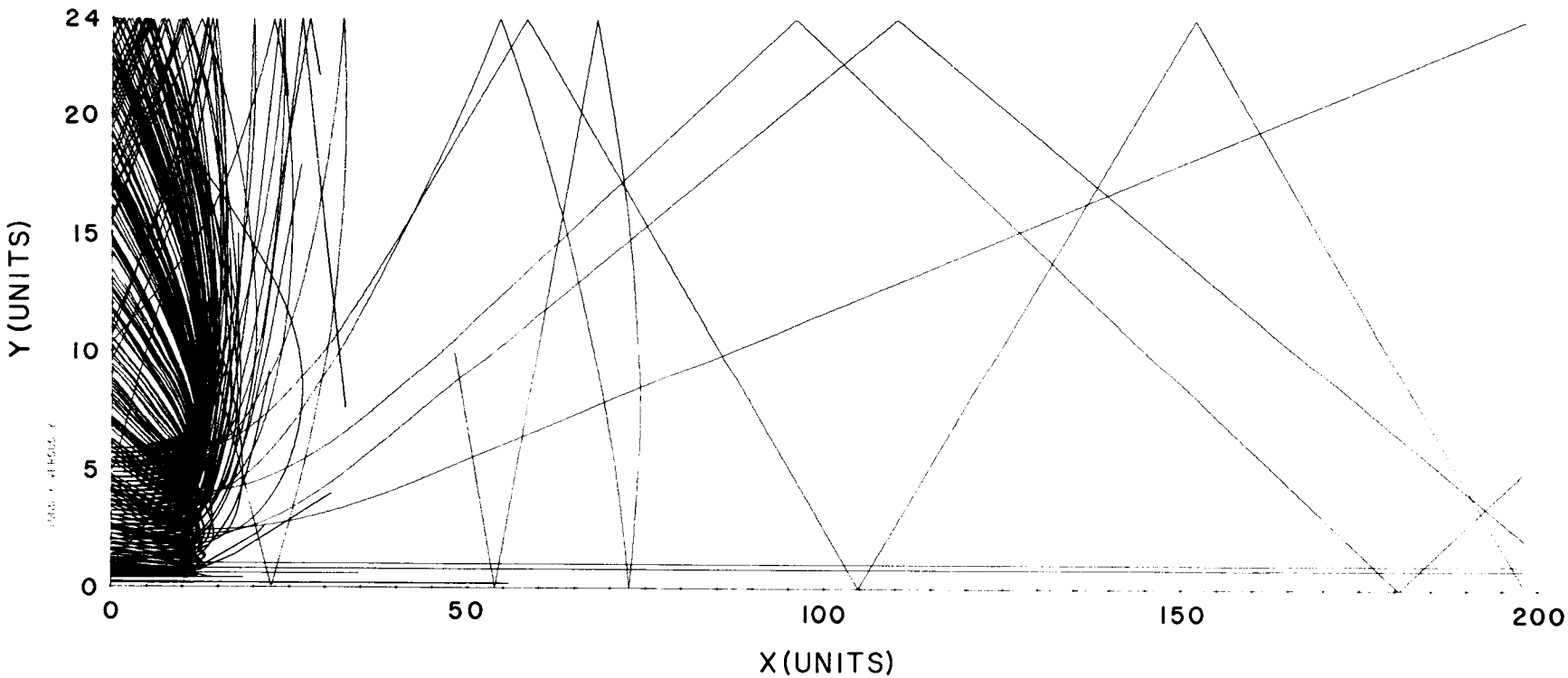

Y VERSUS X, IONS, (RUN 2G)

Fig. 5-13

$$\frac{M}{m} = 144, \quad \frac{\ell}{L} = 1.5, \quad N_i = 3, \quad N = 90, \quad \frac{a}{\ell} = 0.75,$$

$$\frac{\varphi_1}{\varphi_o} = 0.4, \quad \frac{N_e}{N_i} = 0, \quad \omega_p \Delta t = 0.2822$$

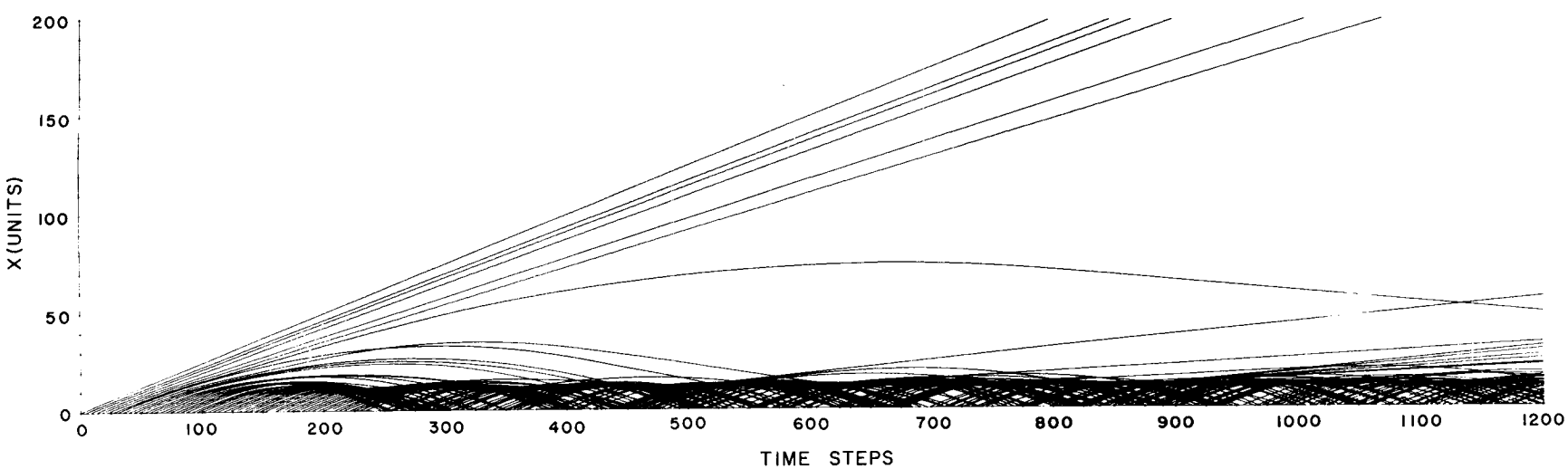

X VERSUS TIME, IONS, (RUN 2G)

Fig. 5-14

ion beam spread from Fig. 5-2 and 5-13 for the cases of $N_e/N_i = 4$ and zero, respectively does indicate that adequate space-charge neutralization seems to occur in the vicinity of the decel grid when a sufficient number of electrons is emitted.

The bunching of the ions in Fig. 5-14 seems to be related with the ion plasma frequency oscillations. The number of time steps in a full plasma frequency period is equal to 267, while the bunches are spaced approximately 130 steps apart. A correlation of this bunching with thrust measurements is indicated in the latter part of this section.

The variation of the normalized thrust as a function of time is shown in Fig. 5-15 for the two cases of electron emission, namely, $N_e/N_i = 4$, and 0, corresponding to Run Nos. 2E, 2F and 2G, respectively. Again, as discussed in Section V.C, the thrust is less than the ideal value in all these three cases. The fluctuations in thrust are somewhat reduced as the value of N_e/N_i is changed from 4 to 2, but the value of thrust is also slightly decreased; actually the thrust fluctuations for the case of $N_e/N_i = 2$ are very close to those for the case of N_e/N_i, and only one curve is shown in Fig. 5-15 because the superposition of the two curves reduces the distinction between the two curves. A deterioration in thrust is clearly noticeable for $N_e/N_i = 0$; the thrust deteriorates very fast, reaches a minimum value, and then oscillates between two levels (each level considerably less than unity). This

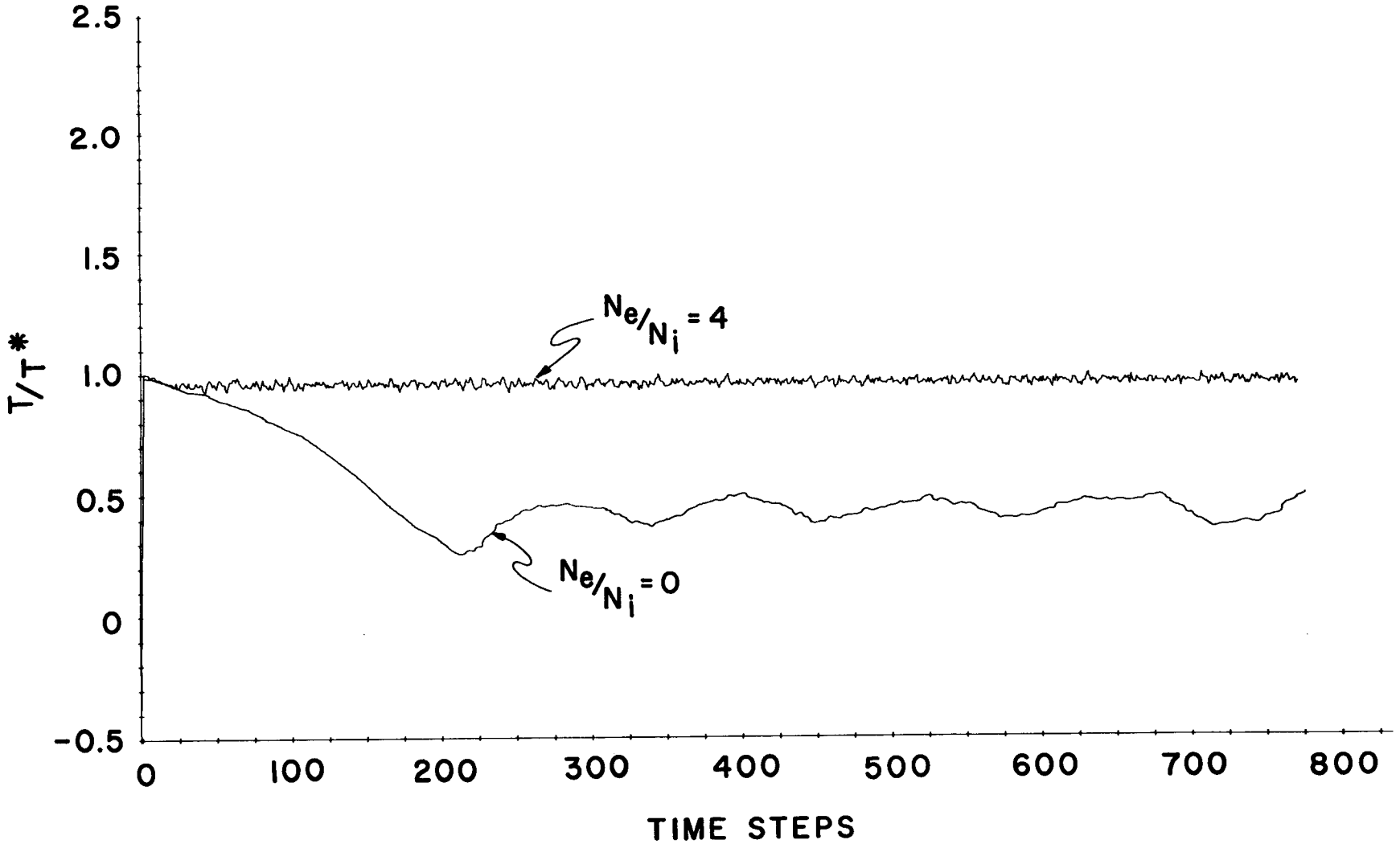

THRUST VERSUS TIME;
VARIATION WITH ELECTRON EMISSION

Fig. 5-15

oscillation frequency is approximately equal to half of the ion plasma frequency; the number of time steps in a full ion plasma frequency oscillation period - 267, while the repetition rate from the plot in Fig. 5-15 is approximately 130. The bunching of ions, as is shown in Fig. 5-14, is also correlated with the same number of time steps.

The expression for thrust derived in Eq. 4-81 does not take into account the contributions of the ions being pulled back; this causes an additional drag on the ship, and thrust deterioration should be worse than indicated by the curve for $N_e/N_i = 0$ in Fig. 5-15.

Figure 5-16 shows the variations in the ship potential for the three cases of emission as a function of time. As mentioned in Section V.C, the ship potential is positive for normal conditions of operation. The ship potential is most positive for the case of highest electron emission, although the fluctuations in ship potential for the case of $N_e/N_i = 2$ are smaller than those for the case of $N_e/N_i = 4$. Again, as mentioned in Section V.C, the evaluation of ship potential at later time steps is questionable. For the case of $N_e/N_i = 0$, the ship potential becomes more and more negative at a decreasing rate, since less and less ions are ejected and the ship builds up negative charge.

E. Variation with Electron Emitter Temperature

In the earlier part of the computer experiments, the effect of the variation of the electron emitter temperature was studied. Two sets of runs, namely 1D and 1E for

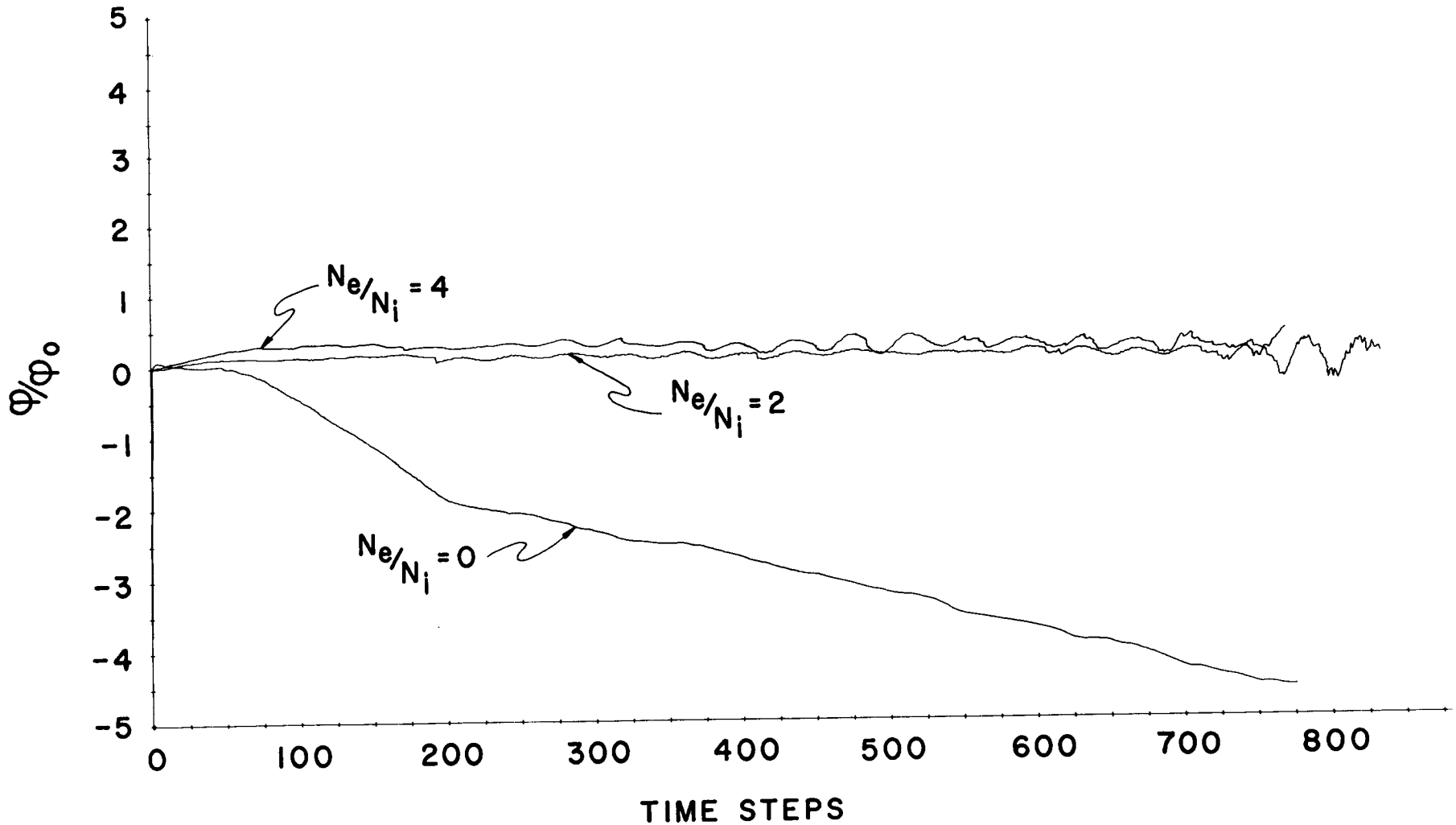

SHIP POTENTIAL VERSUS TIME:
VARIATION WITH ELECTRON EMISSION

Fig. 5-16

$e\varphi_o/kT = 40$ and 100, respectively, were made. These cases correspond to electron velocities less than ion exit velocities and are studied to determine the effect of various electron emitting surfaces. The input parameters and calculated constants are given in Table 5-3.

Table 5-3

Input Parameters and Calculated Constants										
Run No.	$\frac{M}{m}$	$\frac{\ell}{L}$	$\frac{e\varphi_o}{kT}$	N_i	N	$\frac{\lambda_D}{\Delta x}$	θ $x10^{-2}$	q^* 10^{-4}	v_R	$\frac{C}{\varphi_o}$
1D	16	1	40	3	60	1.91	9.43	2.96	0.72	-1.5625
IE	16	1	100	3	60	1.2	9.43	2.96	0.456	-1.5625

Figures 5-17 and 5-18 show typical electron trajectories for the two cases in x-y space. It is clear that, for the case of lower electron emitter temperature, the electrons travel shorter distances in the direction of the accel grid, and the fluctuations of the electrons in the x-y space are also reduced. For both these cases $N_e/N_i = 4$, as in the cases mentioned in Table 5-1. Again, as mentioned in Section V. C, the electron clouds follow patterns like those for the ions in the two respective cases. The ion trajectories are similar to those shown for the cases mentioned in Section V C. Typical electron trajectories (x versus t) are shown in Fig. 5-19 for the case of $e\varphi_o/kT = 40$. It is interesting to note that, because of the reduction in the initial electron velocities, there are a small number of electrons moving ahead of the beam; consequently, the number of reflections of electrons

$\frac{M}{m} = 16 \quad \frac{\ell}{L} = 1 \quad N_i = 3, \quad N = 60, \ \frac{a}{\ell} = 0.75,$

$\frac{\varphi_1}{\varphi_o} = 0.4, \quad \frac{N_e}{N_i} = 4, \quad \omega_p \Delta t = 0.0943, \quad \frac{e\varphi_o}{kT} = 40$

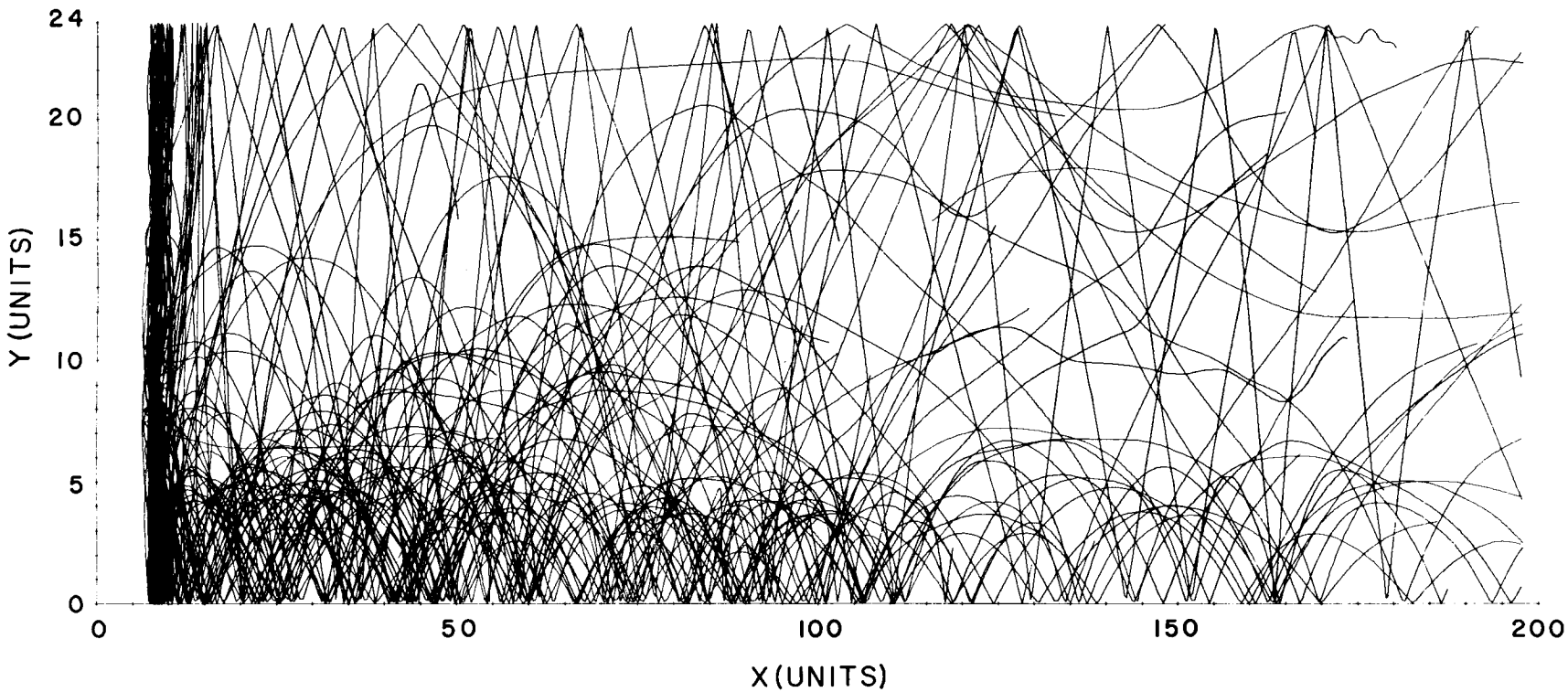

Y VERSUS X, ELECTRONS, (RUN 1D)

Fig. 5-17

$\frac{M}{m} = 16 \quad \frac{\ell}{L} = 1 \quad N_i = 3, \quad N = 60, \quad \frac{a}{\ell} = 0.75,$

$\frac{\varphi_1}{\varphi_o} = 0.4, \quad \frac{N_e}{N_i} = 4, \quad \omega_p \Delta t = 0.0943, \quad \frac{e\varphi_o}{kT} = 100$

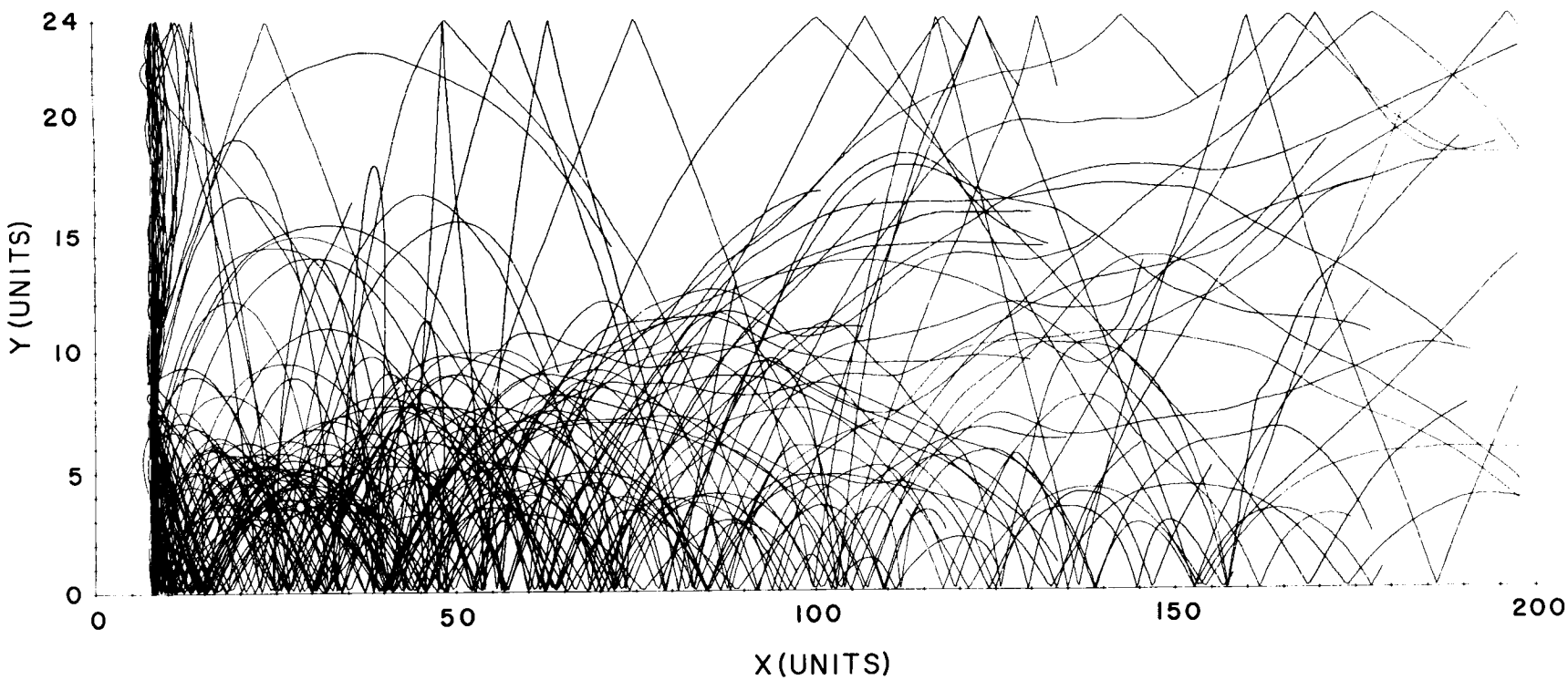

Y VERSUS X, ELECTRONS, (RUN 1E)

Fig. 5-18

$\frac{M}{m} = 16 \quad \frac{\ell}{L} = 1 \quad N_i = 3, \quad N = 60, \quad \frac{a}{\ell} = 0.75,$

$\frac{\varphi_1}{\varphi_o} = 0.4, \quad \frac{N_e}{N_i} = 4, \quad \omega_p \Delta t = 0.0943, \quad \frac{e\varphi_o}{kT} = 40$

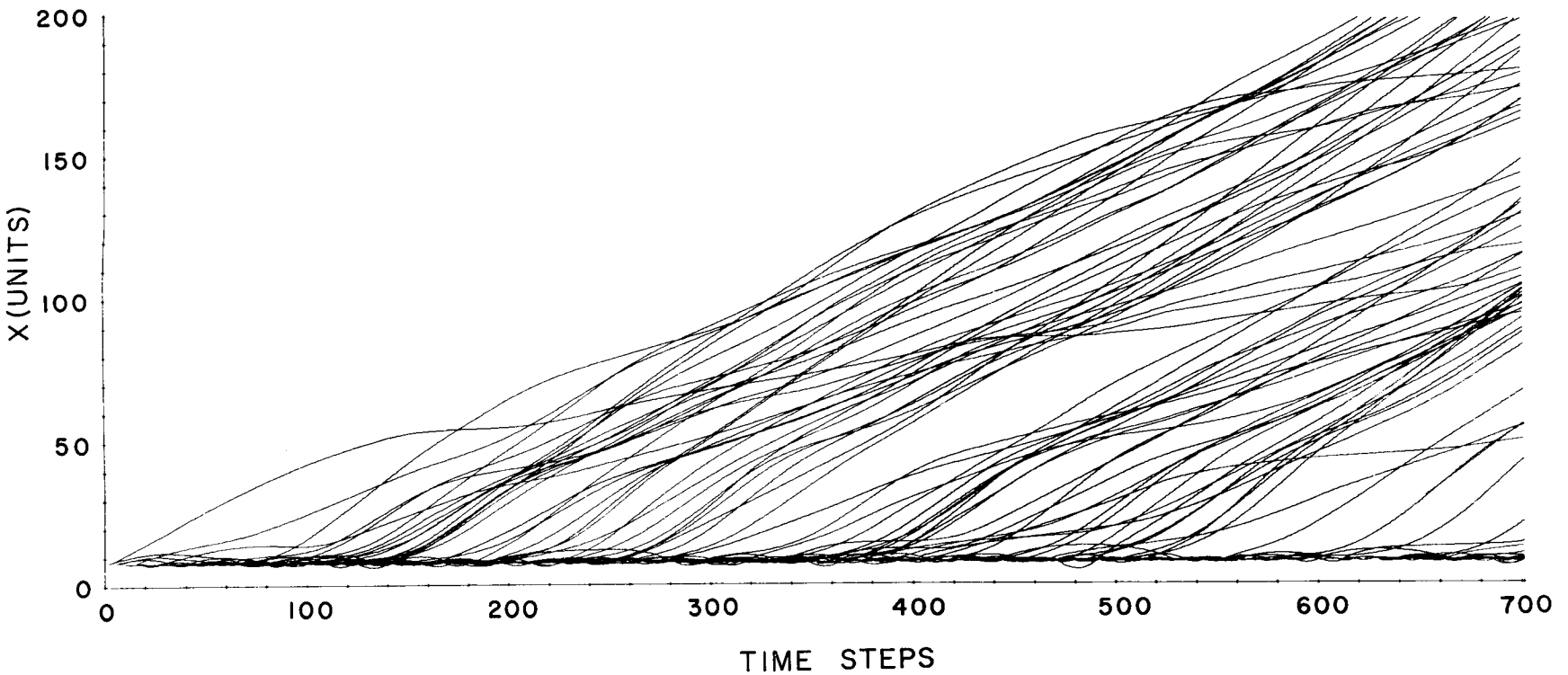

X VERSUS TIME, ELECTRONS, (RUN 1D)

Fig. 5-19

from free space is reduced. The ultimate electron velocities are very close to that of the ion exit velocity, even though the average value of the initial electron velocity is smaller than the ion exit velocity. In other words, electrons picked up energy in this case, while electrons lost energy in the cases discussed in Section V. C. Because of the heavy mass of ions, the change in ion energy is not noticed. In both cases there is some degree of thermalization. The variations in thrust and ship potential are similar to those for the case of $M/m = 144$ (discussed in Section V. C). This indicates that the performance of the ion engine is not affected as long as there is a sufficiently large number of electrons being emitted from either the cold or hot emitter.

F. Variation with Normalized Charge

From the knowledge about the normalization of the parameters and from the comparison study discussed in Section V. C, it is possible to extrapolate the results for any set of parameters. However, one more parameter which is of practical significance is the normalized charge discussed in Section IV. D. An additional degree of freedom on the value of the normalized charge makes it convenient to extrapolate the results in a somewhat flexible manner. As mentioned in Section V. B, a variation in the value of q^*, the normalized charge per unit length, may also be associated with a variation in the value of the

unit time interval (see Eq. 4-11). Since the value of q^* used in the mass comparison study was already high, it was considered appropriate to reduce it and then study the electron-ion mixing for the lower mass ratio. All the conditions were maintained identical as those for Run 3B (see Table 5-1), except that ℓ/L was decreased to 1, which reduced the value of Δt by a factor of 2.25 and the value of q^* by 81/16. This run is referred to as Run 3A. Typical ion trajectories (y vs. x) are shown in Fig. 5-20. The ion-beam spread is reduced as a result of the decrease in q^*; and the value of ℓ_1/ℓ_2, according to the criterion given in Fig. 5-4, is equal to 3. In this case the comparison in ion beam spread is for different values of q^*, but not for different values of ion mass as used in connection with Fig. 5-4. This indicates that the space-charge neutralization seems to be more pronounced for large values of q^*; this is true because, without any space-charge neutralization, the ion-beam spread is proportional to $(q^*)^2$ for the same value of M. The value of ℓ_1/ℓ_2 should then be about 25. Since the value of q^* for an electron is also changed perhaps a good comparison might be based on the difference between the numbers of the two types of particles in the vicinity of the decel grid; this is somewhat difficult to investigate. Sufficient data is not available to make any final conclusions along these lines.

$$\frac{M}{m} = 64, \quad \frac{\ell}{L} = 1 \qquad N_i = 3, \quad N = 90, \quad \frac{a}{\ell} = 0.75,$$

$$\frac{\varphi_1}{\varphi_o} = 0.4, \quad \frac{N_e}{N_i} = 4, \quad \omega_p \Delta t = 0.1255, \quad \frac{e\varphi_o}{kT} = 6.4$$

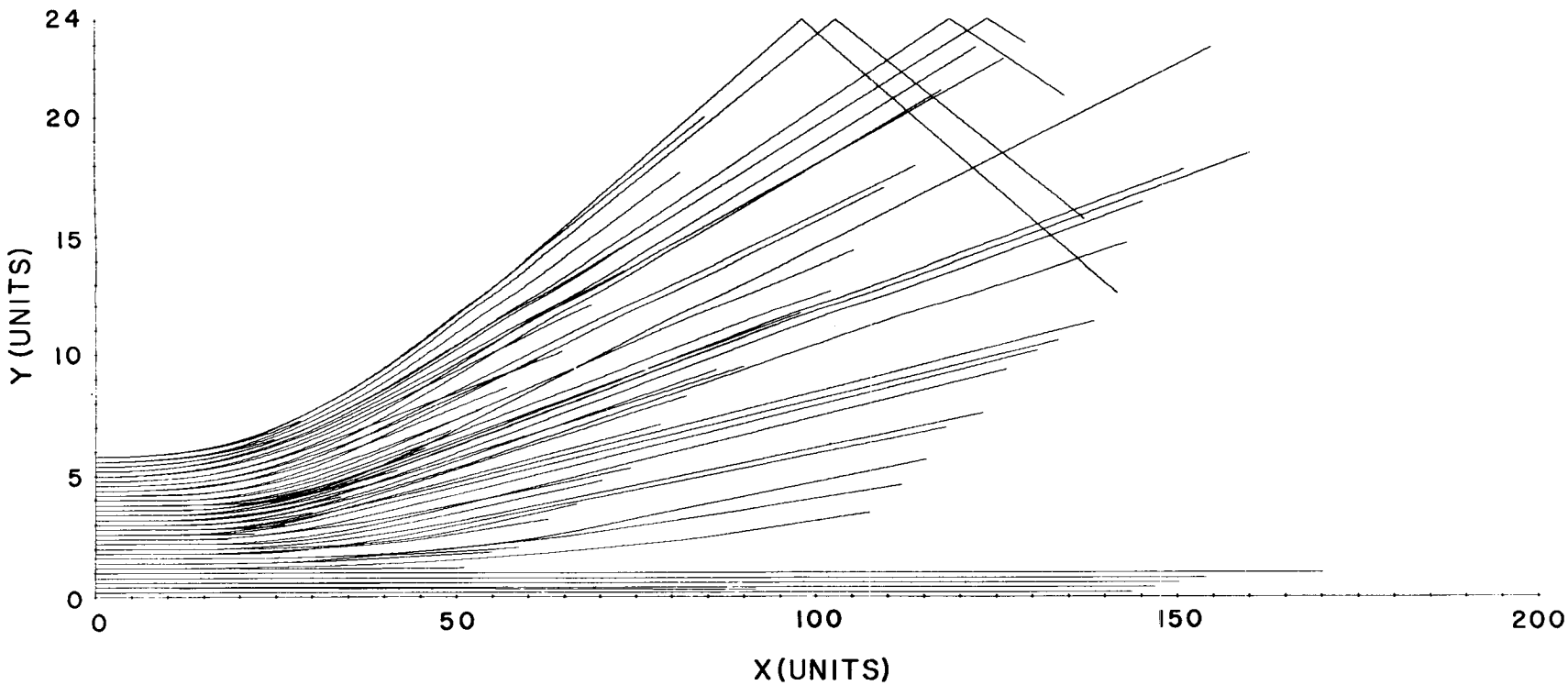

Y VERSUS X, IONS, (RUN 3A)

Fig. 5-20

Figure 5-21 shows the typical electron trajectories (x versus t) for the case of reduced value of q^*. The space-charge forces on electrons (particularly near the decel grid) are reduced, and no electron moves back to the accel grid. Otherwise, the general patterns of the trajectories seem to be similar in the two cases. Again as mentioned in Section V. C, the whole decel grid becomes a virtual emitter, and the electron cloud follows the ion cloud. For the case of reduced q^* the fluctuations in thrust and ship potential are smoothed out and the ship potential is also closer to zero.

G. Extrapolation of Results to Practical Cases

For studying the variation of electron-ion mixing with mass ratio, the value of the parameter $e\varphi_o/kT$ was selected so that

$$\frac{e\varphi_o}{kT} = 0.1 \frac{M}{m} \quad . \tag{5-5}$$

Substituting 2300°K for T, the value of φ_o for cesium ion is approximately 4.6 kilovolts, and the corresponding current density J, using Child's law, is approximately equal to 13.5 ma/cm^2 for L = 1/3 cm. For the case of different ions the values of φ_o and J would be changed accordingly. For example, $\varphi_o \simeq 35$ volts for hydrogen. If the same values of $\omega_p \Delta t$ as used for M/m = 64, 144 and 256 is used for cesuim, the value of

$\frac{M}{m} = 64, \quad \frac{\ell}{L} = 1, \quad N_i = 3, \quad N = 90, \quad \frac{a}{\ell} = 0.75,$

$\frac{\varphi_1}{\varphi_o} = 0.4, \quad \frac{N_e}{N_i} = 4, \quad \omega_p \Delta t = 0.1255, \quad \frac{e\varphi_o}{kT} = 6.4$

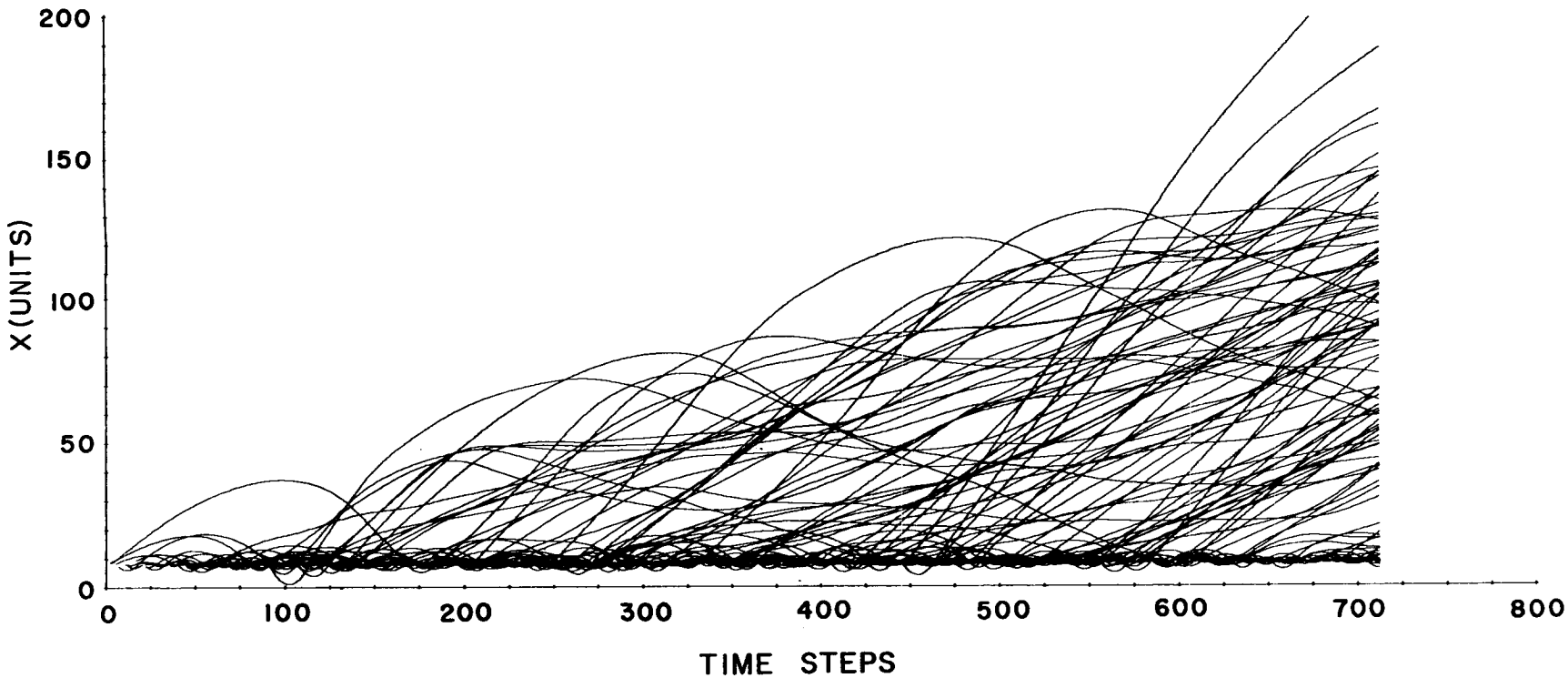

X VERSUS TIME, ELECTRONS, (RUN 3A)

Fig. 5-21

ℓ/L is given by

$$(\ell/L)_{Cs} = 3.75 \times 10^{-2} \quad . \qquad (5\text{-}6)$$

Thus for L = 1/3 cm, ℓ is approximately 5 mils. The corresponding voltage between the two grids (using $\varphi_1/\varphi_o = 0.4$) is equal to 1.84 kilovolts for cesium; with 400 volts/mil as breakdown voltage limit, there does not seem to be any problem. The corresponding value of the electron plasma frequency is approximately 1 Gc.

For the results given in this section, the distance between the two grids was kept constant (ℓ=8 mesh units), thus, it is appropriate to extrapolate the results to hydrogen and cesium ions for appropriate values of L. For example, using the relations described in Section IV, and keeping f_p = 1 Gc in all cases, the values of L is approximately 11 mils and 125 mils for hydrogen and cesium ions, respectively. The corresponding value for ℓ is then about 5 mils. It turns out that one can extrapolate the results given in this section to ions of any mass ratio by keeping ℓ constant. The corresponding current density in each case is about 13.5 ma/cm^2 when the value of L is changed appropriately; however in some cases, a change in the value of L may also be desirable to increase the current density that can be obtained.

The corresponding angles of dispersion for the cases of hydrogen and cesium ions as extrapolated from the studies of

M/m = 64, 144 and 256 for the case of the closed grids (no aperture consideration) appears to be very small. The comparison of thrust and ship potential variations for the three different cases seems to indicate that the simulation of the actual case (cesium ion) would show extremely small fluctuations in thrust and ship potential. The ship potential extrapolated for the case of cesium ions being closer to zero seems to indicate a higher degree of space-charge neutralization.

H. Correlation Between One-Dimensional and Two-Dimensional Results

Because of the two-dimensional nature of the problem, it has not been possible to track the charged particles beyond the decel grid to distances as great as in the one-dimensional simulation. The reduction in the number of binary bits for storing x- and y-coordinates by using packing technique has limited the study of electron-ion mixing mechanism to small values of ion mass ratio. Nevertheless, a study based upon variation of mass has led to an extrapolation of the space-charge neutralization mechanism for large values of mass ratio. Within these limits it has been possible to correlate the results of the one- and two-dimensional formulations. In general (this is also based upon the comparison of the results of the two cases where M/m = 144), it is found that, for the same transient duration, the fluctuations in the ship potential and thrust are reduced for the case of the two-dimensional analysis. The first emitted ions are accelerated, and electrons

with fast velocities swing back and forth in both cases. It is not necessary to generate as many electrons as required in the one-dimensional case; in fact, in one run, one-fourth of the electron emission used in the one-dimensional case was found to give adequate space-charge neutralization. It may be mentioned here that the results from the two-dimensional analysis discussed in this section and the initial results obtained for the case of an aperture seem to indicate that even a lower electron emission may be sufficient for the purpose of space-charge neutralization.

It has also been possible to correlate some of the results described in Section V with the theory of the shelf development derived for the one-dimensional case in Section III. It has been mentioned earlier that even though electrons are emitted from a narrow strip, the whole decel grid becomes a virtual electron emitter. The electrons travel a finite distance towards the accel grid and are reflected back due to the dc voltage across the two grids. However, it appears, as noticed from the potential profile shown in Fig. 3-25, that there is a zero voltage gradient region formed in the neighborhood of the decel grid plane. The electrons moving out of this region towards the accel grid experience a strong accelerating force which moves these electrons away from the accel grid. The dark region shown

in the electron (y vs. x) trajectory plots give an indication of the shelf development as described in Section III. The comparison of the theoretical results and the experimental results (obtained from the trajectory plots) is given in Table 5-4.

Table 5-4

Comparison of Shelf Results		
Run No.	L' (Theoretical)	L' (Experimental)
2E	6.45	6
3B	4.3	5

L' is the distance of the shelf from the accel grid in terms of mesh units. (See Fig. 3-25.) Since $L'/L = 1.21$ (Eq. 3-31) for the shelf formation, it is necessary that $\ell/L \geq 1.21$; this is why this comparison has been made only for two values of mass ratio. The comparison between the theoretical and experimental results is reasonably good on a first order basis. It may be mentioned here again that the theoretical results are based upon the one-dimensional formulation, while the experimental results referred to are from the two-dimensional formulation. This seems to be logical, because the potential

distribution in the vicinity of the grids is very close to that of a one-dimensional case. This makes it desirable to study the effects of the apertures in order to explore the advantages of the two-dimensional formulation.

VI. TWO-DIMENSIONAL ELECTRON-ION MIXING WITH AN APERTURE AT THE DECEL GRID PLANE

A. Introduction

The formulation of the two-dimensional electron-ion mixing problem with transparent accel and decel grids is described in Section IV, and the results are given in Section V. In this case it is assumed that there are no transverse variations of potential along the two grids, and that the grids are transparent in order not to affect the motion of the charged particles. Actually, these assumptions are not valid, because the effect of the aperture can be considerable, particularly when the size of the aperture is comparable to the distance between the two grids. The main problem in the case of an open grid is the solution of Poisson's equation with appropriate simulation of the boundary conditions. There are also some minor modifications in the formulas used for field evaluation.

In general, solution of Poisson's equation with arbitrary boundary conditions is quite time-consuming; most of the present-day methods involve several iterations until a reasonable convergence is obtained. In our problem, the simulation of arbitrary boundary conditions has been achieved by modifying the Fourier analysis and marching method used in solving for the potential distribution.

The modification consists of solving for potential distribution without any boundary constraints, then adding appropriate compensation charges at the required locations (specified by boundary constraints), and solving again for the potential distribution. The total computer time needed to obtain the correct potential distribution with boundary constraints is far less than twice that needed for the case with no such boundary constraints. The computer times are approximately the same when these boundary constraints are close to the accel grid. For boundary constraints near the plane x=200, where space conditions are simulated, the total computer time for obtaining the correct potential distribution is increased (to two times that with no boundary constraints); in that case it may be necessary to adopt a different technique and/or modify our present approach for solving Poisson's equation. This is discussed in detail in the next sections.

B. Evaluation of Capacitance Matrix

It was mentioned in the last section that, in order to obtain a correct potential distribution, it is necessary to add appropriate values of compensating charges at locations specified by boundary constraints. This procedure simulates the effects of the boundary constraints. Thus, the correct potential distribution is obtained as a result of superposition of the actual charge (electrons and ions)

distribution and the compensating charges mentioned above. The values of the compensating charges are obtained by multiplying the capacitance matrix (discussed below) and the uncorrected potential matrix. The uncorrected potential matrix is given by potentials at the locations of the boundary constraints when these potentials are evaluated without any consideration of the boundary constraints.

For the present case it is assumed that the accel grid is still transparent, i.e., there are no transverse variations of potential along the decel grid. The ions are injected with zero transverse velocity, although the effect of the aperture can be simulated by considering appropriate velocity distribution for the x- and y-components, the ions being injected at various points along the aperture. Only the electron emitter (which constitutes a small part of the decel grid plane) is held at a constant potential, while the potentials at other points along the decel grid plane can vary according to the actual space-charge distribution. The configuration of the electron emitter is shown in Fig. 6.1. In order to take into account the effect of the boundary constraints at the electron emitter, it becomes necessary to compute the potential as a result of an arbitrary charge located at any one or a combination of these points. This potential

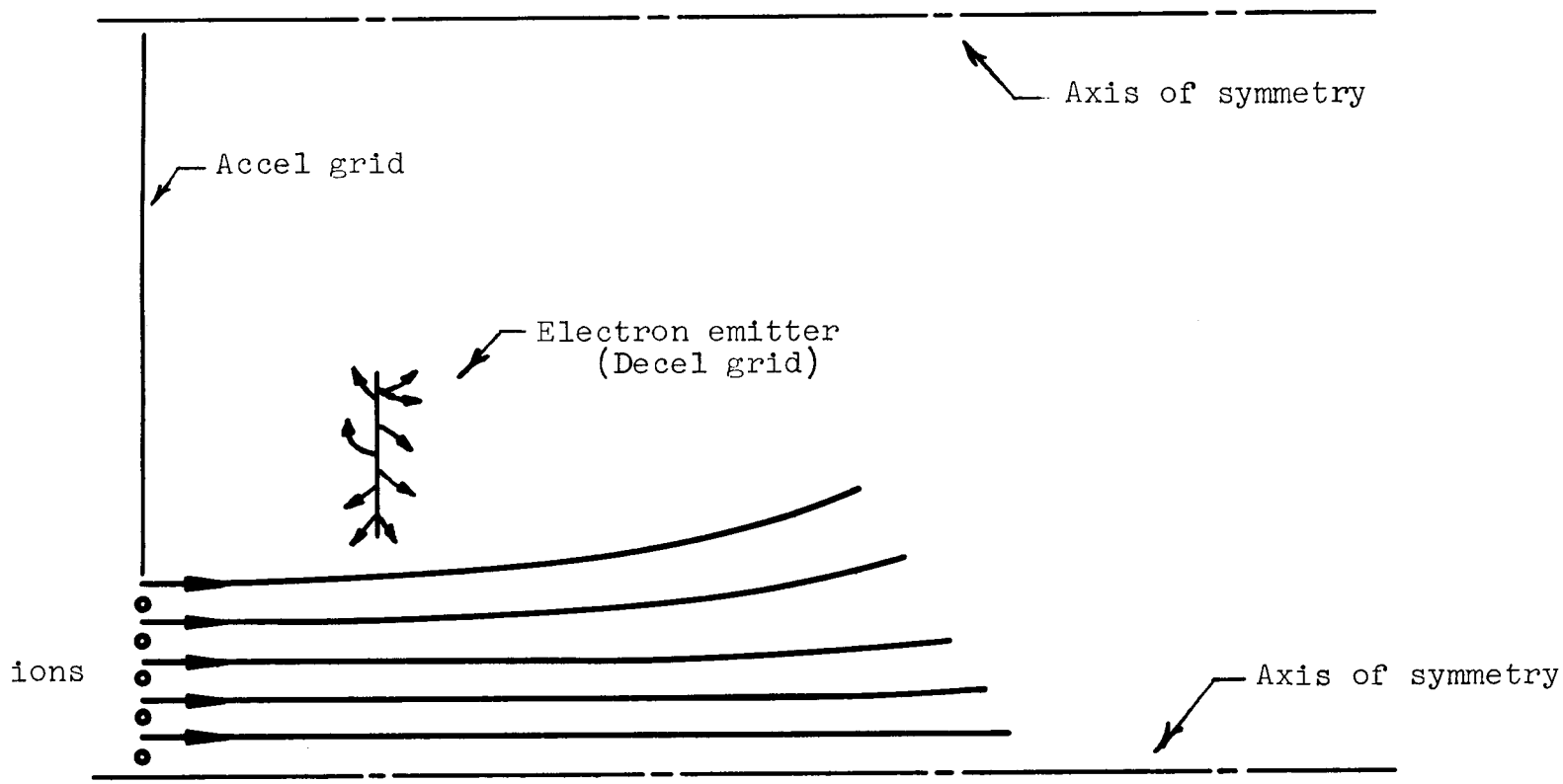

A SCHEMATIC OF ACCEL-DECEL SYSTEM

Fig. 6-1

is evaluated at the locations of boundary constraints and with zero voltage at the accel grid. The relationship between the voltages and charges at these points gives the inverse capacitance matrix, which is a function of the geometrical configuration only. The inverse of the inverse capacitance matrix (capacitance matrix) is given by:

$$\begin{pmatrix} q_1 \\ q_2 \\ q_3 \\ \cdot \\ \cdot \\ \cdot \\ q_n \end{pmatrix} = \begin{pmatrix} C_{11} & C_{12} & C_{13} & - - - - - & C_{1n} \\ C_{21} & C_{22} & C_{23} & - - - - - & C_{2n} \\ C_{31} & - - - - - - - - - - - & & & \\ \cdot & & & & \\ \cdot & & & & \\ \cdot & & & & \\ C_{n1} & C_{n2} & C_{n3} & - - - - - & C_{nn} \end{pmatrix} \begin{pmatrix} V_1 \\ V_2 \\ V_3 \\ \\ \\ V_n \end{pmatrix} . \qquad (6\text{-}1)$$

The diagonal and off diagonal terms of this matrix are referred to as the self- and cross-capacitances of the various mesh points in consideration. As mentioned above, the capacitance matrix is obtained by inverting an n by n matrix. The maximum value of n is restricted by the amount of computer time required to invert the matrix. In general, the diagonal terms are dominant, and in case of large values of n, approximations may be made to take into account only a few terms. This will reduce the computer time in inverting a matrix. In the present case,

n=5; the matrix is inverted only once, and the matrix coefficients are stored on tape. Thus, the computer time involved in inverting a matrix is not of great concern, and the potential distribution obtained is quite accurate.

C. Solution of Poisson's Difference Equation with Boundary Constraints

The procedure for solving Poisson's difference equation with boundary constraints (aperture at the decel grid plane) consists of the Fourier analysis and marching method; Gauss's reduction method is not used. However, there is an additional marching back and forth from the decel grid plane to the accel grid, as discussed below. The algorithm for obtaining the correct potential distribution from the charge distribution is shown in Fig. 6.2, and a schematic of marching process at an arbitrary time is shown in Fig. 6.3. For the case of the transparent grid, March 2 and March 3 are not included, while the end of March 1 and the beginning of March 4 occur at the decel grid and not at the accel grid. With the actual charge distribution, the potential distribution (without any boundary constraint) is obtained at the decel grid plane after the March 2 process (the accel grid being held at a constant potential with respect to the electron emitter as before). The values of the compensating charges are obtained by multiplying the capacitance matrix with the potential matrix (potentials at the locations of the

ALGORITHM

1. Calculate charge harmonics.
2. Starting from I_{max}, march to accel grid calculating ψ's.
3. March to decel grid calculating potential harmonics.
4. Calculate potentials along the decel grid.
5. Calculate compensating charges and add to the existing charges at locations of boundary constraints.
6. Calculate charge harmonics along decel grid.
7. Starting from decel grid, march to accel grid modifying the previous values of ψ's.
8. Starting from accel grid, march to I_{max}.
9. Calculate correct potential distribution.

AN ALGORITHM FOR OBTAINING POTENTIAL DISTRIBUTION FROM THE CHARGE DISTRIBUTION

Fig. 6-2

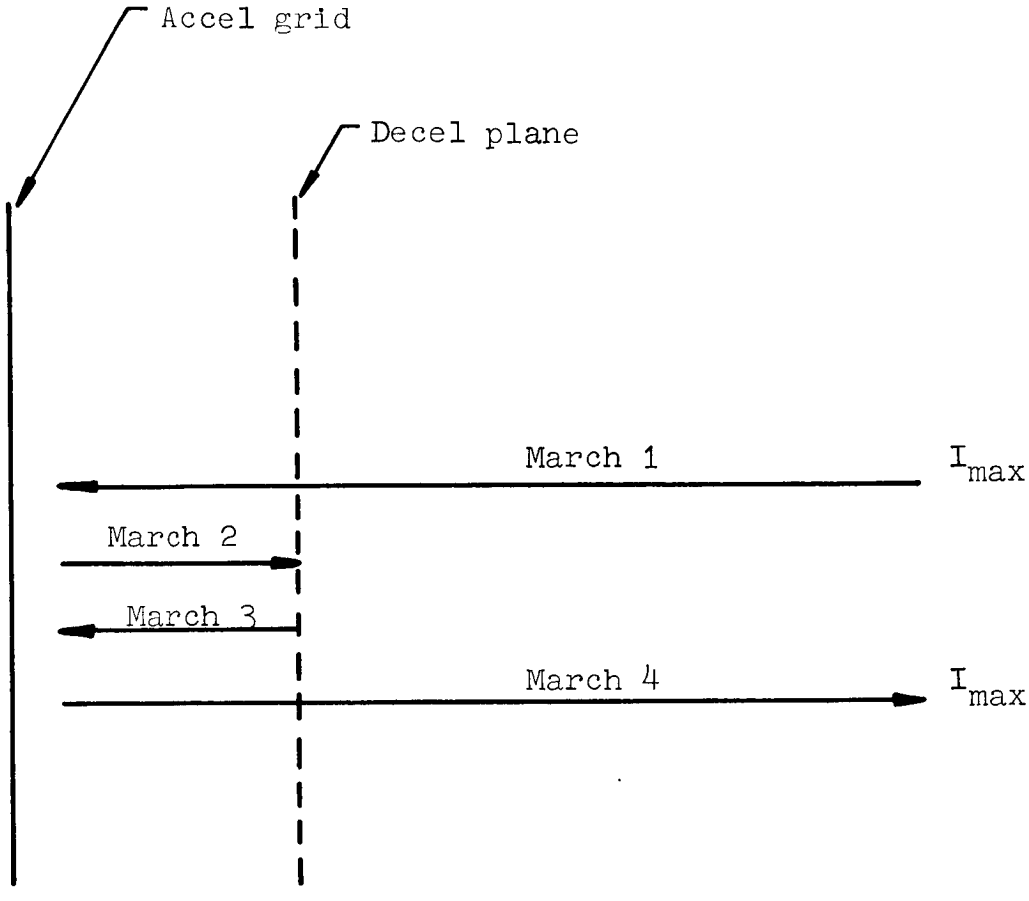

A SCHEMATIC OF MARCHING PROCESS

Fig. 6-3

electron emitter), and added at the appropriate locations. Starting with the previous values of ψ's at column next to the decel grid column, new values of ψ's are obtained by taking into account the actual charge distribution and the compensating charges. The marching process is then completed to obtain the correct potential distribution. The updating of the charged particles is carried on as in the previous case.

D. Thrust Evaluation

The expression for the normalized thrust given by Eq. 4-81 takes into account contributions from both the accel and decel grids. For the case of an open grid there is a conducting plane (emitter) over a relatively short length along the decel grid plane, which makes it necessary to modify the expression for the normalized thrust. Proceeding in a manner similar to that in the closed-grid case, and modifying the contributions from the decel grid plane, the expression for the normalized thrust is given by

$$\frac{T}{T^*} = \frac{2\Delta v}{b}\left\{\sum_{j=1}^{25} 1 - \frac{\left(\frac{\Delta x}{\ell}\,\frac{2\ell}{3L}\right)^2}{(\omega_p \Delta t)^4}\left[\left(\frac{\partial V_j}{\partial x/\Delta x}\right)_3\right]^2\right\}$$

$$- \frac{1}{n}\left\{\sum_{j=1}^{n}\left[\left(\frac{\partial V_j}{\partial x/\Delta x}\right)_1\right]^2 - \left[\left(\frac{\partial V_j}{\partial x/\Delta x}\right)_2\right]^2\right\}\frac{\left(\frac{\Delta x}{\ell}\,\frac{2\ell}{3L}\right)^2}{(\omega_p \Delta t)^4}\,, \quad (6\text{-}2)$$

where suffixes 1, 2, and 3 refer to electric fields E_1, E_2, and E_3 as shown in Fig. 4-4, and n is equal to the length of the electron emitter in terms of Δx's (the results given in next section are for n=5). The contributions from the 1st and 25th rectangles are to be divided by 2, since only half end rectangles are considered.

E. Results

A test run, namely 5A, was formulated for the program with an aperture at the decel grid plane, and the parameters selected for this case are the same as those for the run 2E, discussed in Section V.C., except that $N_e/N_i=3$ is selected in this case. The absorption area of the decel plane, in this case, is reduced, and thus the electron emission required for adequate neutralization is also reduced. The variation of the normalized thrust (Eq. 6-2) and ship potential (discussed in Section IV. E.4) as a function of time are shown in Figs. 6-4 and 6-5, respectively. The ship potential plot is compared with the case of closed grid and is found to be more steady and close to zero for the case of aperture. The fluctuations in thrust and ship potential do not seem to be detrimental to the ion engine performance. The thrust reaches its asymptotic value (less than unity) earlier than that for the case of the closed grid; this is

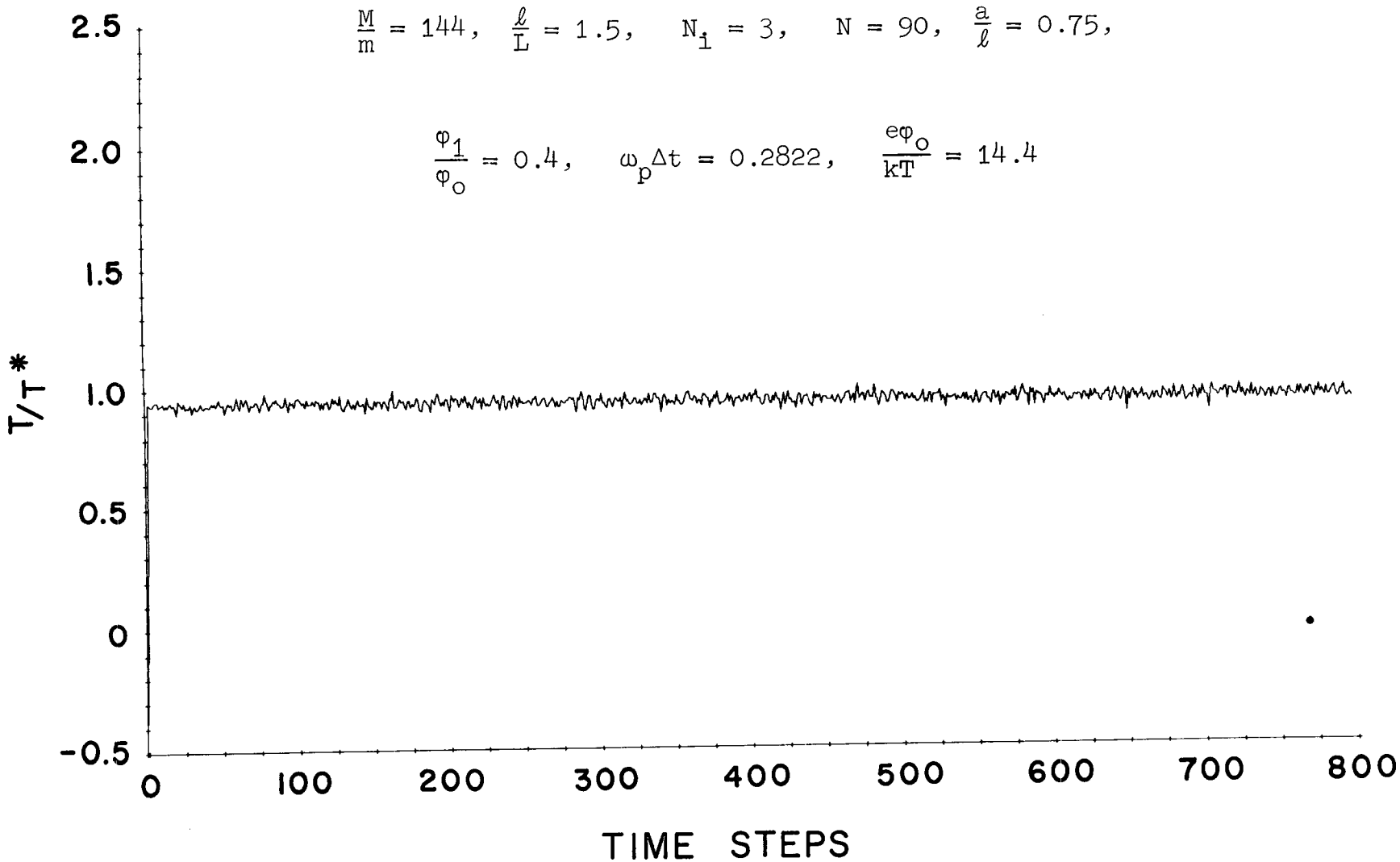

THRUST VERSUS TIME, (RUNS 2E AND 5A)

Fig. 6-4

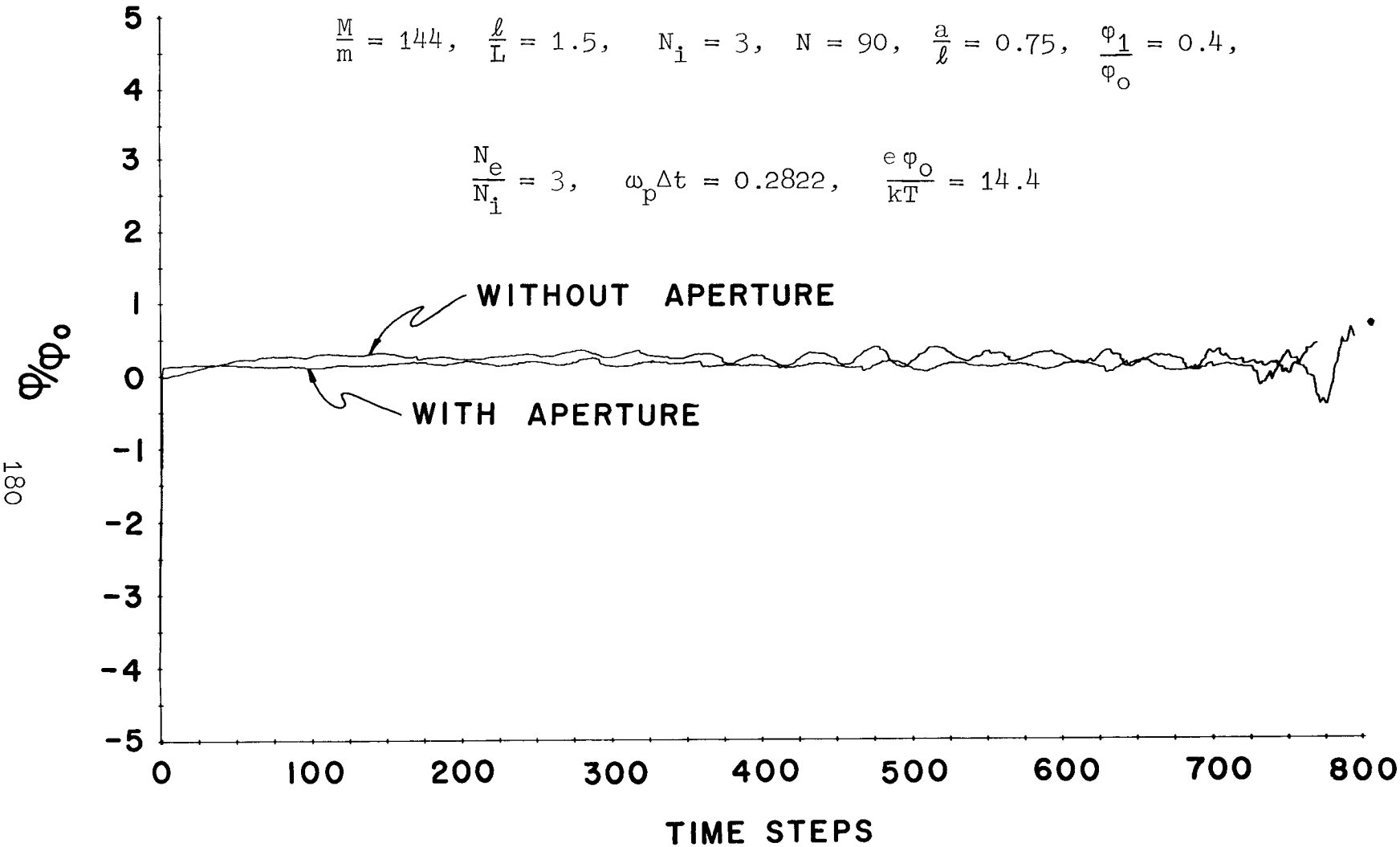

SHIP POTENTIAL VERSUS TIME, (RUN 5A)

Fig. 6-5

attributed to the fact that the average value of E_2 (see Fig. 4-4) is closer to zero than that for the case of the closed grid. As explained earlier, this reduces the value of the thrust. There is no appreciable difference in thrust in the two cases.

The equipotential plots for this case at time intervals $T/\Delta t=200$ and 600 are shown in Figs. 6-6 and 6-7, respectively. Adequate space-charge neutralization seems to occur in the vicinity of the electron emitter. Even though there may be more electrons in the neighborhood of the electron emitter, the presence of ions seems to affect the potential in its vicinity. The resolution in computing the voltage distribution is of the order of one mesh unit. Consequently, it is difficult to estimate the exact potential distribution in the region near the electron emitter. It may be noticed that all the electrons will be reflected towards the ion beam because the electrons moving away from the ion beam encounter relatively high potential barriers. This is compared with the equipotential plots for the case of the closed grid at the same time intervals ($T/\Delta t=200$ and 600) in Figs. 6-8 and 6-9. The accel grid is at -1.024V (normalized potential) with respect to the decel system in all the cases; the number 1.024 results because of the values of the parameters used in Eq. 4-9. It is quite clear from these plots why the complete decel grid (for the idealized case) becomes

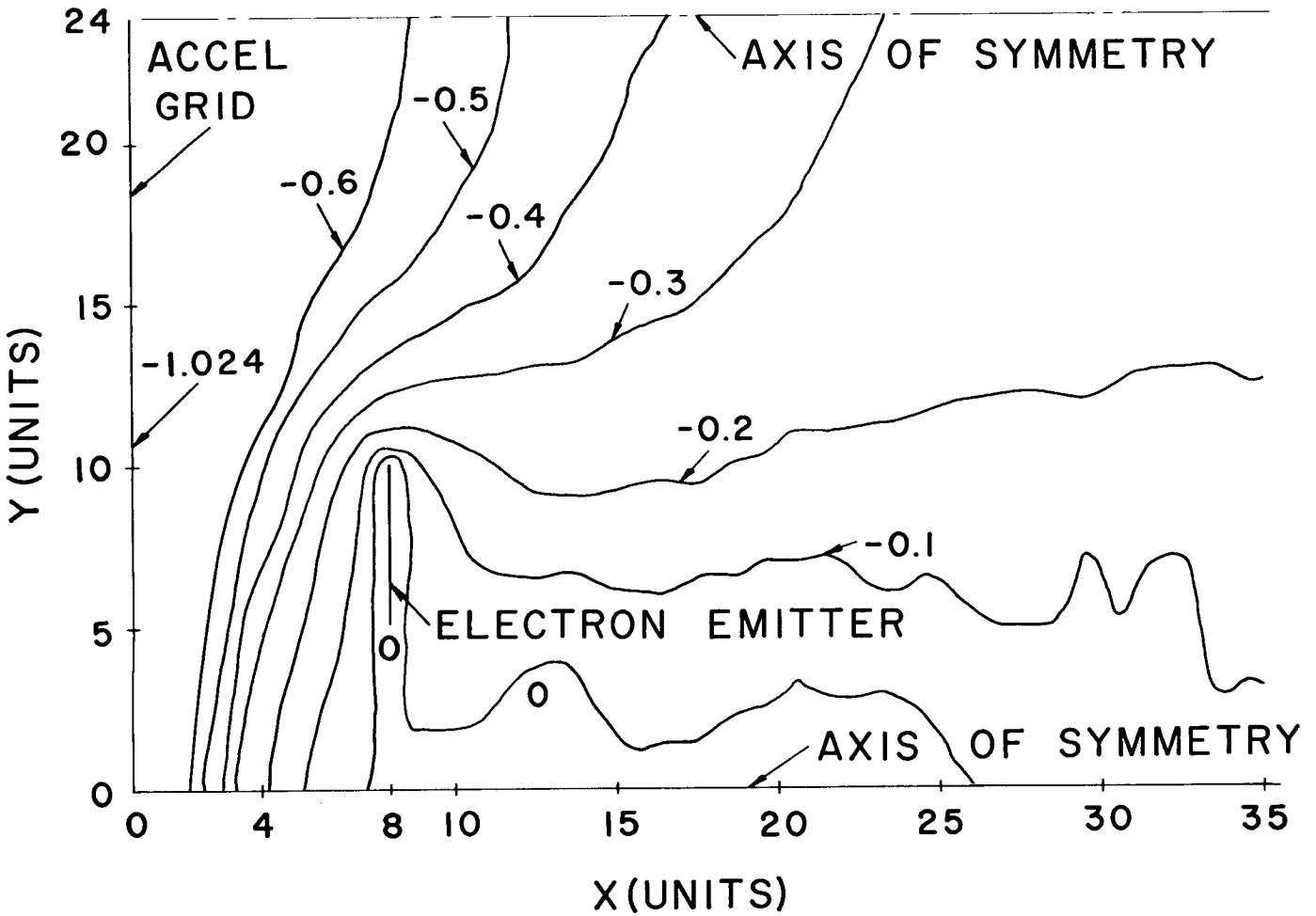

NORMALIZED EQUIPOTENTIALS IN NORMALIZED SPACE; (RUN 5A), TIME STEP: 200

Fig. 6-6

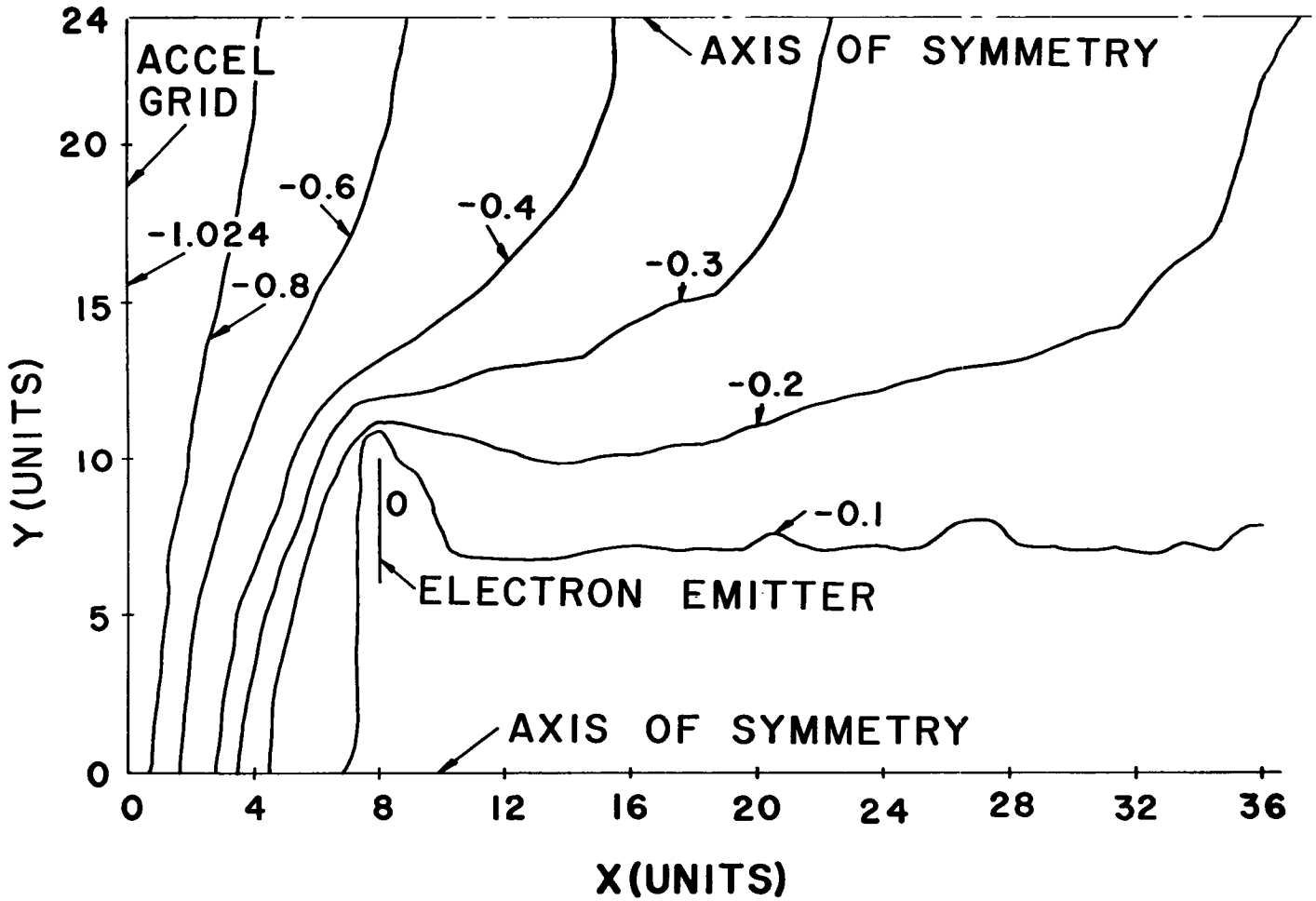

NORMALIZED EQUIPOTENTIALS IN NORMALIZED SPACE; (RUN 5A), TIME STEP: 600

Fig. 6-7

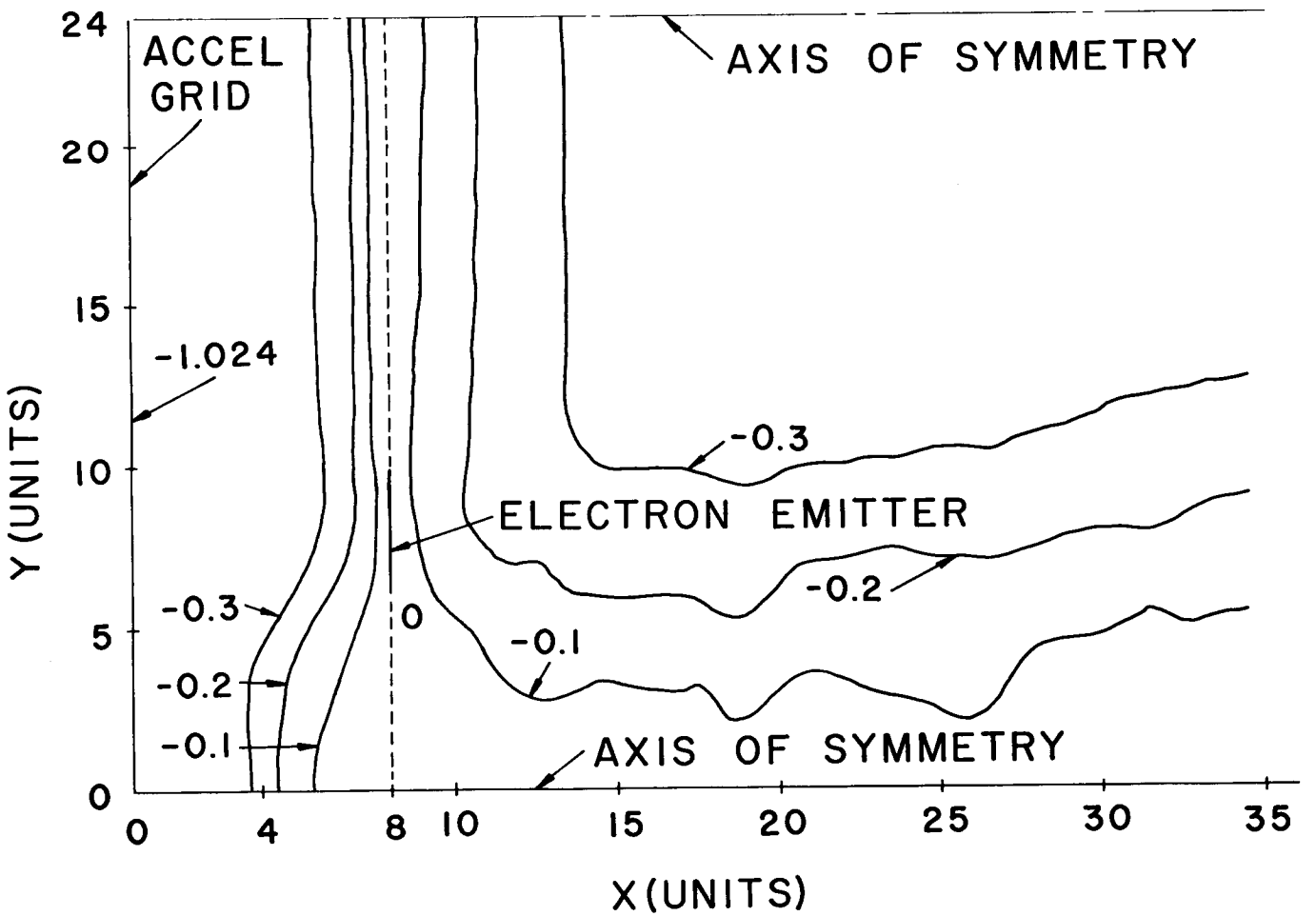

NORMALIZED EQUIPOTENTIALS IN NORMALIZED SPACE; (RUN 2E), TIME STEP: 200

Fig. 6-8

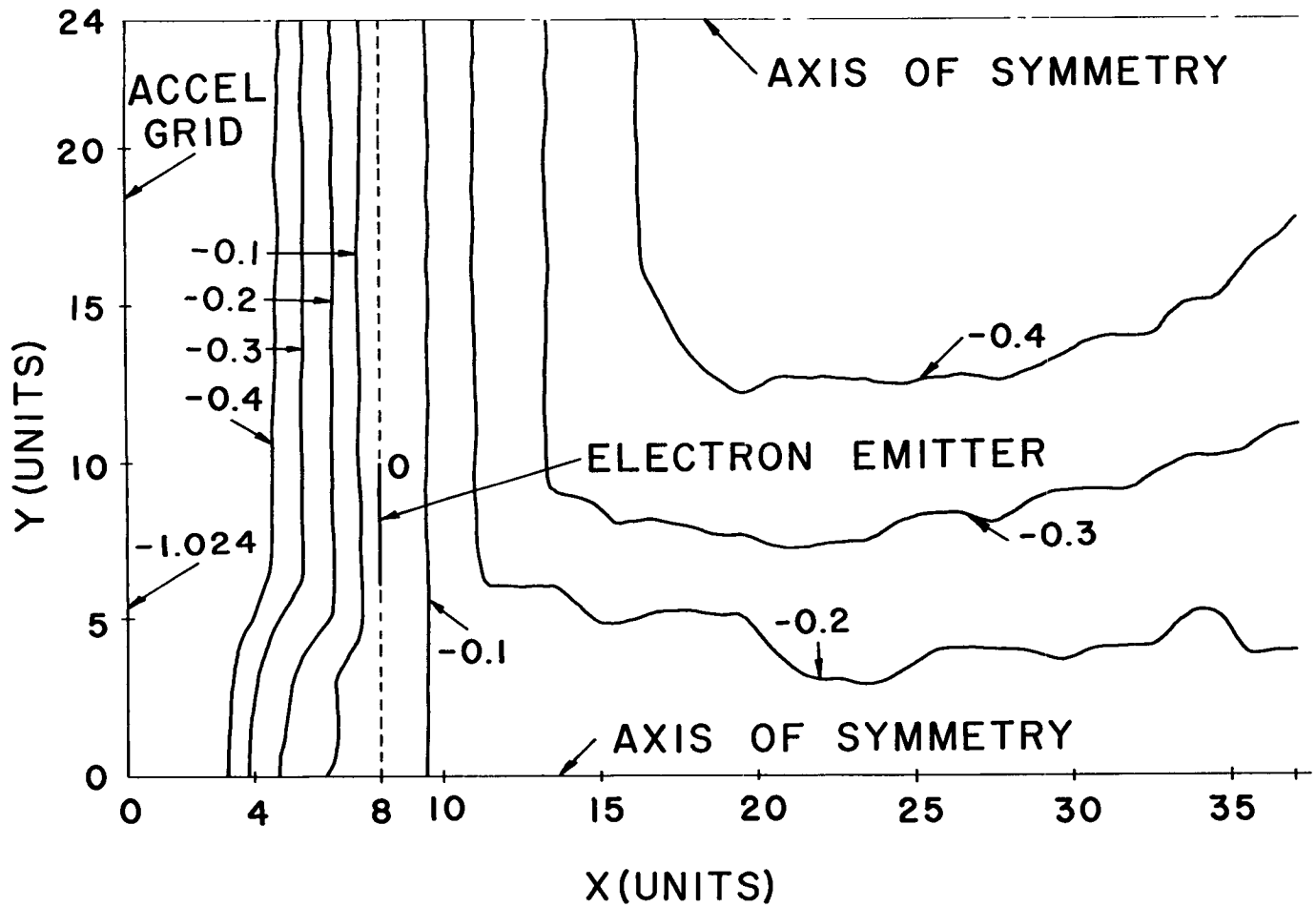

NORMALIZED EQUIPOTENTIALS IN NORMALIZED SPACE; (RUN 2E), TIME STEP: 600

Fig. 6-9

eventually a virtual emitter, even though electrons are emitted from a narrow strip. Figure 6-9 indicates there are more electrons in space, and the region near the decel grid is adequately neutralized; thus, only fast energy electrons will be able to go into space (as compared to those in the case of a closed grid). The effect of the aperture on the potential distribution is quite clear from the plots shown in Fig. 6-10, which represents the condition after the tenth time interval, when the number of particles is relatively small. In general, the potential distribution varies from one time step to another time step.

Figure 6-11 shows the typical trajectories of electrons in the x-y domain. The remarkable difference between the electron trajectories for the two cases - namely, without aperture and with aperture - may easily be noticed by comparing Figs. 5-6, 5-7 and 6-11. Because of the different potential distribution shown in Figs. 6-6 and 6-7 (when compared with that given in Figs. 6-8 and 6-9), for the case of an open grid only high energy electrons would be able to move upward; hence, most of the electrons are directed toward the ion beam. This indicates that the effect of the aperture is helpful in space-charge neutralization. Typical ion trajectories (x-y domain) are shown in Fig. 6-12. A comparison of trajectory plots

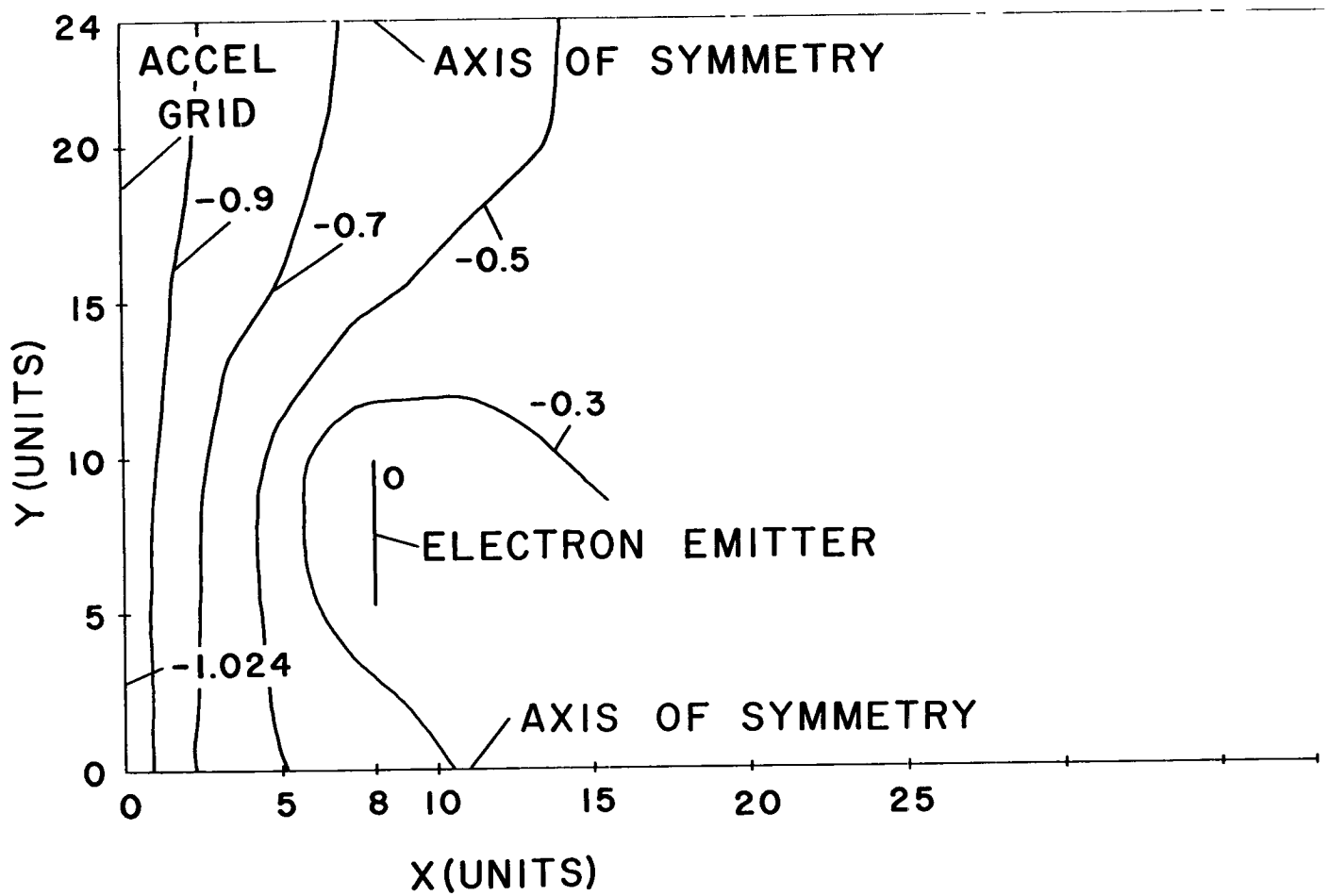

NORMALIZED EQUIPOTENTIALS IN NORMALIZED SPACE; (RUN 5A), TIME STEP: 10

Fig. 6-10

$$\frac{M}{m} = 144, \quad \frac{\ell}{L} = 1.5, \quad N_i = 3, \quad N = 90, \quad \frac{a}{\ell} = 0.75, \quad \frac{\varphi_1}{\varphi_o} = 0.4,$$

$$\frac{N_e}{N_i} = 3, \quad \omega_p \Delta t = 0.2822, \quad \frac{e\varphi_o}{kT} = 14.4$$

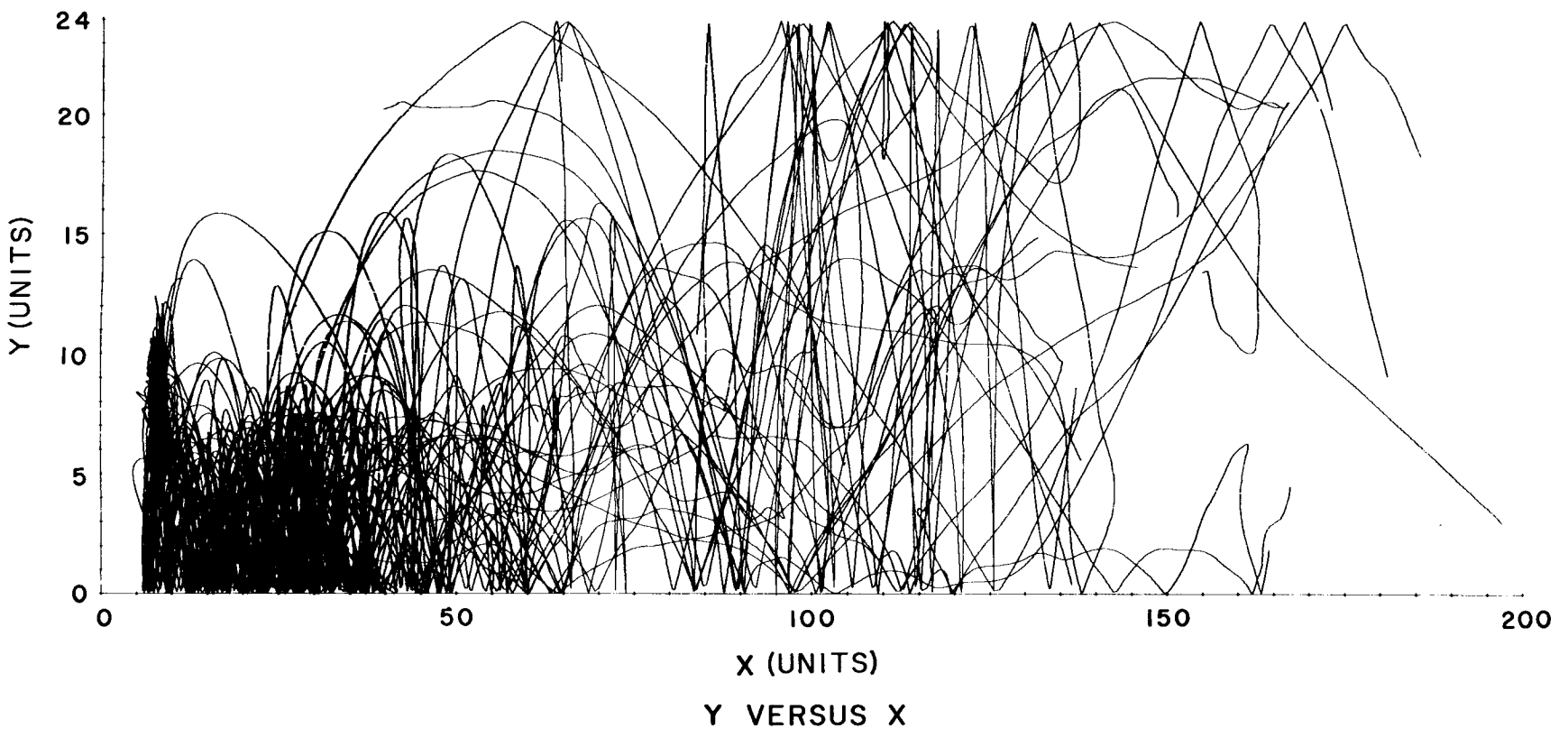

Y VERSUS X, ELECTRONS, (RUN 5A)

Fig. 6-11

$$\frac{M}{m} = 144, \quad \frac{\ell}{L} = 1.5, \quad N_i = 3, \quad N = 90, \quad \frac{a}{\ell} = 0.75, \quad \frac{\varphi_1}{\varphi_o} = 0.4,$$

$$\frac{N_e}{N_i} = 3, \quad \omega_p \Delta t = 0.2822, \quad \frac{e\varphi_o}{kT} = 14.4$$

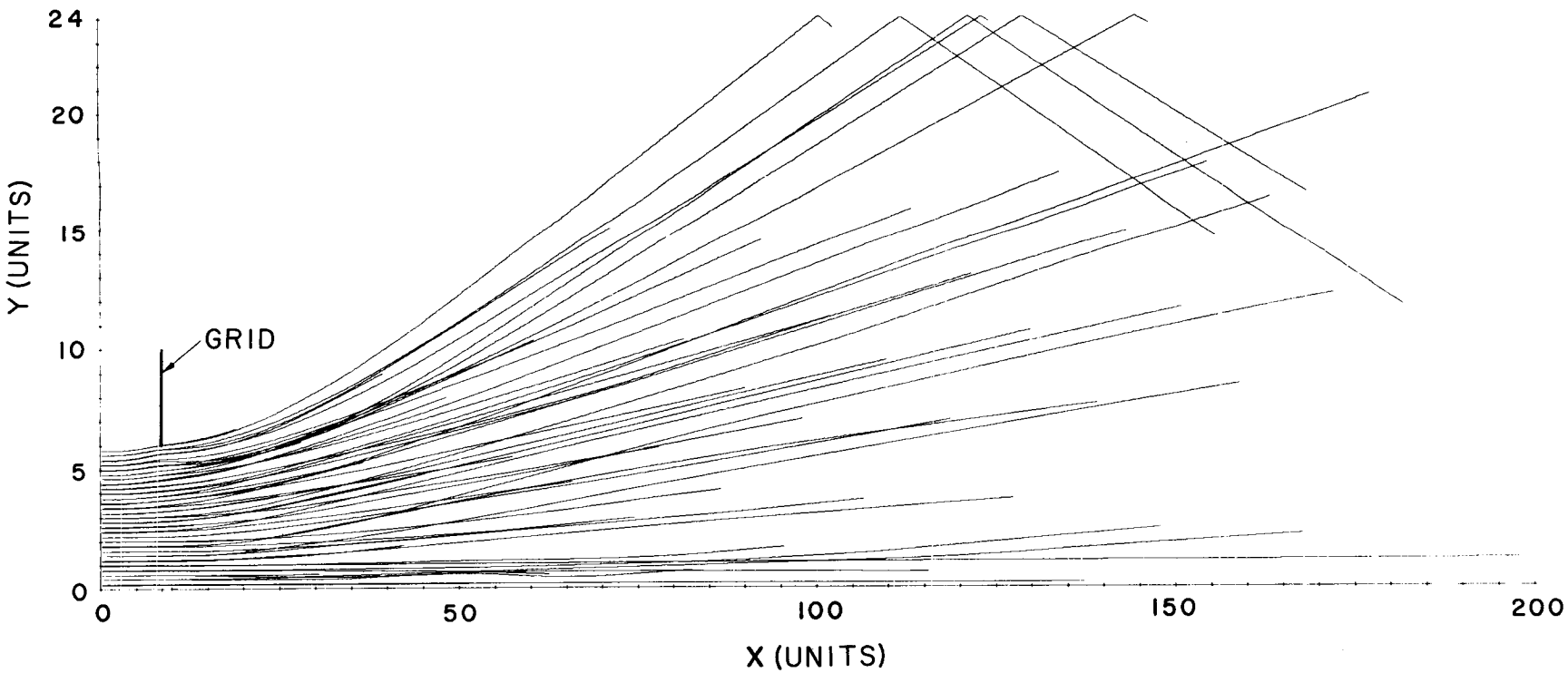

Y VERSUS X, IONS, (RUN 5A)

Fig. 6-12

given in Figs. 5-2 and 6-12 indicates that, because of increased space-charge neutralization for the case of an open grid, the ion-beam spread has been reduced. As mentioned in Section V, the electrons follow ions very closely and move into the ion beam with fluctuating space-charge fields.

VII. CONCLUSIONS AND SUGGESTIONS FOR FURTHER WORK

A. Conclusions

This report has described the formulations and results of the analysis of the electron-ion mixing mechanism for the one- and two-dimensional models, as applied to ion-beam engines. A study based upon several combinations of the various parameters, such as ion-electron mass ratio, electron emission, ion emission, etc., has thrown a considerable light on the space-charge neutralization mechanism desired for ion-beam engines.

For the one-dimensional case, electrons and ions are used as sheet charges; genuine space conditions are imposed on the advancing head of the beam. The space-charge fields are evaluated by using Green's function. Time sequences of plots for ship potential are described. In general, it is found that there are more electrons needed for space-charge neutralization purposes as compared to those needed in the two-dimensional case, and a deficiency in electron emission leads to instability. A sufficient number of particles has been considered, and these particles were allowed to move under the existing space-charge forces to distances limited by the computer memory; in some cases distances as high as 100 intergrid spacings were considered. The fluctuations in thrust and ship potential in some cases build up. Primarily, this was traced due to

lack of electrons. It may be mentioned here that the corresponding fluctuations in the one-dimensional case are greater than those for the two-dimensional case, even for the same transient durations; this may be due to the inferiority of the one-dimensional formulation as compared to the two-dimensional formulation. Needless to say, the two-dimensional model analyzed in detail is not as close to the practical configuration because of the closed grid (no aperture) assumption.

In the two-dimensional formulation, a periodicity in the transverse direction is assumed. A symmetry across the center line of each plane makes it convenient to study the electron-ion mixing with fairly good resolution. The space configuration is divided into 200 x 24 rectangles. (This is limited by computer storage.) An assumption that the beam beyond 200th rectangle is completely neutralized makes it convenient to simulate the space conditions appropriately and to study the transient behavior for a long time. The potential distribution as a result of the charge distribution and the dc voltage across the accel and decel grids has been solved by using the Fourier analysis and marching method; this technique seems to be extremely fast for solving Poisson's equation as compared to other existing methods.

Even though electrons are emitted from a narrow strip, the whole decel grid for the closed grid case becomes a virtual emitter, which has been explained by the potential distribution in the neighborhood of the decel grid. It is found that the fast electrons experience more fluctuations in the transverse direction. The electrons mix into the ion beam with fluctuating fields; these fields admit electrons of the required velocity and in approximately the right number. However, it is necessary to have sufficient electrons, because a deficiency of electrons does cause turning back of ions, which leads to thrust deterioration, so that the ship becomes negatively charged. In general, the ship potential is positive, because there are usually more electrons leaving the system during the transient period, although, under equilibrium conditions, the number of electrons and ions leaving the system should be the same.

Because of the packing technique, i.e., storing the x- and y-coordinates of a particle in a single computer word location, the study of electron-ion mixing has been limited to rather smaller values of ion mass ratio. A comparison study of the electron-ion mixing mechanism has enabled us to extrapolate the results to the case of practical values of ion mass ratio. There is beam-spreading as a result of the ions' own space-charge, which is partially

neutralized by electrons. It is found that the ion beam spread is inversely proportional to the ion mass ratio. The reduction of further spreading of the ion beam seems to indicate that there is adequate space-charge neutralization in the vicinity of the decel grid.

An extrapolation of this study to the practical values of ion mass ratio seems to indicate that, for hydrogen and cesium ions, the angle of beam dispersion is very small, which will not cause any thrust deteriorations. By keeping the distance between the two grids constant (8 units in this case), it is possible to extrapolate the results to the case of arbitrary ion mass ratio while keeping some of the pertinant parameters, such as plasma frequency, Debye length, current density, etc., identical in all cases; this ability is due to the fact that the formulation is normalized.

In general, the fluctuations in the ship potential and thrust are smaller than those found in the one-dimensional case for the same transient duration. While the fluctuations in the ship potential and thrust are caused by excess number of electrons which move back and forth, reduction in thrust is caused by ion beam spread. A reduction in electron emission does smooth out these fluctuations, but thrust is slightly decreased. It is not clear as yet what the long beam simulation would indicate

about the performance of the ion engine. The electron emission needed for adequate neutralization also seems to be less for the two-dimensional case than for the one-dimensional case.

The two-dimensional formulation considered here is limited in the sense that, because of the assumption of the closed grid, the voltage distribution in the vicinity of the decel grid is approximately the same as in the case of the one-dimensional configuration. The results of the shelf development based upon one-dimensional formulation are in good agreement with the results obtained from the two-dimensional formulation.

The case of an aperture at the decel grid is simulated by modifying the marching method and using a charge compensation technique. The equipotentials for this case are considerably altered, and the electrons seem to be drawn towards the ion beam more than they are in the closed grid case. The plots for the electrons and ions trajectories have not been made during this period, because funds had been exhausted. The tape with the trajectories stored on it will be run upon the anticipated renewal of the contract. The fluctuations in the ship potential and thrust seem to be of the same order of magnitude as in the case of the closed grid.

B. Suggestion for Future Work

The results of the one-dimensional and two-dimensional formulations for analyzing the electron-ion mixing mechanism described in this report have led to a very good understanding of the space-charge neutralization needed in the ion-beam engines. The two-dimensional formulation considered here is much closer than the one-dimensional formulation, to the practical configurations, and some interesting results on ion beam-spreading have been obtained. However, because of the closed grid assumption, the potential distribution in the vicinity of the decel grid is very nearly the same as that in the one-dimensional case; in fact, the correlation of the results (electron trajectories in the x-y domain) with the theory of the shelf development based on one-dimensional formulation also seems to indicate this. This makes it rather important to study the aperture, simulating more closely the actual case. It is felt that the results would differ considerably from the results obtained so far. Thus, an optimization of both the shape and position of the electron emitter would be desirable for further investigation. Along with the simulation of the aperture at the decel grid, it is also desirable to simulate the aperture at the accel grid. This would then imply new boundary conditions at the accel grid, both in terms of the potential distribution and velocity component's distribution for the ions injected across the accel grid.

The studies to date have indicated that there is an adequate space-charge neutralization in the vicinity of the decel grid, although the bouncing off of the electrons

from the front of the beam does seem to indicate that complete thermalization has not occurred. Variations in electron emission and in initial electron velocity would, of course, lead to different results, but it would be then desirable to investigate the degree of thermalization and to determine electron and ion temperatures in order to obtain a greater understanding of the space-charge neutralization mechanism. It appears that the thermalization studies could be made both for the one- and two-dimensional cases within the limitation of computer storage. The potential profile in space would also augment the understanding of the space-charge neutralization and thermalization mechanisms.

Due to computer limitations it has not been possible to simulate long beams and to study the fast electrons moving ahead of the beam; these electrons eventually bounce back from the free space and move back into the region under consideration. A simulation based upon this reflection would enable us to extend our transient study for longer time intervals. This would enable us to explore any instability. A consideration of smaller values of mass ratio is also helpful in the early diagnosis of ion instability.

One alternate way to simulate a long beam would be to reduce the number of rectangles in the transverse

direction: for example, from 48 to 24 in a period. This would enable the tracing of the particles to a larger number of rectangles along the x-axis. This would then require an additional binary bit for specifying the integral part of the x-coordinate, which might demand reduction in the decimal accuracy for the x-coordinate. Some considerations towards a variable spacing along the x-axis would also be helpful in achieving long beam simulation.

The study of rf impedance across the two grids was initiated, but has not been completed. (A brief mention of this work is made in the 5th quarterly report.[15]) It is expected that a consideration of the rf impedance across the two grids would lead to results which are different from those obtained to date, because the voltage is induced on the circuit, and this alters the trajectories considerably. It seems that the effect of the rf impedance would be to reduce the instability mechanism. Furthermore, a case of density or velocity modulation across the two decel grids would also be helpful in instability diagnosis.

---

15. R.P. Wadhwa, "Analysis of Electron-Ion Mixing in Ion Engines", Quarterly Report No. 6, Contract No. NAS 3-2503; September 30, 1963.